Chapter 6

A_b with Momentum-Weighted Charge: Binned Asymmetry

6.1 Introduction

This chapter and the next present experimental determinations of A_b using the polarized forward-backward asymmetry* of b quarks from Z^0 decay. The sample of $Z^0 \rightarrow b\bar{b}$ events was isolated using a lifetime tag [134], and discrimination between the b and $\bar{b}$ directions of the decay axis was provided by the event momentum-weighted charge. The SLD Monte Carlo is used in this chapter to estimate the tag composition, the probability the decay axis is correctly signed, and the magnitude of radiative effects.

The remainder of this section will present a brief outline of the technique and justify its use. Following that is a detailed presentation of the measurement, its systematic errors, and cross-checks that have been investigated. Chapter 7 presents a second version of the analysis which reduces the systematic error by deriving its calibration from experimental data.

*Also called the "left-right forward-backward asymmetry."

6.1.1 Technique Overview

To extract the value of A_b using the left-right forward-backward asymmetry, the values of two observables must be measured for a sample of $Z^0 \rightarrow b\bar{b}$ events. The first is the b quark direction relative to the incident electron direction, expressed as

$$\cos\theta = \vec{p}_b \cdot \vec{p}_{e^-} / p_b p_{e^-}. \tag{6.1}$$

where $\vec{p}_b$ and $\vec{p}_{e^-}$ are the b quark and electron momenta, respectively. In general, the $\bar{b}$ quark will travel in the direction opposite to the b quark. The second is the electron beam polarization, P_e. $\tilde{A}^b_{FB}$, the asymmetry which is defined in Equation 1.70, and which is proportional to A_b and P_e, can then be computed and A_b extracted.

Lifetime Tag

The Z^0 decays into each fermion in Table 1.1 except for the t quark, so the first step in the technique is to separate a sample of $Z^0 \rightarrow b\bar{b}$ decays from the others, by taking advantage of the long lifetime and high mass of B hadrons.

Track impact parameters to the interaction point (IP) have been used previously [135] to isolate enriched samples of $e^+e^- \rightarrow b\bar{b}$. The technique is often called a "lifetime tag" because the average impact parameter of B decay tracks is nearly independent of the momentum of the parent B hadron, but rather depends linearly on the average B lifetime. B hadrons can be separated from charmed hadrons since the latter decay more rapidly, and because B hadrons have a larger mass, allowing for larger transverse components of the decay tracks' momenta. The parameters chosen for the tag are that three or more charged tracks miss the IP by more than 3σ in the plane perpendicular to the beam axis, where σ is the combined track measurement error and extrapolation uncertainty due to multiple scattering in the detector material. This tag is 61% efficient at a $Z^0 \rightarrow b\bar{b}$ purity of 89% [134].

Momentum-Weighted Track Charge

The decay axis of the Z^0 is approximated using the thrust axis of the event [136], using LAC energy clusters†. The task of finding the b quark flight direction reduces to one of finding which of the two directions along the thrust axis the b quark traveled, and which the $\bar{b}$. Techniques using leptons or charged kaons are effective at determining the sign of the b quark [46][50], but the subset of $Z^0 \to b\bar{b}$ decays for which these are present and confidently identified is not large. This analysis takes a more inclusive approach and uses a momentum-weighted sum of the charges of the tracks in each tagged event to identify the b flight direction.

The event momentum-weighted charge Q is defined to be

$$Q = -\sum_{tracks} q_i |\vec{p}_i \cdot \vec{t}|^{\kappa} \mathrm{sgn}(\vec{p}_i \cdot \vec{t}), \tag{6.2}$$

where $\vec{t}$ is the thrust axis, q_i and $\vec{p}_i$ are the ith track's charge and momentum, and κ is a parameter which may be adjusted to optimize the measurement sensitivity. This analysis chooses $\kappa = 0.5$, a choice to be discussed in Section 6.4.1. The sign of $\vec{t}$ is chosen to make Q positive, making $\vec{t}$ the estimator of the b quark direction.

This technique of signing a parton's charge has a long history. It was first suggested by Feynman and Field [29] to distinguish between up- and down-type quark jets in hadronic collisions, and was named "jet charge." Momentum-weighted charge has been successfully used in e^+e^- experiments at lower energies at PEP and PETRA [137], TRISTAN [138], and more recently at LEP energies [139].

The SLD Monte Carlo suggests that the sign of $\vec{t}$ is chosen correctly ~68% of the time, with better charge assignment when $\cos\theta$ is small, due to the CDC's acceptance. The correct-signing probability $P_{correct}$ can be expressed in terms of an "Analyzing Power" (AP):

$$AP = P_{correct} - P_{incorrect} = 2P_{correct} - 1 \sim 36\%. \tag{6.3}$$

AP dilutes the asymmetry from its electroweak value, described in Section 1.4.4, down to its measured value. The analyzing power AP depends on the details of B

†The LAC provides a minimally biased estimate of the original direction of the partons emitted by the Z^0. Using tracks reconstructed by the CDC would bias the measured thrust axes towards the center of the detector, because of the loss of acceptance at high angles. Furthermore, the LAC allows reconstruction of neutral energy, reducing the uncertainty in the event axis.

fragmentation at the Z^0, mixing and decay, as well as the detector response. Because of $\cos\theta$-dependent detector acceptance and radiative effects, AP must be estimated as a function of $\cos\theta$ using a Monte Carlo with full simulation of these effects.

Asymmetry and Fit

Once the events are b-tagged and the signed direction of the b in each one determined with momentum-weighted track charge, the left-right forward-backward asymmetry $\tilde{A}$ can be computed. Histograms binned in $\cos\theta_T$, the signed thrust axis, are accumulated separately with events produced with the left- and right-handed electron beams. Then

$$\tilde{A}_i^{obs} = \frac{N_{FL}^i - N_{BL}^i + N_{BR}^i - N_{FR}^i}{N_{FL}^i + N_{BL}^i + N_{BR}^i + N_{FR}^i} \tag{6.4}$$

is calculated in each $\cos\theta$ bin, indexed with the letter i, with L, R referring to the left- and right-handed beam helicity states, and F, B referring to events with positive and negative $\cos\theta_T$.

This observed asymmetry must first be corrected for expectations of light-flavor contamination of the tag, an additive effect on the asymmetry.

$$\tilde{A}_i^{corr} = \frac{\tilde{A}_i^{obs}}{\Pi_i} - \frac{1-\Pi_i}{\Pi_i}\tilde{A}_i^{light}, \tag{6.5}$$

where Π_i, the b-tag purity in each $\cos\theta$ bin, and $\tilde{A}_i^{light}$, the asymmetry of background events, are estimated from the Monte Carlo.

The corrected asymmetry $\tilde{A}_i^{corr}$ is directly proportional to $P_e A_b$ in each bin of $\cos\theta_T$, and the coefficient is the analyzing power AP. The fit proceeds by finding the asymmetry in each bin of $\cos\theta_T$ in a pure Monte Carlo sample of $Z^0 \to b\bar{b}$ events, with full modeling of B fragmentation and decay, mixing, gluon radiation, and initial-state photon radiation[‡]. The Monte Carlo asymmetries are compared with those in data, and an overall scale factor is determined for the Monte Carlo to determine the best fit. This scale factor constitutes a fully corrected measurement of A_b using a binned fit.

[‡]The QED corrections mentioned in Section 1.5 are not applied to the measurement in this chapter because their effects are included in the Monte Carlo simulation. They will be necessary in Chapter 7, though.

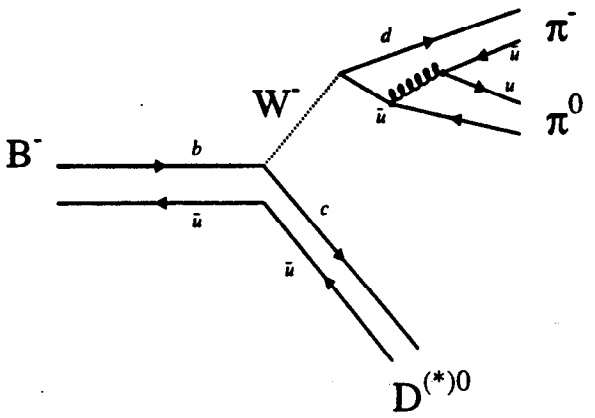

Figure 6.1: Feynman diagram of a typical B decay, $B^- \rightarrow D^{*0}\pi^+\pi^0$.

6.1.2 Why Momentum-Weighted Charge Works

While momentum-weighted charge was originally proposed to distinguish between light-flavored jets [29], heavy-flavored decays of the Z^0 provide a much more optimal setting for its use. The reasons for this are twofold. First, the B fragmentation function is extremely hard (see Figure 1.2 for a parameterization). The fraction of the beam energy a B meson receives from a Z^0 decay is on average ~70% [118][140], leaving relatively little energy for fragmentation tracks. When the B loses a large fraction of energy to hard gluon radiation, the gluon jet has an average charge of zero [141] and develops no preference when momentum-weighting is applied.

The second reason is that the process of B meson decay favors particles with charge correlated with that of the original b quark with high momentum. In general, a B decay contains $W^\pm$ products, a charmed spectator, and perhaps some soft tracks

from fragmentation of the spectator. The $W^{\pm}$ products, which come directly from the B meson decay vertex, have a net charge of -1 when the b quark itself has a charge of $-\frac{1}{3}$, and tend to have a high momentum in the laboratory, owing to the large mass of the recoiling spectator system and the available energy in the disintegration of the B. While the charmed spectator and its daughter products have a total charge that is anticorrelated with the original b, this is somewhat mitigated because the kaon into which the charmed hadron decays will have a charge that is positively correlated with the charge of the original b quark. Because charmed mesons do not mix appreciably [142], the charge sign is not diluted through this step. Figure 6.2 shows the average charge in bins of $\ln(P_{tot})$ for particles which originate at the B decay vertex, particles that originate at the cascade charm vertex (or vertices), and particles that originate at the Z^0 decay vertex. Because tracks with high momentum have more charge correlation with the originating quark, weighting the track charge with momentum improves the analyzing power.

An alternative approach to a track-charge analysis is to weight the charges with the rapidity of the tracks. This has been found to be about as effective as using momentum-weighting with $\kappa = 0.5$.

6.2 Experimental Results

6.2.1 Event Selection

The SLD trigger has an efficiency $\epsilon \geq 96\%$ [143] for accepting hadronic Z^0 decays, but it is also relatively efficient for backgrounds of various kinds. In addition, the Z^0 decays into final states which are not important for this analysis, such as the leptonic decays. The most serious background of the leptonic decay channels is the $\tau^+\tau^-$ final state. These events have a chance of passing the b-tag requirements because of the substantial lifetime of the τ lepton, and because the tracks have a high average momentum, which reduces the impact errors.

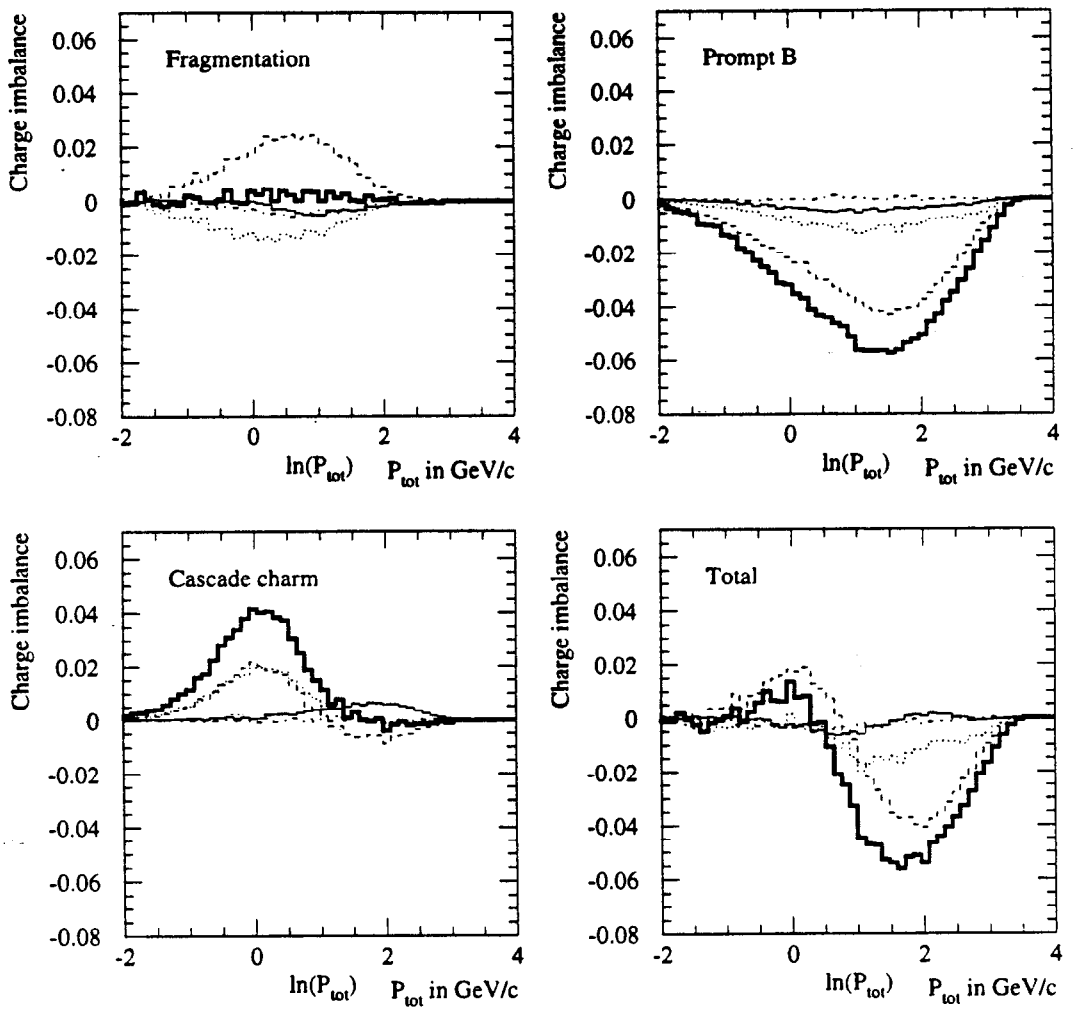

Figure 6.2: Average charge separation in bins of momentum for tracks from B decay, cascade D decay, and fragmentation, estimated with the SLD Monte Carlo. The histograms show the contributions from different species of B hadrons — dashed: B_u, dotted: B_d, dot-dashed: B_s, and solid: Λ_b. The bold histogram is the sum over all species. The sign-correlated tracks from the B decay vertex in general have more momentum than the oppositely-correlated tracks from the cascade charm decay vertex.

6.2.2 Trigger and Z^0 Filter

The first stage of event selection is the trigger applied online before the detector is read out. After the data are written to tape, they are quickly scanned by a filtering program, which applies loose calorimetric and tracking requirements on the events and writes a skimmed sample to tape. The combined trigger and filter efficiencies are estimated to be 93% [144][143]. Detailed descriptions of the trigger and filter are given in Appendix D.

During 1993, there was a flaw in one of the trigger requirements. A readout "veto" on triggers which incorporated tracking information, was configured improperly. The veto was designed to inhibit readout of the tracking chamber when the cell occupancy was too high, in order to reduce deadtime from accelerator backgrounds. The threshold was set too low from run 21573 to run 22553, from here on called the "veto period." This period lasted from April 30, 1993, to June 17, 1993, and comprises roughly 2/5 of the 1993 data sample. With this low threshold, the veto inhibited CDC readout on ~20% of hadronic Z^0 events, with a bias against reading out high-multiplicity events. It is unfortunate for heavy flavor analyses because $Z^0 \rightarrow b\bar{b}$ events have a higher average multiplicity than other hadronic decays and are therefore more likely to have been affected by this veto.

While the cell overflow veto is simulated in the Monte Carlo, it is more prudent to omit this data, as the vetoed sample's analyzing power may be different from that of the the non-vetoed sample.

6.2.3 Analysis Requirements

The filtered sample is too permissive a set to be useful for most analyses of the SLD data; only about 50% of it consists of hadronic Z^0 decays. A small fraction of it is mu pairs, tau pairs, and WAB's, with the remainder being combinations of various kinds of accelerator background. Each of the requirements listed in this section is designed to improve the purity of the hadronic Z^0 sample without introducing significant biases in the analysis results. Full detector displays of each of the different Z^0 decays can be seen in Figure 6.3.

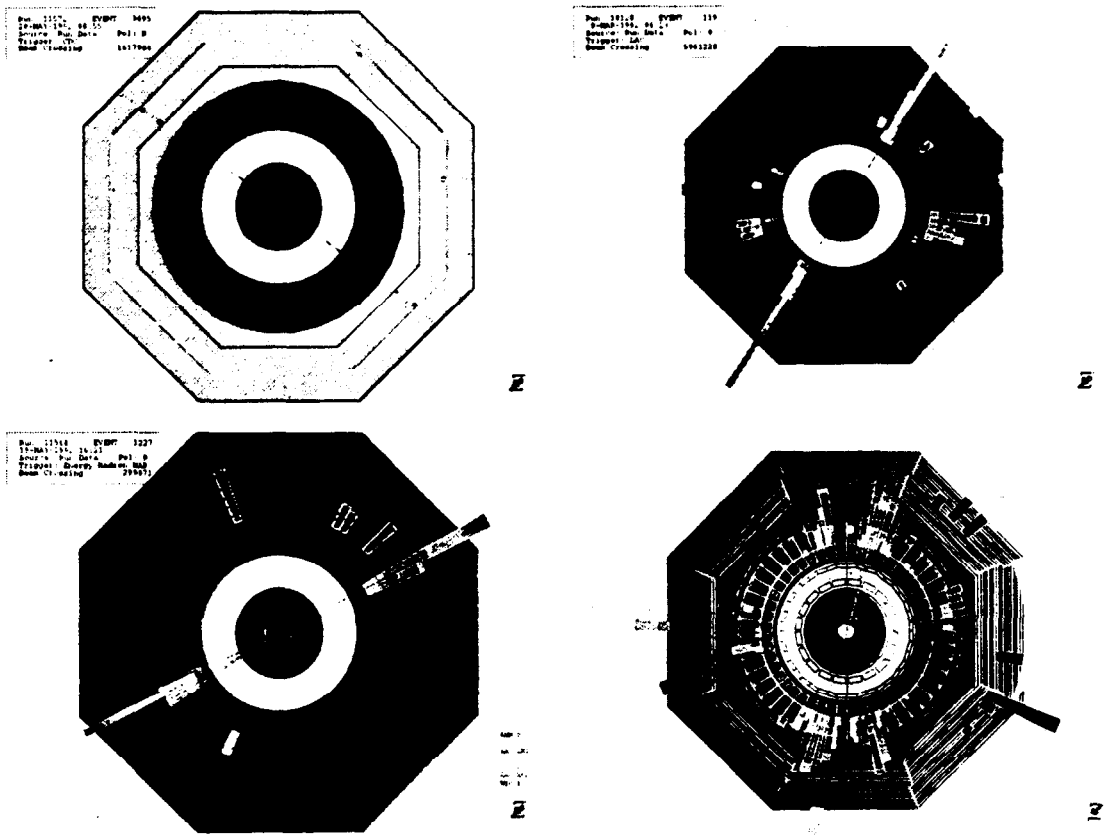

Figure 6.3: Different types of Z^0 decay. Clockwise from the upper left are $Z^0 \rightarrow \mu^+\mu^-$, $Z^0 \rightarrow e^+e^-$, $Z^0 \rightarrow \tau^+\tau^-$, and $Z^0 \rightarrow$hadrons.

Hadronic decays of the Z^0 tend to have high charged multiplicities and large amounts of energy in the charged tracks. Leptonic (e^+e^- or $\mu^+\mu^-$) decays nearly always have charged multiplicities of 2, while $Z^0 \rightarrow \tau^+\tau^-$ event decay multiplicities commonly reach up to 6. The event selection will therefore rely on tracking information from the CDC.

Track Selection

In order to select events based on their charged tracks, one needs to require that the tracks themselves originate near the interaction region and be measured well. This

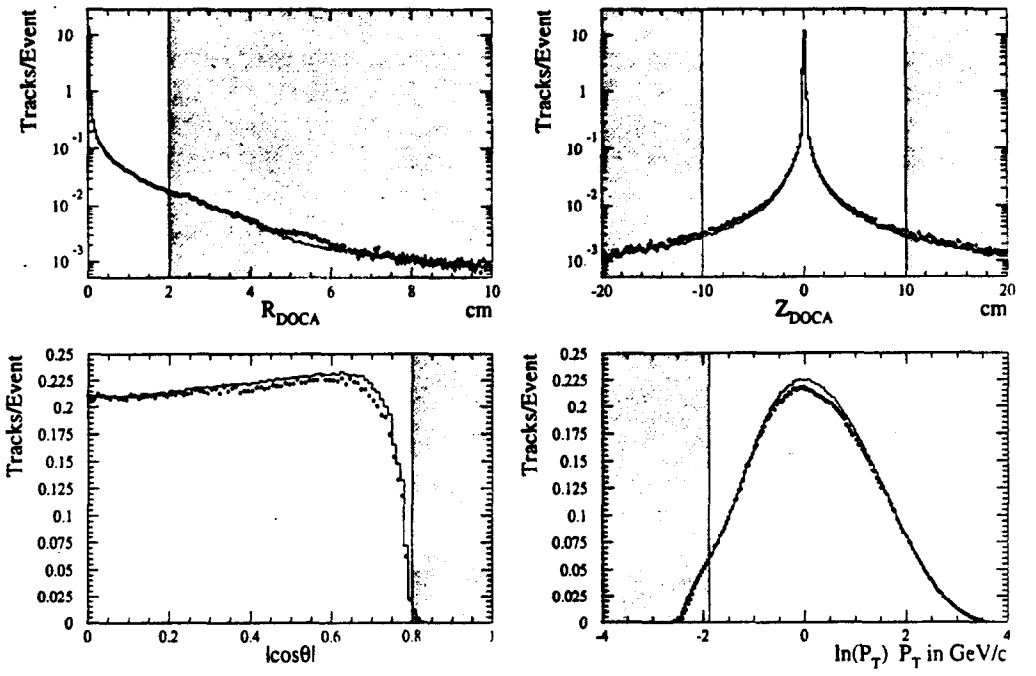

Figure 6.4: Distributions of the first four track selection variables (Equations 6.7–6.10). The data (points) are compared with the Monte Carlo (histogram). Shaded areas correspond to tracks which do not pass the selection criteria. In each plot, all track and event selection cuts have been applied except the one shown.

analysis requires that each track have

$$R_{DOCA} < 2.0 \text{ cm}, \tag{6.6}$$

$$Z_{DOCA} < 10.0 \text{ cm}, \tag{6.7}$$

$$|\cos\theta| < 0.8, \tag{6.8}$$

$$P_t > 150 \text{ MeV/c}, \tag{6.9}$$

$$R_{inner\ hit} < 45 \text{ cm}, \tag{6.10}$$

$$N_{hits} > 39 \text{ of a possible } 80, \tag{6.11}$$

$$\chi^2/DOF < 5.0, \text{ and} \tag{6.12}$$

$$P_{tot} < 50 \text{ GeV/c}, \tag{6.13}$$

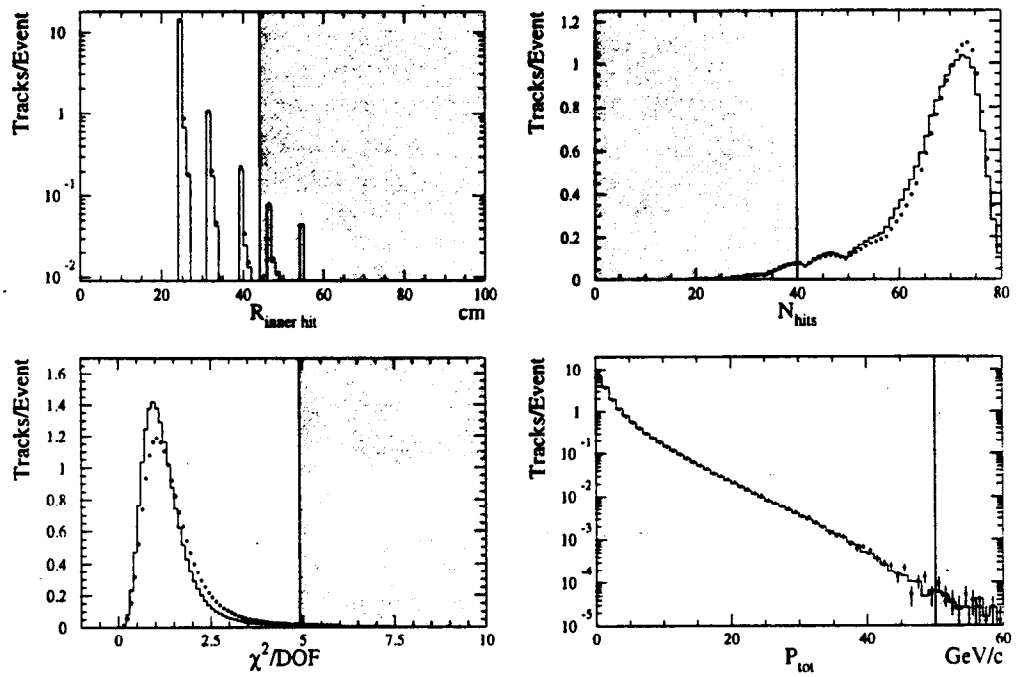

Figure 6.5: Distributions of the second four track selection variables (Equations 6.11–6.13). The data (points) are compared with the Monte Carlo (histogram). Shaded areas correspond to tracks which do not pass the selection criteria. In each plot, all track and event selection cuts have been applied except the one shown.

where R_{DOCA} is the x-y radius of the track at its point of closest approach to the beamline, Z_{DOCA} is the z coordinate of the same location, with $z = 0$ within a few millimeters of the average IP position, P_t is the momentum transverse to the beam axis, and $r_{inner\ hit}$ is the x-y radius of the CDC hit closest to the beampipe. The purpose of the first two cuts above is to reject tracks that do not originate from the interaction point. One of the largest sources of extraneous charged tracks in the detector is the pair of tungsten synchrotron radiation masks M4, located at $z = \pm 40$ cm from the IP [145]. Inelastic scattering in detector material of particles from Z^0 decay and stray particles from the beam also fall into this category. Figure 6.4 shows the R_{DOCA} and Z_{DOCA} distributions before cuts.

The acceptance of the CDC falls very quickly outside of $|\cos\theta_{track}| = 0.75$, with

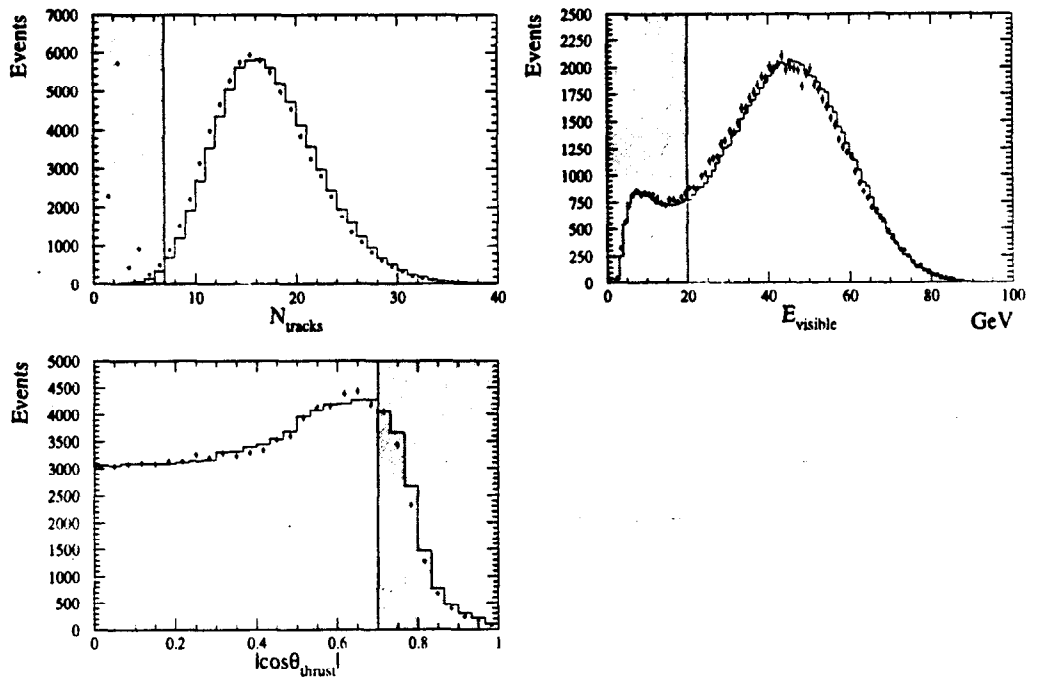

Figure 6.6: Distributions of the event selection variables (Equations 6.15–6.16). The data (points) are compared with the Monte Carlo (histogram). Shaded areas correspond to events which do not pass the selection criteria. In each plot, all track and event selection cuts have been applied except the one shown.

virtually no tracks left outside of $|\cos\theta| = 0.8$, where an expected 7 out of 10 layers are fully hit by the track. In this sense, the cut on $\cos\theta_{track}$ is almost not a cut at all. save for the fact that any track with $|\cos\theta| > 0.8$ probably has not been reconstructed properly, or has come from some place other than the IP. This cut is also correlated with the cut on N_{hits}, and so contributes little.

The cut on P_t serves two purposes. A large fraction of the beam-related background tracks have very low momentum transverse to the beam. Electromagnetic backgrounds such as Compton scatters from synchrotron radiation photons in the detector material have very low P_t on this scale [145]. Tracks with P_t under ~100 MeV also loop back into the tracking chamber and the track reconstruction may split them into multiple track segments.

The radius of the closest hit requirement mainly rejects K_s^0 and Λ decay product tracks that started midway through the CDC and may not be well measured. It also rejects the second halves of tracks that kinked because of decays or scatters and were split into two pieces. It is not a completely orthogonal cut to the N_{hits} cut, which ensures that the track have enough measured points to determine the track parameters reliably. The χ^2 cut attempts to reject tracks that have too many hits that were incorrectly assigned to them, and tracks that kinked but were not split into two tracks. If a track has a measured momentum greater than 50 GeV/c, then it was probably mismeasured, perhaps due to a kink in the track, or hits that were taken from other tracks. The momentum measurement error of 45 GeV/c tracks with CDC-only information is 10.1 GeV, as given by Equation 6.29; the error drops by a factor of two when VXD information is added.

Event Selection

Once a set of clean tracks has been found, events are selected based on it. The requirements for this analysis are

$$N_{tracks} \geq 7, \tag{6.14}$$

$$E_{visible} \geq 20 \text{ GeV}, \quad \text{and} \tag{6.15}$$

$$|\cos\theta_{thrust}| < 0.7, \tag{6.16}$$

where $E_{visible}$ is the sum of the energies in charged tracks passing the above criteria. assuming each has the mass of a pion, and θ_{thrust} is the polar angle of the thrust axis found using energy clusters in the LAC. Because the N_{tracks} requirement is based on selected tracks, it is effective in eliminating beam-related background triggers in which no tracks come from the interaction point. The cut of 7 tracks was chosen to remove nearly all of the $Z^0 \to \tau^+\tau^-$ background without too significant a loss of hadronic efficiency. The cut at 7 tracks requires at least one of the taus in the event to have a five-prong decay (the other must have at least three prongs in its decay), or for some tracks to be misreconstructed. The five-prong branching fraction of taus is $(1.25 \pm 0.24)^{-3}$ [146], and the three-prong fraction is $(14.38 \pm 0.24)\%$, and $\Gamma(Z^0 \to \tau^+\tau^-)/\Gamma(Z^0 \to \text{hadrons}) \simeq 4.8\%$, so the contamination is expected to be

very small. A Monte Carlo study indicates that the efficiency of the event selection for $Z^0 \rightarrow \tau^+\tau^-$ events is (0.77±0.09)%, and that therefore the $Z^0 \rightarrow \tau^+\tau^-$ contamination is $(0.09 \pm 0.01)\%$. Similar Monte Carlo studies indicate that the selection efficiency for WABs is 0.02% and the selection efficiency for 2γ events is $< 0.02\%$. Dimuon events are expected to be less efficient than WAB's, owing to less final-state radiation and bremsstrahlung in the detector material to convert into e^+e^- pairs.

The visible energy cut is also designed to help eliminate beam-related backgrounds and 2γ events, as tracks within the detector acceptance for these triggers tend to be very soft. A comparison of this variable in data and Monte Carlo with all other selection cuts applied is shown in Figure 6.6. The cut on the polar angle of the thrust axis is applied to improve the quality of the tagged event sample. Because the coverage of the vertex detector extends only to tracks with $|\cos\theta| < 0.75$[§] [112], any event with a LAC thrust axis far beyond that is likely to have suffered severe QCD radiation or have large calorimeter backgrounds.

The efficiency of these cuts can be estimated from Monte Carlo to be ~60%, with the main inefficiency in this selection coming from the cut on $|\cos\theta_{thrust}|$. When the events are analyzed, only the tracks passing the selection criteria are used. A total of 15,858 hadronic events pass event selection in the 1993 sample (omitting the veto period). The total for 1994–1995 is 59,430 events.

6.2.4 B Tagged Sample

To take advantage of the large mass and long lifetime (~1.5 ps) of the B hadrons and of the fine resolution of the SLD tracking chambers, this analysis employs a 2-dimensional signed impact parameter tag to identify $Z^0 \rightarrow b\bar{b}$ events. This tag has been described in detail elsewhere [134][147]. The tracks and the beam spot are projected into the plane perpendicular to the beam axis for purposes of the tag. Because the impact parameter resolution is dependent on the momentum of the track and its dip angle, which together determine how severe the multiple scattering is expected

[§]While the innermost layer of the VXD extends out to $|\cos\theta| < 0.85$, tracks are not guaranteed to hit it. One-hit VXD coverage extends roughly to $|\cos\theta| = 0.80$.

to be in the beampipe and detector material, this analysis uses the normalized impact parameter b/σ_b, the impact parameter divided by its measurement error, as the indicator of significance.

The sign of the impact parameter b is chosen with the aid of jets formed from reconstructed tracks using the JADE algorithm [148], with $y_{cut} = 0.02$. A low y_{cut} is chosen to prevent combining distinct jets together into larger ones with less angular resolution.

If the 2-dimensional projection of a track intersects its jet's axis on the same side of the IP as the track's flight path, then the impact parameter is signed positive. In the converse case, the track appears to have originated on the far side of the beam spot, and it is given a negative impact parameter. Because the boost of the heavy mesons is large at the Z^0, virtually no tracks at all will originate on the far side of the IP relative to the direction in which they travel. The negative side of the impact parameter distribution is therefore a measure of the resolution and correct-signing of the impact parameters alone.

In order to ensure that the tracks used in the tag have well-measured impact parameters, additional requirements are applied to the tracks. They are:

$$N_{VXDhits} \geq 1, \tag{6.17}$$

$$b < 3 \text{ mm, and} \tag{6.18}$$

$$\sigma_b < 250\ \mu m, \tag{6.19}$$

where $N_{VXDhits}$ is the number of clusters in the Vertex Detector associated with the track, and b is the impact parameter. Distributions of these variables are found in Figure 6.7. In addition, tracks identified as a decay product of a K^0 or a Λ, or the product of a γ conversion in detector material, are omitted from the tag analysis. These additional requirements are not applied for the tracks used in the momentum-weighted charge, as the loss of even one track in the selection cuts due to a scatter or a mislink to VXD hits will reduce the probability that the event will be signed correctly.

The normalized impact parameter distribution is shown in Figure 6.8 for 1994 data and Monte Carlo. Figure 6.9 shows a breakdown by flavor of the normalized

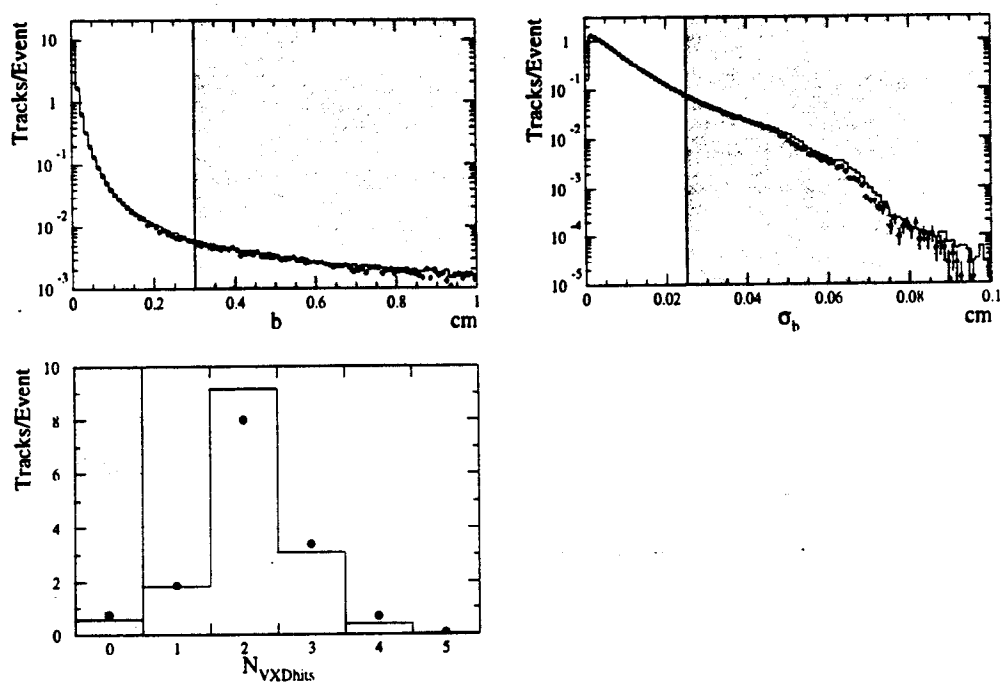

Figure 6.7: Distributions of vertexing-quality track cut variables. The data are shown as points and the Monte Carlo simulation values are shown as histograms. Data in the shaded regions are rejected by the track selection for purposes of B-tagging only.

impact parameter distributions as estimated in the Monte Carlo. No extra smearing of the Monte Carlo distributions has been applied, although because the data and Monte Carlo multiplicity distribution of Figure 4.4 do not match, an *ad hoc* tracking inefficiency has been applied to the Monte Carlo.

To tag an event, three tracks or more are required to have normalized impact parameters $b/\sigma_b > 3.0$. An event which has many tracks with highly significant impact parameters is shown in Figure 6.10. The performance of this tag can be seen in Figure 6.11, where the composition of the Monte Carlo is shown as a function of the number of such tracks. The total rate as a function of the number of significant tracks can be compared between data and Monte Carlo. The estimated efficiency of the tag is 61% and the purity is 89%, with nearly all of the contamination, 10%.

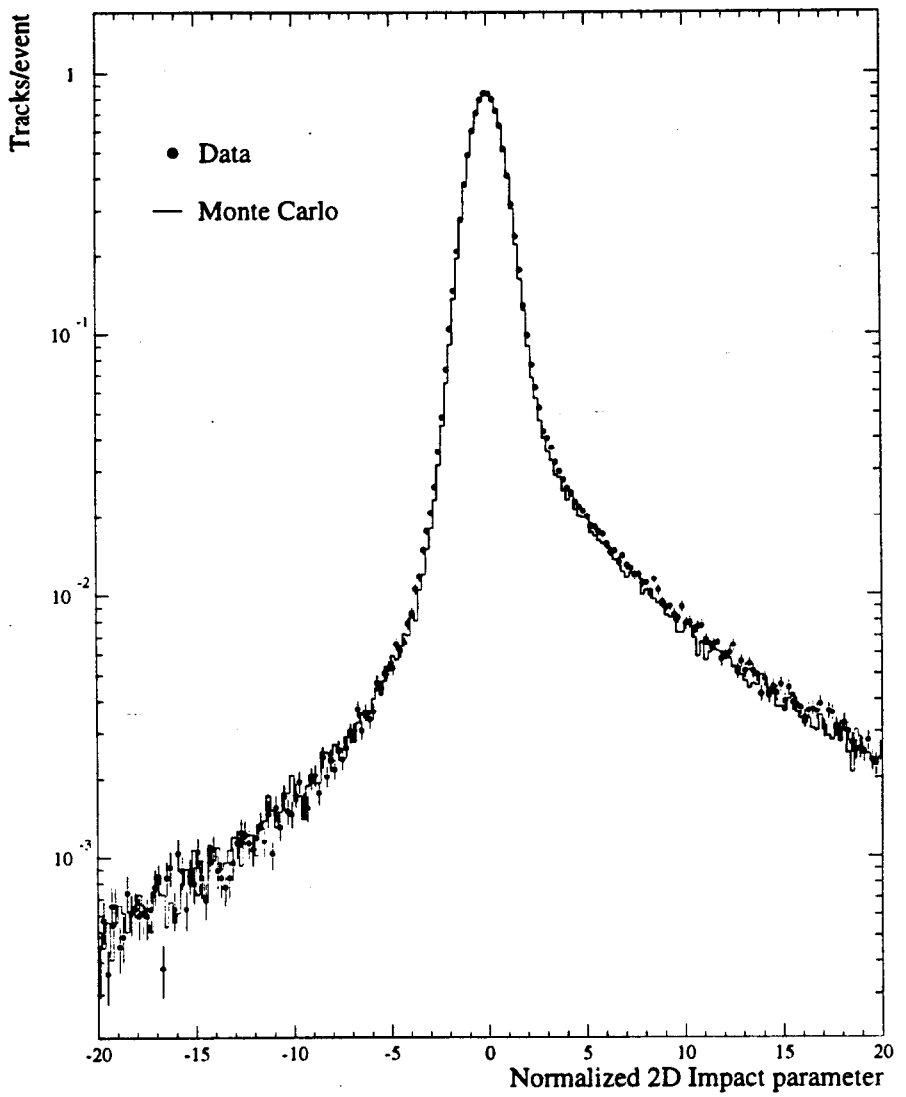

Figure 6.8: Comparison of the normalized 2D impact parameter in data (points) and Monte Carlo (histogram). No smearing of the Monte Carlo has been applied. Visible discrepancies in this distribution affect the b-tag rate. Systematic errors on the tag are discussed in Section 6.2.5.

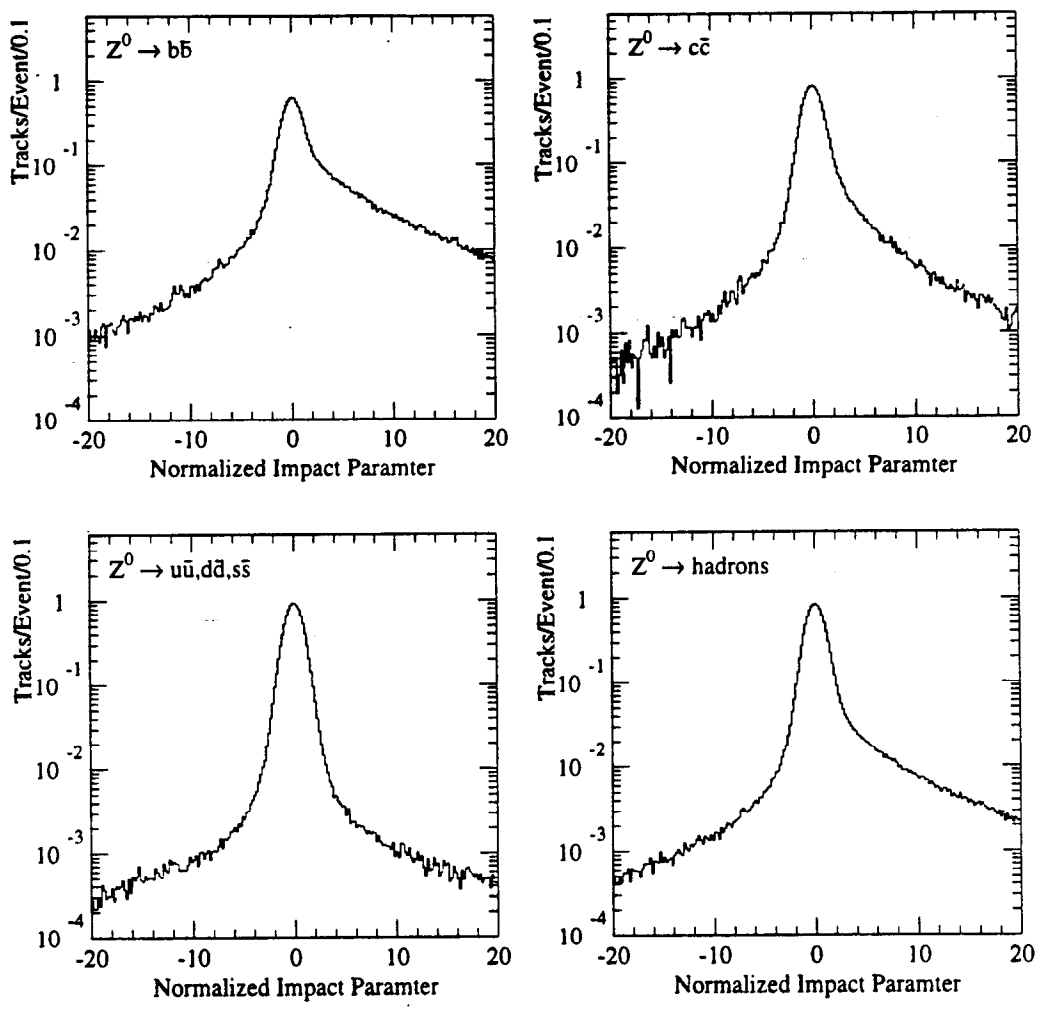

Figure 6.9: Normalized 2D impact parameter distributions estimated for each flavor of hadronic Z^0 decay in the SLD Monte Carlo.

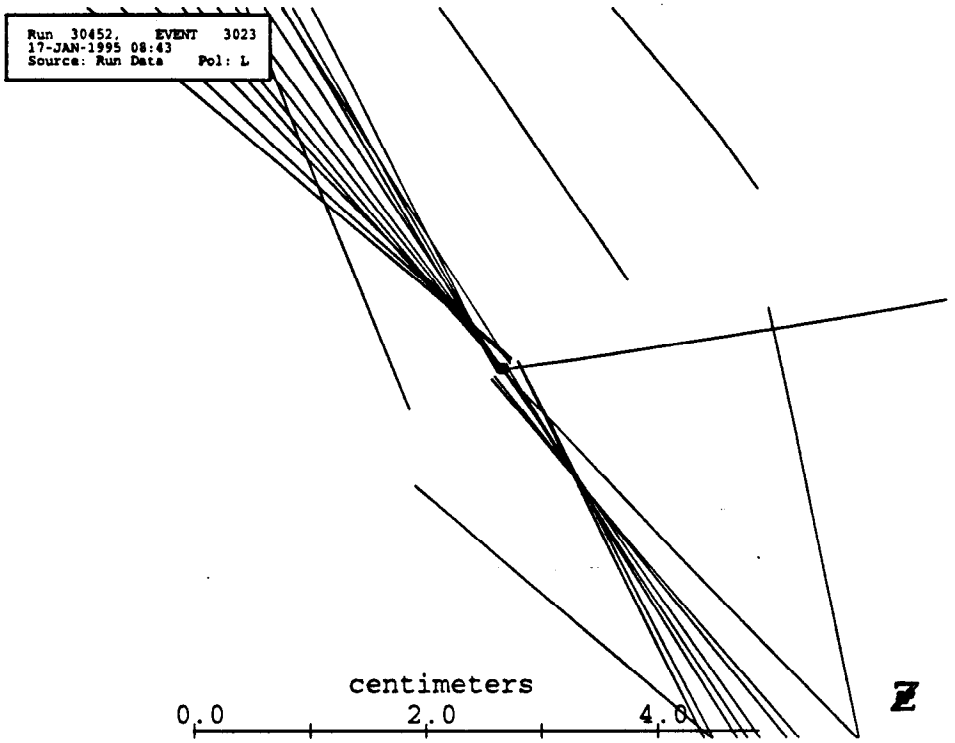

Figure 6.10: An event tagged with the normalized 2-D impact parameter tag. In this case, there are enough tracks with significant impact paramters to distinguish at least one displaced vertex in each hemisphere. The beam spot lies in the center of the square box with an error of 6μm in both directions in this projection.

coming from $Z^0 \rightarrow c\bar{c}$ events, and only 1% from $Z^0 \rightarrow uds$ events.

The fraction of events tagged in the data is $(15.96 \pm 0.13)\%$ for events retained by the hadronic event selection. A Monte Carlo study indicates that $(7.3 \pm 3.2)\%$ $Z^0 \rightarrow \tau^+\tau^-$ decays which pass event selection also pass the 2-D impact parameter tag. The total estimate of the fraction of $Z^0 \rightarrow \tau^+\tau^-$ events in the tagged sample is $(0.04 \pm 0.02)\%$.

The tagged event sample consists of 2,504 events in the 1993 data set, and 9,241 events in the 1994–1995 data set.

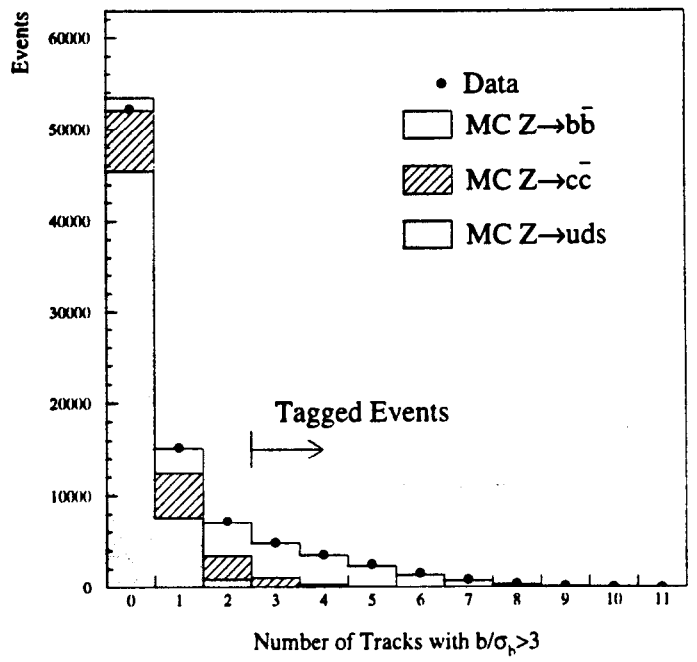

Figure 6.11: Performance of the 2-Dimensional Normalized Impact-Parameter Tag

6.2.5 Systematic Uncertainties on the B Tag

The performance of the 2-D normalized impact parameter tag is affected by the properties of the SLD tracking systems and by the underlying processes of B fragmentation and decay; additional model dependence comes from the simulation of $Z^0 \rightarrow c\bar{c}$ events and gluon splitting.

Because the Monte Carlo simulation of the tag provides the estimation of the purity of the $Z^0 \rightarrow b\bar{b}$ sample and also the composition of the contaminating fractions, it is crucial that the simulation be correct, and that conceivable deviations between the model and the true processes be well understood. In addition, the sensitivity of the analysis to the model parameters which may not be well constrained must be evaluated, and errors propagated through the A_b measurement.

The only property of the tag to which this analysis is sensitive is the composition.

Table 6.1: Systematic errors of the 3-tracks at 3σ 2-D impact parameter tag, after Reference [134].

Detector Modeling		$\delta\epsilon_b/\epsilon_b$ (%)	$\delta\Pi_b/\Pi_b$ (%)
Tracking & Linking efficiency		2.9	0.32
Tracking resolution		< 0.1%	< 0.1%
Trigger & Event Selection		0.5	0.06
Beam position tails		0	0.5
Physics Modeling	Variation		
B lifetimes	$\tau_{B_{meson}}$=1.55±0.10ps, $\tau_{B_{baryon}}$=1.10±0.30ps	2.6	0.29
b fragmentation	Peterson $\langle x_e \rangle = 0.695 \pm 0.021$	2.2	0.24
b fragmentation	Bowler *vs.* Peterson at $\langle x_e \rangle = 0.695$	0.2	0.02
b baryon production	(8.9±3.0)%	0.6	0.07
B decay to D^+	(±6% absolute)	0.3	0.03
B decay multiplicity	±0.25 tracks per B decay	2.2	0.24
B model	Phase space *vs.* Tuned JETSET 6.3	0.7	0.08
c fragmentation	Peterson $\langle x_e \rangle$ for D^* = 0.501 ± 0.025	0	0.5
c fragmentation	Bowler *vs.* Peterson at $\langle x_e \rangle = 0.501$	0	0.1
c decay to D^+	±5% absolute	0	< 0.1%
c decay multiplicity		0	0.9
s production	$s\bar{s}$ popping ±10%	0	0.3
uds decay multiplicity	±0.3 tracks	0	0.1
$g \to b\bar{b}$ splitting	±50% of JETSET	0	0.5
$g \to c\bar{c}$ splitting	± 50% of JETSET	0	0.3
$\Gamma(Z^0 \to c\bar{c})$	$R_c = 0.171 \pm 0.017$	0	1.0
Jet axis modeling	JADE y_{cut} varied from 0.01 to 0.10	0.8	.09
Total		5.2%	1.8%

Some sensitivity to the efficiency comes from its effect on the purity, through the following relation

$$\Pi_b = \frac{R_b \epsilon_b}{R_b \epsilon_b + R_c \epsilon_c + (1 - R_b - R_c)\epsilon_{uds}}, \tag{6.20}$$

where Π_b is the tag purity, and ϵ_b is the tag efficiency. Systematic uncertainties for the efficiency and composition of the 2-D normalized impact parameter tag have been estimated in reference [134] and are presented in Table 6.1, with their resulting effects on just the B tag purity.

The discrepancies visible in Figures 6.8 and 6.11 result in a ~5% higher tag fraction in the data than in the Monte Carlo. Given that largest errors in the tag rate come from uncertainties in ϵ_b and not the purity, these discrepancies are of less concern for the measurement of A_b.

Because the tag is nearly 90% pure in $Z^0 \rightarrow b\bar{b}$ decays and nearly all of the contamination comes from $Z^0 \rightarrow c\bar{c}$events, the largest contributions come from uncertainties in R_c and the modeling of charm decays. Uncertainties in the B tagging efficiency are scaled down by roughly 0.1 in their effect on uncertainties on the B purity.

6.2.6 Momentum-Weighted Charge Distributions

Because the binned asymmetry fit technique uses the Monte Carlo to estimate how often the momentum-weighted track charge of Equation 6.2 signs the events properly, it is important to verify that the Monte Carlo reproduces the distribution of that variable. The comparison must be made with $|Q|$, where Q is defined in Equation 6.2. The distribution of a signed Q would introduce the polarization and A_b; the unsigned distribution depends only on the details of fragmentation, decay, and detector response.

The Q distribution, shown in Figure 6.12, fits to a Gaussian with zero mean, with $\chi^2 = 43.4$ for the data, and $\chi^2 = 56$ for the Monte Carlo, both with 28 degrees of freedom[¶]. The width of the Q distribution in data is (4.187 ± 0.025) $(\mathrm{GeV})^{\frac{1}{2}}$, and that of the data is (4.330 ± 0.015) $(\mathrm{GeV})^{\frac{1}{2}}$. The property that Q is nearly Gaussian will aid in the calibration of the analyzing power in the next chapter.

[¶]In fact, the distribution of Q is not expected to be perfectly Gaussian even if the underlying momentum-weighted charge distributions are. This point will be brought up in detail in Chapter 7.

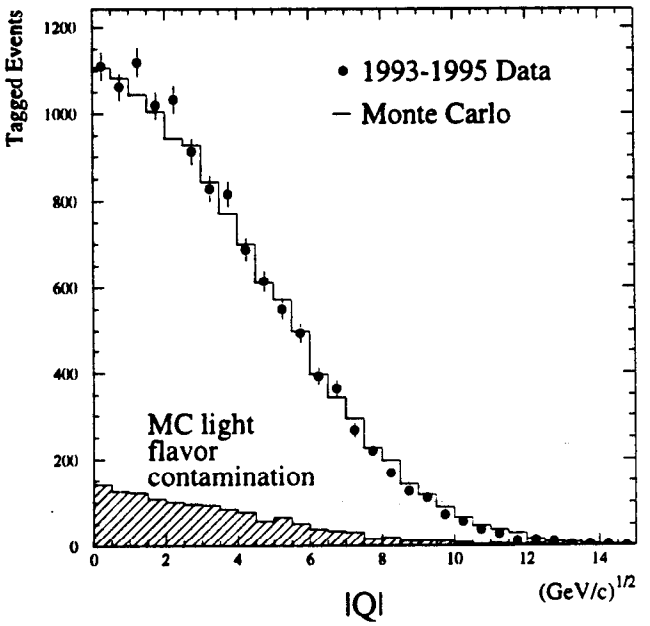

Figure 6.12: Momentum-Weighted Charge comparison of data and Monte Carlo for tagged events. The momentum-weighting exponent κ is set to 0.5. The Monte Carlo distribution is broken down into a signal ($Z^0 \rightarrow b\bar{b}$) subsample, shown as a histogram, and contamination from light flavored hadronic decays, shown hatched. Only the absolute value is shown, so as not to bias the comparison with asymmetry-dependent information.

A second quantity can be formed which yields information about the material in the detector. The quantity

$$Q_{sum} = \sum_{tracks} q_i |\vec{p}_i \cdot \vec{t}\,|^{\kappa} \tag{6.21}$$

ignores whether a track went into the forward hemisphere or the backward hemisphere, and therefore contains no information about the measured asymmetry. Furthermore, it is a signed quantity, and its average value is an indication of the contribution of extra positive charged tracks due to interactions with detector material of the particles originating at the Z^0 decay. This distribution, shown in Figure 6.13, is also nearly Gaussian with a mean of 0.088 ± 0.033 (GeV)$^{\frac{1}{2}}$ and a width of 3.654 ± 0.024

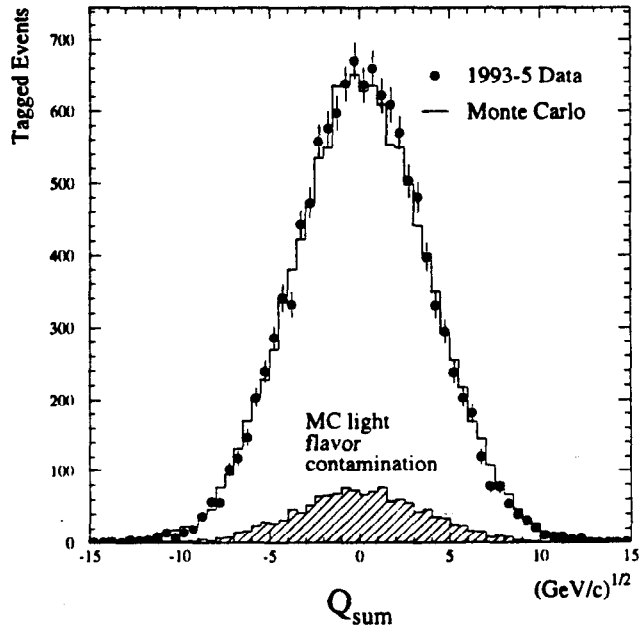

Figure 6.13: Distribution of Q_{sum} for tagged events, compared between data and Monte Carlo. The Monte Carlo $Z^0 \rightarrow b\bar{b}$ contribution is shown in the clear histogram, while the light-flavor Z^0 decays are shown in the hatched histogram.

(GeV)$^{\frac{1}{2}}$ in the data, and a mean of 0.010 ± 0.020 (GeV)$^{\frac{1}{2}}$ and a width of 3.774 ± 0.014 (GeV)$^{\frac{1}{2}}$ in the Monte Carlo. The χ^2 values are 48.4 and 70.1 for 51 degrees of freedom in the data and Monte Carlo, respectively. This width will become important later in the maximum-likelihood fit, as it carries information about the analyzing power.

6.2.7 Asymmetry Fit

Once the momentum-weighted charge Q, defined in Equation 6.2, has been calculated for the tagged events and the thrust axis signed, the left-right forward-backward asymmetry may be formed. To demonstrate the large asymmetry present in the Q-signed data sample, the events are binned in $\cos\theta$ separately for events produced when the electron beam was left- and right-handed polarized, shown in Figure 6.14.

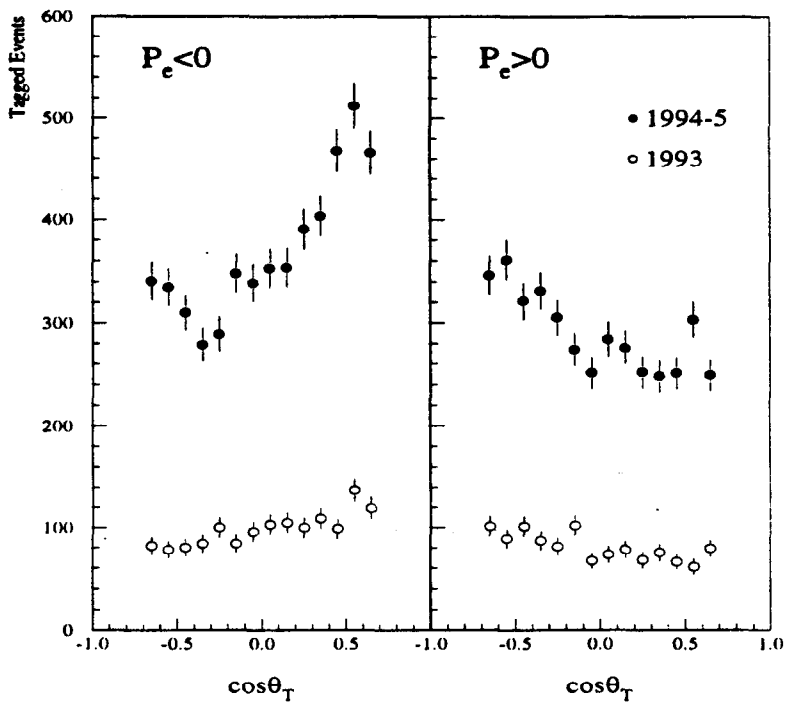

Figure 6.14: Calorimetric thrust axis $\cos\theta$, signed with momentum-weighted track charge. binned separately for events created with the left-handed and right-handed e^- beams. The effects of the increased polarization from 63% (1993) to 77% (1994–5), and the larger data sample in 1994–5, are visible.

The Standard Model prediction of the forward-backward asymmetry is larger for the events produced with the left-handed beam than for the right-handed beam. One may also see the effects of A_{LR} — the Z^0 production cross-section is larger for the left-handed electrons than for right-handed electrons. There are 6,565 tagged events produced when the e^- beam was left-handed and 5,180 tagged events produced when the e^- beam was right-handed in the 1993–1995 data sample.

The left-right forward-backward asymmetry is then formed as prescribed by Equation 6.4. The Monte Carlo is used to estimate the contamination fraction and asymmetry in each bin of $\cos\theta$. The contamination asymmetry is then subtracted from the data asymmetry according to Equation 6.5. Typically, the background asymmetry has a value of -0.75 times the signal asymmetry. The sign is negative because the

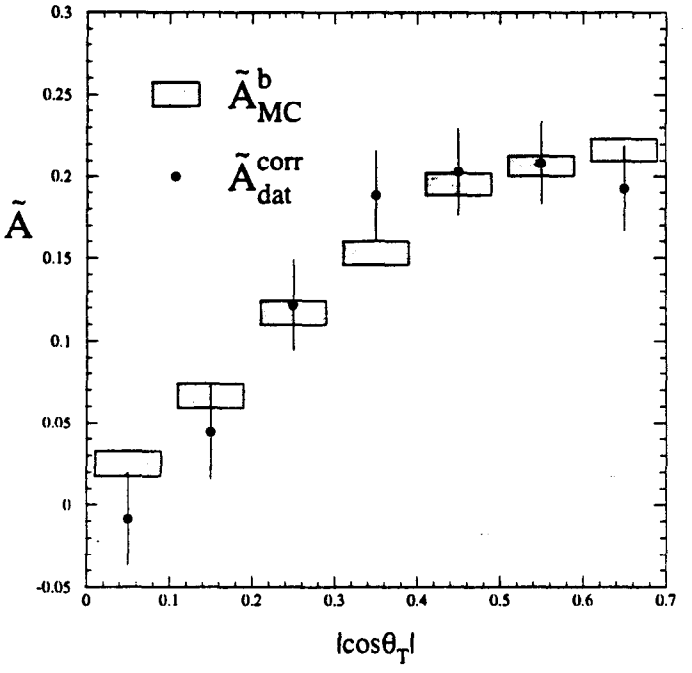

Figure 6.15: Binned fit of the MC asymmetry to the data asymmetry, taking into account $\cos\theta_T$-dependent effects on the analyzing power. The Monte Carlo statistical error is indicated by the shaded regions.

background is dominated by $Z^0 \to c\bar{c}$ events, and the value is less than unity because $A_c < A_b$, and because $Z^0 \to c\bar{c}$ events are expected to have less analyzing power on average than $Z^0 \to b\bar{b}$ events. This results in a bin-by-bin correction of approximately 21%. The correctness of the modeling necessary to subtract the contamination properly may be tested by repeating the entire analysis with stronger and weaker tags, the results of which are described in Section 6.4.2.

There remains a large amount of ordinary physics and detector processes which affect the measurement of A_b with momentum-weighted track charge, and therefore must be accounted for with a detailed simulation. These effects include tracking efficiency, $B^0 - \overline{B}^0$ mixing, charge dilution from the properties of the B decay process.

fragmentation tracks, stray particles produced by interactions with the detector material, thrust-axis resolution, radiation of hard gluons, heavy quark pair splitting from gluons, and initial state radiation. These effects are simulated by the SLD Monte Carlo, which incorporates a full implementation of JETSET 7.4, with the decays of B mesons taken care of by the CLEO B-decay model. The decay tables of the D mesons have also been altered from the default JETSET values in order to agree better with available measurements, and are presented in Chapter 5. The average B mixing parameter χ_B is 0.130 in the SLD Monte Carlo, with near saturation of B_s mixing, and $\chi_d = 0.180$ for the B_d meson alone.

While all of the known "ordinary" physics effects which may dilute the observed asymmetry are modeled in the Monte Carlo, it is important to evaluate how much of an effect each is contributing to the answer, and to estimate the uncertainties in each, which will be the subject of the next section. Another important feature of most of these corrections is that they depend on the polar angle. Because the underlying asymmetry also has a dependence on polar angle given by Equation 1.72, and therefore the different bins in $\cos\theta$ receive different weights in the fit, these effects must be taken into account separately in each bin of $\cos\theta$. Fortunately, though, the asymmetry in each bin scales proportionally with $P_e A_b$, and therefore a simple scaling fit of the Monte Carlo asymmetry to the data asymmetry is justified. The Monte Carlo is then run at $P_e = \pm 100\%$ and $A_b = 1.0$[‖], and the measured A_b is given by

$$A_b = \frac{1}{\langle P_e \rangle_{\mathcal{L}}} \left(\frac{\sum_i \tilde{A}_i^{corr} \tilde{A}^b_{MC,i} / \sigma_i^2}{\sum_i \left(\tilde{A}^b_{MC,i} \right)^2 / \sigma_i^2} \right), \tag{6.22}$$

where $\langle P_e \rangle_{\mathcal{L}}$ is the luminosity-weighted electron beam polarization, and $\tilde{A}^b_{MC,i}$ is the left-right forward-backward asymmetry calculated in bin i of $\cos\theta$ in the Monte Carlo. for a pure sample of $Z^0 \to b\bar{b}$ events that have been tagged. Typically $\tilde{A}^b_{MC,i}$ is ~36% of the raw cross-section asymmetry in its bin, corresponding to a correct-sign fraction

[‖]In practice, the Monte Carlo is run with $A_b^{MC} = 0.9357$ and the resulting fit value of A_b is multiplied by A_b^{MC}. In addition, the SLD Monte Carlo is generated with equal quantities of left-handed events and right-handed events. This unphysical situation affects the calculation of $\tilde{A}$ in the MC, and therefore must be adjusted to reflect $A_{LR} \simeq 0.15$ by removing a fraction of the right-handed events, as described in Section 5.2.

of ~68%. The bins are weighted by the statistical error on the data measurements σ_i, which is given by a binomial error expression

$$\sigma_i = 2\sqrt{\frac{(N^i_{FL}+N^i_{BR})(N^i_{BL}+N^i_{FR})}{(N^i_{FL}+N^i_{BR}+N^i_{BL}+N^i_{FR})^3}}, \tag{6.23}$$

in each bin of $\cos\theta$. The statistical error used in the fit is magnified by the correction for light-flavor contamination as prescribed by Equation 6.5:

$$\sigma^i_{\tilde{A}^{corr}} = \frac{\sigma^i_{\tilde{A}^{obs}}}{\Pi^i_b}, \tag{6.24}$$

also calculated separately in each bin of $\cos\theta$. The statistical error on the fit for A_b in Equation 6.22 is given by

$$\delta A_b(\text{stat.}) = 1/\left(\langle P_e\rangle_{\mathcal{L}}\sqrt{\sum_i\left(\tilde{A}^b_{MC,i}\right)^2/\sigma_i^2}\right). \tag{6.25}$$

Using a luminosity-weighted polarization of

$$\langle P_e\rangle_{\mathcal{L}} = 0.739, \tag{6.26}$$

averaged over 1993–1995 data (omitting the 1993 veto period), the value fit by this procedure is

$$A_b = 0.828 \pm 0.054(\text{stat.}) \tag{6.27}$$

The statistical error scales as $1/\left(P_e \cdot AP \cdot \sqrt{N}\right)$, with much of the magnification coming from $1/AP$. Gains in sensitivity can often be made more quickly by improving AP than by collecting more data. This is the strategy taken by the semileptonic analyses and the inclusive kaon analysis, although the efficiency of the impact-parameter tag compensates in this case for the loss of analyzing power incurred by using momentum-weighted track charge.

6.3 Systematic Error Analysis

Systematic errors on the measurement of A_b arise from parts of the analysis in which a model is used to interpret the data. The most important of these is the binned

Table 6.2: Details of the binned asymmetry fit for A_b. $\tilde{A}^b_{MC}$ is tabulated as if $A_b = P_e = 1.00$ in the Monte Carlo; $\tilde{A}^{light}_{MC}$ is reported at the correct luminosity-weighted polarization and assumes Standard Model couplings, so that it may be directly used in Equation 6.5.

$\cos\theta_T$	$\tilde{A}^{obs}$	$\tilde{A}^{light}_{MC}$	Π_b	$\tilde{A}^{corr}$
0.0–0.1	-0.011 ± 0.025	-0.032	0.887	-0.009 ± 0.028
0.1–0.2	0.030 ± 0.024	-0.064	0.879	0.043 ± 0.028
0.2–0.3	0.106 ± 0.025	-0.030	0.898	0.121 ± 0.028
0.3–0.4	0.151 ± 0.025	-0.131	0.888	0.187 ± 0.028
0.4–0.5	0.166 ± 0.024	-0.127	0.892	0.201 ± 0.027
0.5–0.6	0.171 ± 0.023	-0.142	0.898	0.207 ± 0.025
0.6–0.7	0.158 ± 0.023	-0.119	0.892	0.191 ± 0.026

$\cos\theta_T$	$\frac{2\cos\theta_T}{1+\cos^2\theta_T}$	$\tilde{A}^b_{MC}$	$\langle P_e\rangle_{\mathcal{L}} \cdot \tilde{A}^b_{MC}$
0.0–0.1	0.010	0.041 ± 0.012	0.030 ± 0.009
0.1–0.2	0.293	0.108 ± 0.012	0.080 ± 0.009
0.2–0.3	0.471	0.190 ± 0.012	0.140 ± 0.009
0.3–0.4	0.624	0.249 ± 0.011	0.184 ± 0.008
0.4–0.5	0.748	0.317 ± 0.011	0.235 ± 0.008
0.5–0.6	0.846	0.335 ± 0.010	0.248 ± 0.008
0.6–0.7	0.914	0.352 ± 0.011	0.260 ± 0.008

asymmetry fit which accounts for the analyzing power of the measurement. The other point at which model dependence is introduced is the light-quark subtraction step. A summary of the systematic errors in this analysis is presented at the end of this section in Tables 6.6, 6.7, 6.8, and 6.9.

6.3.1 Detector Modeling

Tracking Efficiency

The tracking efficiency error is estimated by varying the tracking efficiency in the Monte Carlo and estimating its effect on the analyzing power. Because the effect of tracking efficiency decouples from the other simulation issues, and because detailed studies of the tracking performance show that any unmodeled inefficiency has at most a very weak dependence on track $\cos\theta$ and momentum [149], the model has been to remove tracks completely at random from the Monte Carlo. It was found that the sensitivity of the measured value of A_b is

$$\frac{1}{A_b}\frac{\partial A_b}{\partial \epsilon_{inef}} \simeq -2.0, \tag{6.28}$$

where ϵ_{inef} is the residual unmodeled overall tracking inefficiency.

This unmodeled inefficiency may be estimated by comparing the data multiplicity distributions with those obtained from the Monte Carlo simulation. Figure 4.4 shows the raw multiplicity distribution for all hadronic events passing event selection criteria. The average multiplicity of selected tracks in data events passing hadronic event selection is 17.10, while the simulation reports 17.51. Figure 4.6 shows the distribution in polar angle of tracks in those events compared between data and Monte Carlo, and Figure 4.5 shows a comparison as a function of the natural logarithm of the total momentum.

The difference in the observed multiplicity between data and Monte Carlo can arise from two sources: 1) unmodeled tracking inefficiency, and 2) mis-tuning of the Monte Carlo generator so that it does not produce the genuine Z^0 decay charged multiplicity. Given a multiplicity measurement from ALEPH of $\langle n_{ch}\rangle = 20.85 \pm 0.24$ [150] and that the SLD Monte Carlo generator produces $\langle n_{ch}\rangle = 20.9$, and an overall multiplicity discrepancy between data and Monte Carlo of 0.4 tracks/ event out of 17.1, the unmodeled tracking inefficiency is estimated to be 2.3%. This may be easily corrected for after the fact, either by removing tracks from the Monte Carlo in a random fashion, or by applying an *ad hoc* correction to the answer after the analysis is complete. The former approach was chosen, and has been incorporated in the answer quoted in the previous section.

The systematic error incurred in this process is cautiously estimated to be 2% on the tracking efficiency, which translates into a 4% relative uncertainty on A_b.

Ghost Tracks

A feature of Figure 4.5 is that while the data has fewer tracks than the Monte Carlo for momenta up to 3 GeV, it has more tracks at high momentum. It is likely that this corresponds to an error in the modeling of the fragmentation and hadronization processes by JETSET, but the most conservative approach to understanding this as an error is to take all of the extra tracks to be randomly-signed background.

The "ghost track" hypothesis has a conceivable mechanism. High-momentum tracks in the cores of jets may rob hits from each other, and extra tracks may be formed out of the shorter fragments left over after the long tracks have been found. These in general will be quite straight, due to the projective nature of the CDC cells, the high momenta of the original parent tracks, and the probability of misassigning hits to form tracks.

The Monte Carlo has been conservatively adjusted in this analysis to add extra, randomly-signed tracks of the right momentum-distribution to flatten out the ratio of Figure 4.5. The end result of this test is that the measured value of A_b changed by a relative 1.0%**.

Momentum Resolution

The momentum resolution of the CDC, discussed in Section 4.2.3, is measured using dilepton events and through-going cosmic rays, and is found to be

$$\delta p_\perp = p_\perp^2 \sqrt{0.0050^2 + (0.010/p_\perp)^2}, \tag{6.29}$$

where $p_\perp$ is the momentum transverse to the beam axis in GeV. The effect of the momentum resolution on the analyzing power of the technique can be estimated from the Monte Carlo by calculating the analyzing power of Equation 6.3 with a generator-level Monte Carlo with a simple acceptance model and cuts. For the same events,

**The effect of extra tracks at high momentum increases with larger κ.

the momentum of the tracks is smeared by the amount specified in Equation 6.29, and the analyzing power recomputed. Taking the entire difference as a conservative estimate of the effect yields a relative systematic error of $< 0.2\%$.

Tag Purity

Section 6.2.5 dealt with issues of the B tag affecting the Monte Carlo estimation of its purity. To estimate the effect of mismodeling the purity, the analysis is re-run, forcing the contamination fraction to be different from what the Monte Carlo predicts by 1σ of the error. In the worst case, the all of the impurity is assumed to be $Z^0 \rightarrow c\bar{c}$ background, because these events have opposite asymmetry to $Z^0 \rightarrow b\bar{b}$ events. It is found that

$$\partial A_b^{meas} / \partial \Pi_c^{estimated} = 1.48, \tag{6.30}$$

and so the total systematic error from the tag composition is 2.4%. Contributions from *uds* contamination are smaller than the charm contribution by a factor of 10, and furthermore have the same sign asymmetry as the B asymmetry, and therefore do not contribute significantly.

The $Z^0 \rightarrow \tau^+\tau^-$ contamination was discussed above, and does not contribute more than $(0.04 \pm 0.02)\%$ of the tagged sample, and therefore its contribution to the asymmetry cannot be more than 0.04%, assuming randomly signed directions. Non-Z^0 events in the detector constitute a smaller fraction of the event sample than do the $Z^0 \rightarrow \tau^+\tau^-$, due to the difficulty of satisfying both the event selection and the impact-parameter tag.

A more serious contribution from background tracks arises from the fact that some of these background events may overlay beam crossings on which a real Z^0 decayed, even ones that are tagged. This is modeled by the background overlay in the Monte Carlo.

Geometrical Distortion of the CDC

The tracking chamber has been aligned using high-momentum tracks from $Z^0 \rightarrow \mu^+\mu^-$ and wide-angle Bhabhas. These provide a convenient source of monoenergetic

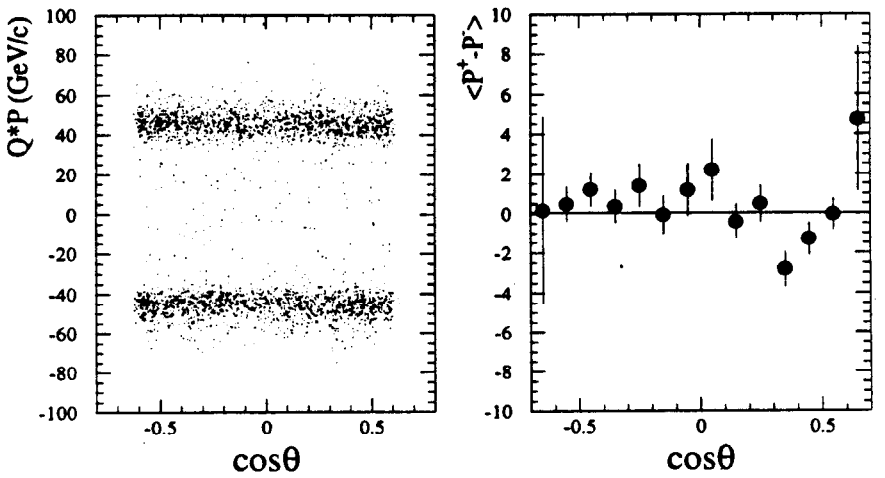

Figure 6.16: Total momenta of positive and negative muons separately as a function of $\cos\theta$. Negative muons appear with negative momenta in the plot on the left. The plot on the right shows the average difference between the measured total momentum of positive muons and negative muons as a function of polar angle.

tracks to test if there are any biases in the momentum of positive and negative tracks in the forward and backward hemispheres. Figure 6.16 shows the momentum of positive and negative leptons separately in di-lepton events as a function of $\cos\theta$, ruling out distortions which would bias the momentum of a 45 GeV track by more than 2%. Distortions produce constant offsets in the sagitta of tracks, and therefore affect lower-momentum tracks less than the dimuon sample.

The left-right forward-backward asymmetry is a particularly convenient observable from the point of view of this systematic error, in that the measured asymmetry is formed as a difference between the polarization states, and therefore, since the tracking chamber has the same geometrical distortions with the left-handed electron beam as with the right-handed beam, the distortions nearly cancel. The residual distortion effect is proportional to $A_e \simeq 0.15$, owing to the fact that more events are produced with the left-handed beam. This particular distortion is a ~6 times more serious problem for the unpolarized forward-backward asymmetry.

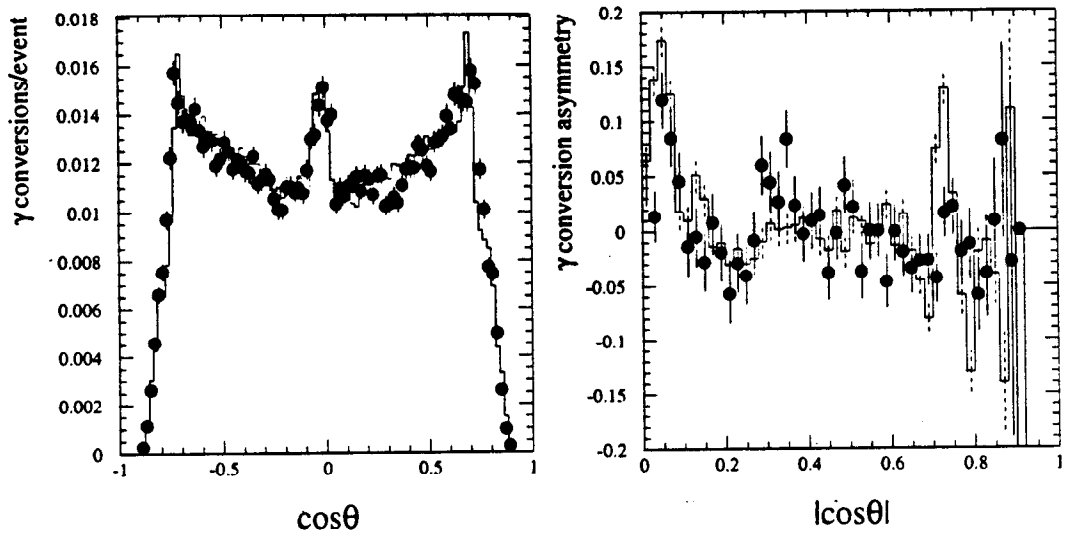

Figure 6.17: Data and Monte Carlo distributions of gamma conversions and their asymmetries.

Detector Material Asymmetry

Nuclear interactions of final-state particles with the material of the detector before the tracking volume introduce extra tracks into the detector, as well as degrading the momentum of the particles originating with the Z^0 decay. The positive charge of atomic nuclei lends the the extra tracks a net positive bias, and gives them a larger baryon fraction than is present in tracks originating at the Z^0 decay vertex. The extra tracks produced tend to have low momentum and are thus given lower weight in this analysis.

For the same reason that the geometrical distortion errors are suppressed by a factor of A_e, errors induced by asymmetry in the detector material distribution are also suppressed by the same amount.

Detector material asymmetry can be estimated by examining the rate of gamma conversions as a function of polar angle. Shown in Figure 6.17 is the gamma conversion rate on hadronic Z^0 decays passing the event selection compared between data and

Monte Carlo for the 1994–1995 run. The asymmetry

$$A_\gamma = \frac{n_\gamma(\cos\theta) - n_\gamma(-\cos\theta)}{n_\gamma(\cos\theta) + n_\gamma(-\cos\theta)} \tag{6.31}$$

is also computed with its statistical error and compared against the Monte Carlo. The significant rise in asymmetry around $\cos\theta \sim 0.05$ owes itself to the presence of a steel screw and a steel band around the VXD cryostat at the physical midplane of the detector. Because the IP is ~3.9 mm offset from the geometrical center of the detector, this band and screw are offset to one side. Fortunately, this material imbalance is in the central portion of the detector and contributes a vanishingly small amount to the asymmetry.

In order to quantify the detector material asymmetry's effect on an asymmetry measurement, a properly weighted average of it is necessary. Events at larger values of $|\cos\theta|$ contribute more to the fit, as per Equation 1.72. The statistical errors are magnified to reflect their contribution in the fit,

$$\delta A_\gamma \rightarrow \delta A_\gamma \left(\frac{1+\cos^2\theta}{2\cos\theta}\right) \tag{6.32}$$

and the asymmetries A_γ are averaged with their new errors within the range $|\cos\theta| < 0.8$, the tracking acceptance cut. The averages found are $\langle A_\gamma \rangle = -0.62\%$ for the data and $\langle A_\gamma \rangle = -0.91\%$ for the Monte Carlo. The discrepancy between these, multiplied by A_e, gives the justification for quoting this error at $< 0.1\%$.

Thrust Axis Resolution

The tracking chamber can be used to estimate the reliability of the Monte Carlo simulation of the thrust axis resolution. The angular resolution of the tracks in the CDC is 0.45 mrad in ϕ and 3.7 mrad in θ [151], much more precise than the thrust axis needs to be known. The technique is to sample events with calorimetric thrust axes in a particular bin of $\cos\theta$ and then to histogram the $\cos\theta$ of tracks in all such events. To the extent that JETSET properly models the angular distribution of tracks in Z^0 decays, these distributions of track angles can be compared directly between data and Monte Carlo.

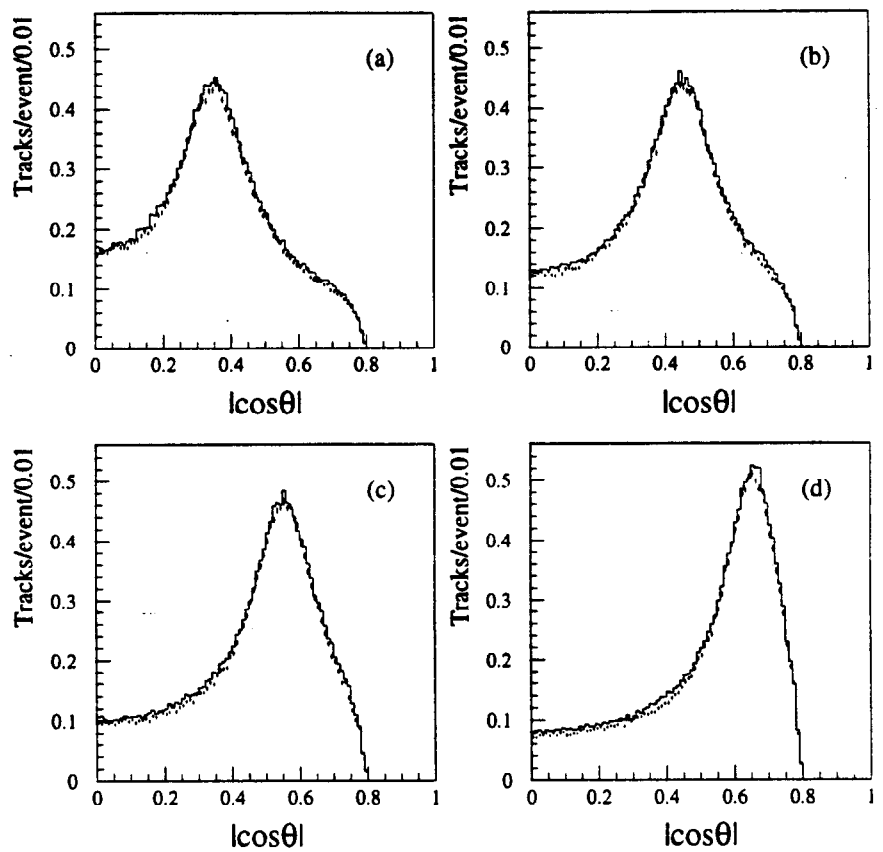

Figure 6.18: Comparison of data (points) and Monte Carlo (histogram) track $\cos\theta$, in bins of calorimeter thrust $\cos\theta_T$, showing that the calorimeter thrust axis direction is well modeled in the Monte Carlo. The $\cos\theta_T$ bins are: (a) $0.3 < |\cos\theta_T| < .4$, (b) $0.4 < |\cos\theta_T| < .5$, (c) $0.5 < |\cos\theta_T| < .6$, and (d) $0.6 < |\cos\theta_T| < .7$.

If the data has an unmodeled smearing of the thrust axis, or if the Monte Carlo smears the axis too much, the effect of that will appear in these distributions. The smearing must be sufficient to move an event from one region in $\cos\theta$ to another with a significantly different expected value of asymmetry as predicted by Equation 1.72. A comparison of these distributions, shown in Figure 6.18, puts an upper bound on the thrust axis bias at $\delta(\cos\theta) = 0.005$, which would bias the A_b answer by 0.6% relative to itself.

The momentum-weighted track charge in Equation 6.2 is insensitive to small angular smears of the thrust axis. Changes to the dot product of the momentum into the thrust axis are second order in the smearing angle. The effect on the transverse momentum of particles with respect to the thrust axis is much larger, although not important for this analysis.

Event Pileup

A small, known deficiency of the Monte Carlo is that it only generates one hadronic Z^0 decay per event, while each beam crossing at SLC has a finite probability of producing two Z^0 decays on one beam crossing. Because SLC has a higher luminosity than LEP per beam crossing, it has a larger fraction of pileup events. Assuming 150,000 hadronic Z^0 decays are collected at an average running luminosity of 50 decays/hour with SLC running at 120 Hz, the pileup fraction should be ~1/8640, yielding a total of 17.3 pileup events. After correcting for event selection efficiency and the tagging fraction, ~4.7 events are expected to be pileup events. Of a total tagged sample of 12002 events, the pileup fraction amounts to 0.04%. If the pileup events are assumed to be randomly signed, then the systematic error on A_b is also 0.04%. In order to tag, though, a pileup trigger has to contain at least one $Z^0 \rightarrow b\bar{b}$, so the effect is very likely smaller.

Final-State QCD radiation

The asymmetry-diluting effects of final-state QCD radiation are incorporated into the JETSET Monte Carlo through its parton-shower model. The magnitude of the difference between the raw asymmetry and the QCD corrected asymmetry can be

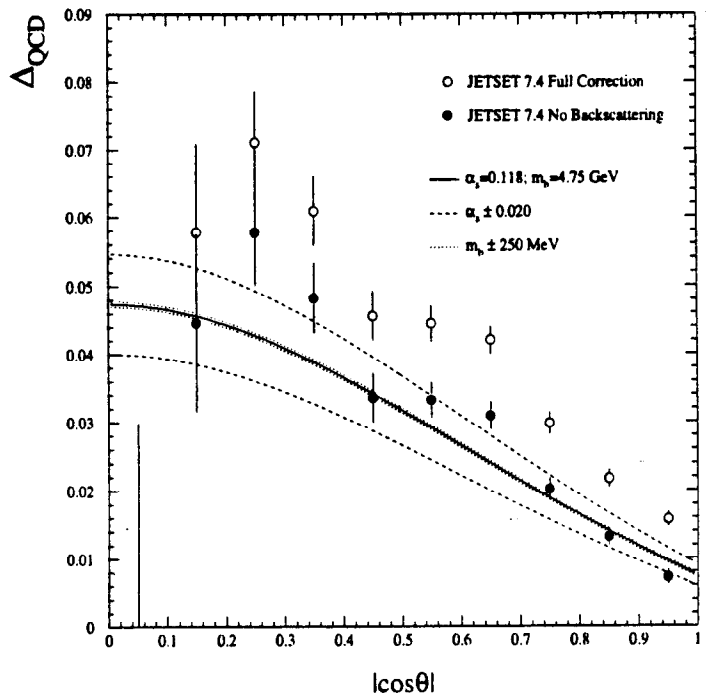

Figure 6.19: QCD corrections as calculated in [58], compared against those estimated from JETSET 7.4. Errors on the curves include $\pm 2\sigma$ of the theoretical error of α_s and ± 250 MeV on the b quark mass. The open circles are the full correction as estimated by the JETSET generator, and the filled circles are the correction omitting events in which the two quarks are in the same hemisphere. This second form will become important in Section 7.3.6. The difference between JETSET and the analytic calculation gives a -1% relative correction to A_b.

calculated using JETSET by comparing the asymmetry using the quark axis before the initiation of the parton shower and the asymmetry using the quark axis after the parton shower has reached its cutoff. The former asymmetry is simply the raw electroweak value given in Equation 1.72 as a function of $\cos\theta$. This smear in the quark axis angle dilutes the asymmetry and constitutes a high-order calculation of the QCD correction, which may be compared against first- and second-order analytic calculations. This comparison of the fractional change in asymmetry using the Monte Carlo estimate and the calculation in Reference [58] is shown in Figure 6.19.

Table 6.3: Systematic uncertainties on the electron beam polarization as measured by the Compton Polarimeter [42]. The later 2/3 of the 1993 running benefited from routine laser polarization scanning and has smaller errors.

Systematic Uncertainty	End 1993 $\delta P_e/P_e$ (%)	Total 1993 $\delta P_e/P_e$ (%)	1994–1995 $\delta P_e/P_e$ (%)
Laser Polarization	0.6	1.0	0.2
Detector Linearity	0.6	0.6	0.5
Electronic Crosstalk	0.2	0.2	0.2
Analyzing Power Calibration	0.4	0.4	0.3
Cross Checks	0.5	0.5	0.4
Polarimeter Total	1.1	1.3	0.76
Final Focus Chromaticity	1.1	1.1	0.2
Total	1.6	1.7	0.78

It is apparent from Figure 6.19 that JETSET estimates a larger QCD correction than the analytic calculation. Because the analytic version is used in Chapter 7, consistency requires a commensurate Δ_{QCD} to be used in this result. The values of the estimate Monte Carlo asymmetry in Table 6.2 have been increased by a relative 1%, which lowers the measured value of A_b by 1%.

The systematic error estimated from this contribution is given by allowing the value of α_s to vary by 2σ of its current theoretical ambiguity, as well as comparing a second-order calculation [54] against the first-order version [55]. The second-order calculation was not used owing to the fact that it neglected the b quark mass, did not give a dependence on $\cos\theta$, and was calculated assuming the b quark direction was measured, instead of the thrust axis. It has been estimated that using the thrust axis instead of the b quark axis reduces the QCD correction to 90% of its value [152], but another calculation [57] quotes a 95% correction, and this discrepancy is also accounted in the systematic error.

Polarization

The systematic error due to the measurement error of the electron beam polarization is one of the smallest errors due to the effort involved in producing the required precision for the A_{LR} measurement. The Compton polarimeter measures a raw scattering asymmetry, which is then divided by the laser polarization and an expected asymmetry function which depends on a QED prediction and a detector model. The raw Compton asymmetry is affected by detector/ADC linearity and interchannel crosstalk. The raw asymmetry also involves subtracting the laser-off background from the observed Compton signal. If there is crosstalk from the laser electronics over to the detector amplifiers and digitizers which contributes to the laser-on signal but not to the measured background, it will affect the measured asymmetry. Fortunately, this electrical pickup can be measured when the SLC electron beam is off.

The laser polarization is monitored by scanning the voltages on the Pockels Cells to determine the phase shift of the transport optics down to the Compton interaction point, and to determine the unpolarized fraction, which dominates the uncertainty in laser polarization. This scanning of Pockels Cell voltages was not installed until about 1/3 of the way through the 1993 run, increasing the laser polarization error for the 1993 result.

An additional error in the polarization used arises from the fact that the Compton polarimeter measures the average polarization of the entire bunch of electrons, while only a portion of the bunch is focused tightly enough to contribute to the luminosity. If the electron bunch has a large energy spread, or worse, a long energy tail, then the off-energy electrons in the bunch will not arrive at the SLC IP properly focused, owing to the chromaticity of the final focus. The energy of the electrons is correlated with the orientation of their polarization, from Equation 3.2. Energy spread in the bunch depolarizes the bunch, but a chromatic final focus will pick out a more coherently polarized portion of the bunch. This effect has been estimated for 1993 running parameters to be a $(1.7\pm1.1)\%$ correction to the luminosity-weighted polarization [41]. For 1994–1995 running, the energy spread of the beam was carefully controlled by "overcompressing" the bunch in the NRTL transfer line, and by upgrading the optics of the final focus. For 1994–1995, the chromatic effect is estimated to be $0.2 \pm 0.2\%$, and it is incorporated in both the polarization values and errors for both runs.

Beam Parameter Asymmetries

A potential source of error for an asymmetry measurement is the difference in the average absolute value of the polarization on the left-handed beam pulses as compared to the right-handed beam pulses. If we follow Equation 1.61 but set $P_{e,Right} = |P| + \epsilon_p$, and $P_{e,Left} = -|P| + \epsilon_p$, where $|P|$ is the average magnitude of the polarization of both beams, then the left-right forward-backward asymmetry of Equation 1.72 becomes

$$\tilde{A} = \frac{2A_b|P|\cos\theta}{(1+\cos^2\theta)(1-A_e\epsilon_p)}. \tag{6.33}$$

The Compton polarimeter is able to measure the polarization of both helicity states of the beam separately, and is measured to be $\Delta P_e/P_e = 0.0033 \pm 0.0001$ [153] and is smaller in 1994–1995 [42]. The effect on the measured A_b is a relative 0.05%.

A related systematic error contribution is the difference in average luminosity between the left-handed beam and the right-handed beam[††]. This asymmetry can be measured with the electron beam toroids and corrected after the run. During the 1993 run, the NLTR spin rotator solenoid was reversed for approximately half of the accumulated luminosity, nearly canceling this asymmetry; The net current asymmetry for 1993 was estimated to be $(0.038 \pm 0.050)\%$ [153]. For 1994–1995, the spin rotator reversals were arranged less fortuitously, and the average luminosity asymmetry became $(0.087 \pm 0.043)\%$ [42]. If $\mathcal{L}_R = \overline{L}(1+\epsilon_{\mathcal{L}})$ and $\mathcal{L}_L = \overline{L}(1-\epsilon_{\mathcal{L}})$, the expected asymmetry function becomes

$$\tilde{A} = \frac{2A_b|P_e|\cos\theta}{(1+\cos^2\theta)(1-(1+|P_e|)A_e\epsilon_{\mathcal{L}})}. \tag{6.34}$$

This effect, too, is multiplied by a factor of A_e, but has an additional $(1+|P_e|)$. The total error incurred from neglecting this effect is 0.03%.

[††]While the polarized SLC is constructed to cancel most effects that could generate such an asymmetry, effects at the polarized electron source can remain. In particular, misalignment or circular dichroism in the source optics can introduce a difference in the amount of light reaching the cathode for the two photon helicities.

6.3.2 Modeling Physical Processes

Weighting Scheme

The task of evaluating the sensitivity of an analysis that is sensitive to the details of B hadron fragmentation and decay using a Monte Carlo model is a large one. The technique used here is to generate a large sample of JETSET 7.4 $Z^0 \rightarrow b\bar{b}$ decays and to calculate the analyzing power. No detector simulation is performed, because systematic effects from the underlying physics model and detector-induced effects are expected to be independent multiplicative factors in the analysis.

The strategy employed is to evaluate the decay axis from the original quark directions given by JETSET 7.4, calculate the momentum-weighted charge sum for the event using observable final-state particles (after decays of particles, including the K_s^0 and the Λ. Then, to calculate the error coming from contribution j, the sums of correct and incorrect events, with weights to be described below, are formed:

$$N^j_{right} = \sum_{CorrectEvents} \left(1 + \epsilon^j_i\right), \tag{6.35}$$

where i is the subscript of correct events, and ϵ^j_i is the weight on that event for systematic error j. Similarly, the incorrect sum is

$$N^j_{wrong} = \sum_{InorrectEvents} \left(1 + \epsilon^j_i\right). \tag{6.36}$$

The weighted analyzing power is given by

$$AP^j = \frac{N^j_{right} - N^j_{wrong}}{N^j_{right} + N^j_{wrong}}, \tag{6.37}$$

and compared against the analyzing power computed for the same generated sample with $\epsilon = 0$ on each event. The fractional change in analyzing power is the fractional error on the measurement of A_b, corresponding to a fluctuation in a model parameter described by the weights ϵ^j_i. There is no need to normalize the weights in this scheme because of the the cancelation of normalization factors in the numerator and denominator of Equation 6.37. Some of the errors mentioned below will use special estimations not incorporating the weighting scheme.

Table 6.4: Generator-level analyzing powers for events with different numbers of fragmentation protons. The errors are statistical errors on this Monte Carlo study.

# Fragmentation Protons	Event Fraction	Analyzing Power
0	0.534 ± 0.001	0.4767 ± 0.0027
1	0.237 ± 0.001	0.4339 ± 0.0041
2	0.159 ± 0.001	0.4371 ± 0.00050
3	0.046 ± 0.0005	0.4037 ± 0.0095
4	0.0178 ± 0.0003	0.414 ± 0.015
5	0.0039 ± 0.0001	0.374 ± 0.033
≥ 6	0.0014 ± 0.0001	0.465 ± 0.054

B Fragmentation and Hadronization

The first systematic error to test is the fragmentation function, which will use special Monte Carlo generations, as the fragmentation function affects the momentum and distribution of all particles in the event. If a choice were made to weight the events with a function of the B hadron momentum, then the sample may be biased towards events with hard gluon radiation, rather than the details of string breaking, so the weighting procedure was not chosen.

The analyzing power of the momentum-weighted track charge technique was calculated with the Peterson fragmentation function [118] with $\epsilon_b = 0.006$, yielding an average $x_e = E(B)/E(beam) = 0.695$. The Peterson parameter ϵ_b was varied between 0.01 and 0.002 to estimate this systematic error. Also investigated was the use of the Bowler fragmentation function [154], tuned to have the same mean B hadron energy as the default Peterson function, and the discrepancy in analyzing power is given as a separate error.

The uncertainty in the production fractions of B hadron species contributes a systematic error because the different species have different analyzing powers. The B^0 and B^+ fractions are constrained to be equal by isospin symmetry, but the B_s and Λ_b fractions need to be measured experimentally [155][156][157].

Table 6.5: Generator-level analyzing powers for events with different numbers of fragmentation $K^{\pm}$. The errors are statistical errors on this Monte Carlo study.

# Fragmentation $K^{\pm}$	Event Fraction	Analyzing Power
0	0.382 ± 0.001	0.4873 ± 0.0032
1	0.277 ± 0.001	0.4541 ± 0.0038
2	0.189 ± 0.001	0.4444 ± 0.00046
3	0.0884 ± 0.0006	0.4072 ± 0.0069
4	0.0399 ± 0.0004	0.3942 ± 0.010
5	0.0148 ± 0.0003	0.3848 ± 0.016
≥ 6	0.0086 ± 0.0002	0.3617 ± 0.023

Another detail of fragmentation is the fraction of protons and other baryons produced by the hadronization process. Because protons are much more massive than the other light particles which contribute to the momentum-weighted charge sum, they can substantially affect the analyzing power. A Monte Carlo run consisting of only $Z^0 \rightarrow b\bar{b}$ was performed, and the analyzing power computed separately for events with different numbers of fragmentation protons present. The results of this study are presented in Table 6.4. The SLD Monte Carlo generates 1.053 protons/event [36], while the PDG value is 0.92±0.11 [146]. This does not constrain the proton production in $Z^0 \rightarrow b\bar{b}$ events, though, which the Monte Carlo predicts at 0.78 protons/event, and so the uncertainty is doubled to be conservative. If the sample of events with fragmentation protons was reduced by 20% (absolute) and replaced with events with no fragmentation protons in them, the analyzing power would change by a relative 2.4%.

The multiplicity of fragmentation $K^{\pm}$ was treated similarly, and this result is displayed in Table 6.5. The 1994 PDG reports an inclusive 2.12±0.13 $K^{\pm}$ event, while the SLD Monte Carlo predicts 2.28 inclusive kaons in all hadronic Z^0 decays, including the decay products of heavy hadrons. The SLD Monte Carlo predicts 1.2 fragmentation kaons per event in $Z^0 \rightarrow b\bar{b}$ decays. If a conservative 20% of all events were replaced with events without fragmentation kaons, then the analyzing power

Table 6.6: Summary of the detector modeling and general systematics of the binned asymmetry fit to A_b.

Error Source	Variation	$\delta A_b/A_b$
Tracking		
Tracking efficiency	2.0%	4.0%
Ghost Tracks	3% at high momentum	1.0%
Momentum Resolution	100% of effect	< 0.2%
Thrust Axis Resolution		0.6%
Chamber Distortion		< 0.3%
Material Asymmetry		< 0.1%
Tag Contamination		
$Z^0 \to c\bar{c}$ Contribution to Tag	See Table 6.1	2.6%
$Z^0 \to uds$ Contribution to Tag	See Table 6.1	0.3%
$Z^0 \to \tau^+\tau^-$ Contribution to Tag	Full Value	< 0.04%
General		
Monte Carlo Statistics	1σ	1.6%
QCD Radiation	$\alpha_s \pm 0.02$, 2nd order terms	0.9%
Polarization	1σ	0.8%
Event Pileup	$(0.0 \pm 0.26)\%$	< 0.04%
Subtotal: Detector Modeling and General		5.3%

Table 6.7: Summary of the B hadron fragmentation systematic errors of the binned asymmetry fit to A_b.

Error Source	Variation	$\delta A_b/A_b$
B Fragmentation $\langle x_B \rangle$	$\langle x_B \rangle = 0.695 \pm 0.021$	1.3%
B Fragmentation Function	Bowler-Peterson, same $\langle x_e \rangle$	0.5%
Fragmentation Protons	$(0.78 \pm 0.16)\%$	2.4%
Fragmentation $K^{\pm}$	$(1.20 \pm 0.24)\%$	2.5%
$b \rightarrow B^0$ Fraction	$(40.6 \pm 2.0)\%$	0.39%
$b \rightarrow B^+$ Fraction	$(40.6 \pm 2.0)\%$	0.80%
$b \rightarrow B_s$ Fraction	$(11.5 \pm 2.0)\%$	0.63%
$b \rightarrow \Lambda_b$ Fraction	$(7.3 \pm 3.6)\%$	0.58%
gluon $\rightarrow b\bar{b}$	$\pm 50\%$ of JETSET	0.02%
gluon $\rightarrow c\bar{c}$	$\pm 50\%$ of JETSET	0.07%
Subtotal: B Fragmentation		3.9%

would change by a relative 2.5%.

The inclusive pion yield in the SLD Monte Carlo matches the 1994 PDG value to within 0.4%, and the error in the PDG average is 2%, so fragmentation pions are not expected to be a significant source of systematic error. The inclusive non-leading multiplicity has also been measured by SLD [158], and found to be in agreement with the SLD Monte Carlo model.

$B^0 - \overline{B}^0$ Mixing

The systematic error from uncertainties in the species-averaged time-integrated mixing parameter χ_B have been evaluated by disabling the mixing in the Monte Carlo, and checking the difference in analyzing power between that model and the Monte Carlo with a full mixing value of $\chi_B = 0.130$ applied. The total effect on the analyzing power is a relative 11%, and the fractional uncertainty in χ_B is proportional to the

Table 6.8: Summary of the B hadron mixing and decay systematic errors of the binned asymmetry fit to A_b.

Error Source	Variation	$\delta A_b/A_b$
B Mixing	$\chi_B = 0.115 \pm 0.006$	0.6%
τ_{B^+}/τ_{B^0} Lifetime Ratio	1.00±0.20	0.22%
D^0 fraction in B decay	$(64.8 \pm 2.6)\%$	0.24%
$D^\pm$ fraction in B decay	$(26.6 \pm 3.7)\%$	0.20%
D_s fraction in B decay	$(10.7 \pm 2.5)\%$	0.9%
$B \rightarrow D$ Momentum	$\langle P_D \rangle = (2.50 \pm 0.13)$ GeV/c	0.10%
$B^+ \rightarrow D$ *vs* $B^0 \rightarrow D$ Momentum	±20%	3.7%
B Decay Multiplicity	11.04 ± 0.25	0.41%
$B \rightarrow K^\pm$ Multiplicity	$1.49 \pm .06$	0.22%
$B \rightarrow P$ Multiplicity	$0.13 \pm .02$	0.09%
$B \rightarrow \pi^\pm$ Multiplicity	8.40 ± 0.25	0.32%
$B \rightarrow K^\pm$ Momentum	4×hard tail	0.62%
$B \rightarrow P$ Momentum	4×hard tail	0.10%
$B \rightarrow \pi^\pm$ Momentum	4×hard tail	3.0%
$B \rightarrow l\nu X$ B.R. Fraction	10.96 ± 0.55	0.46%
$B \rightarrow D^*$ Fraction	$(62 \pm 12)\%$	0.32%
Λ_b Polarization	100% of expectation	0.8%
Subtotal: B Mixing and Decay		5.1%

Table 6.9: Summary of the charmed hadron modeling systematic errors of of the binned asymmetry fit to A_b.

Error Source	Variation	$\delta A_b/A_b$
Charm Fragmentation		
Fragmentation $\langle x_D^* \rangle$	$\langle x_D^* \rangle = 0.498 \pm 0.023$	0.4%
$c \rightarrow D^0$ Fraction	$(53 \pm 3)\%$	0.07%
$c \rightarrow D^\pm$ Fraction	$(25 \pm 5)\%$	0.15%
$c \rightarrow D_s$ Fraction	$(22 \pm 6)\%$	0.11%
Charmed Hadron Decay		
Charm Decay Multiplicity	each$\pm$ 2.2%	0.06 %
$D \rightarrow l\nu X$ B.R. Fraction	each$\pm$ 5% (rel.)	< .1%
Subtotal: Charm Modeling		0.46%

fractional uncertainty in A_b, supplying the systematic error. A correction must be applied because the latest measurement of the mixing parameter $\chi_B = 0.115 \pm 0.006$ [64]. rather than the older value used in the Monte Carlo. This amounts to a downwards correction to A_b of $\simeq$1% .

An important feature is that the mixing dependence of A_b when measured with momentum-weighted track charge is less than similar analyses using semileptonic B decays and/or kaons. The reason for this is that the B^0 and the B_s have intrinsically smaller analyzing powers to begin with, so the dilution of the information coming from their decays matters less in the overall sum.

B Meson Decay Model

The most important sources of model dependence due to the particular choice of the B hadron decay model are described below. Allowed variations in the model parameters are guided by discrepancies between the SLD Monte Carlo and observed data, as mentioned in Chapter 5, and also by the uncertainties in the available measurements.

Differences in the $B^{\pm}$ and B^0 D Spectrum

The inclusive particle spectra of Figure 5.2 provide no information about the charge of the particles, nor about whether they came from $B^{\pm}$ or B^0 decay. The D spectra of Figure 5.3 also have no indication of what the individual spectra of $B^{\pm}$ and B^0 D momentum spectra might be. An error associated with this uncertainty was evaluated by introducing a weight to the $B^{\pm} \rightarrow D$ momentum spectrum and an opposite weight the $B^0 \rightarrow D$ spectrum, so that the overall mean would be conserved. The weights are chosen in inverse proportion to the branching fractions, so as to keep the mean D momentum constant.

Hadronic Decays

One of the main discrepancies between the SLD Monte Carlo and the ARGUS data is in the high-momentum end of the inclusive pion spectrum. We weight events with $\epsilon = 1$ for events with B-decay pions above 2.0 GeV and report the relative difference in analyzing power as a systematic error. Other errors include varying the average B decay multiplicity, the charm momentum spectrum, the fractions of D^0, D^+, and D_s in B hadron decay, as well as the charm decay multiplicity. Errors were also evaluated for the inclusive fractions of kaons, pions, and protons from B decay, as well as their momentum spectra, although these errors may overcount somewhat the charm fractions and spectra errors.

Semileptonic Decays

While semileptonic decays constitute only ~11% of the decays of B hadrons, they are an important portion of the sample. The charged lepton has a hard momentum spectrum in the laboratory frame, and it is very correlated with the charge of the b quark emitted by the Z^0 [‡‡]. Leptons from cascade charm decays are anticorrelated with the b sign, but have less momentum than the prompt B decay leptons.

[‡‡]It is not perfectly correlated, because of $B^0 - \overline{B}^0$ mixing.

Charm Modeling

The lifetimes, decay properties, and production momentum spectra of D mesons have already been included in the estimation of the error on the purity of the B tag, but these uncertainties also affect the estimation of how often the correct sign of the decay axis is determined by the momentum-weighted charge in $Z^0 \rightarrow c\bar{c}$ events. These errors include uncertainties in the species fractions, their multiplicities, and their momentum spectra. Uncertainties in their lifetimes do not enter here, as they are decoupled from the momentum-weighted charge measurements, except to the extent that they alter the composition of the tagged sample.

τ_{B^+}/τ_{B^0} Lifetime Ratio

A difference in the B^+ and B^0 lifetimes would have an effect on the analyzing power of the technique, owing to the different analyzing powers of hemispheres containing B^+ and B^0, and the fact that the tag preferentially selects events containing long-lived B hadrons. The magnitude of this effect is diluted somewhat by the fact that there are two B hadrons in each event, each with its chance of contributing enough tracks to tag the event. The SLD Monte Carlo sets the B^0 and B^+ lifetimes equal to each other, consistent with the latest measurements of τ_{B^+}/τ_{B^0} from LEP and the Tevatron [159] of 1.01 ± 0.05.

To investigate this, Monte Carlo events are generated with an artificially modified $\tau_{B^+}/\tau_{B^0}=1.2$, and the tag and geometrical acceptance are simulated at the generator level. The analyzing power is then computed and compared against generator-level events with equal lifetimes, and the difference between the ratio of the analyzing powers and unity, scaled by the true uncertainty in the lifetime ratio, constitutes the systematic error.

Final-State Polarization

The average final-state polarization of b quarks emerging from the hard scattering process is A_b, which in the Standard Model is expected to be close to 94%. If this polarization is transmitted to the final-state hadrons, it has the ability to shift the

momentum-weighted charge distributions and affect the analyzing power of the technique presented in this chapter.

A recent paper by Falk and Peskin [160] discusses the preservation of polarization of final-state hadrons from Z^0 decay. In it, they prove a "no-win" theorem, in which it is shown that for the case of $b \rightarrow$pseudoscalar meson, polarization information is lost. The meson itself is unpolarizable, but the argument of Falk and Peskin shows that even the polarization of a B^* cannot affect the final-state distribution of particles, because the angular distribution of the transition photon emitted in $B^* \rightarrow B$ has an isotropic distribution. Even transition pions from more highly excited mesons, B_1, B_2^* are expected to have no forward-backwards asymmetry along the direction of helicity of the excited mesons.

Heavy baryons, on the other hand, have the ability to retain their polarization. Because the light diquark in a Λ_b is in a $j = 0$ state, it has no angular momentum to impart to the heavy quark. This argument has been used to show that fragmentation does not dilute Λ_b polarization when the Λ_b is produced directly [161][162]. Falk and Peskin, however, add in 30% Σ_b and Σ_b^*, which have less expected polarization. and arrive at a net polarization of the Λ_b to be 68%. A recent measurement from ALEPH quotes the Λ_b polarization, measured with the energies of the lepton and neutrino in semileptonic Λ_b decays, to be -0.26 ± 0.26 [164], consistent with the high fraction ($\sim$50% of the b baryon production) of Σ_b and Σ_b^* production measured by DELPHI [140].

The polarization of the Λ_b has an effect on the present analysis because polarized Λ_b's are expected to have a forward-backward asymmetry of Λ's as decay products in their rest frame. Körner and Krämer have also calculated a final-state asymmetry in semileptonic decays of polarized Λ_b's [163][161][162]. It is expected that the manifestation of polarization in a general hadronic decay of the Λ_b will be diluted even more than in the semileptonic case.

The expected BR($b \rightarrow \Lambda_b$) is $\sim$7% [156][157], and so $\sim$14% of $Z^0 \rightarrow b\bar{b}$ decays have a Λ_b in them. The average momentum-weighted charge for the Λ_b is estimated to be one-half that of the average for the B mesons. Given that an event with a Λ_b is likely to have another hadron in the other hemisphere, even if the sign of

the Λ_b is determined only by its unmodeled polarization, the other hemisphere is likely to cancel the information. A conservative estimate of this systematic error is (14%)(0.23)(0.50)(0.50)=0.8% (relative), taking into account the branching fraction, expected polarization, polarization information dilution in hadronic Λ_b decays, and charge dilution of B baryons relative to the meson in the opposite hemisphere.

6.3.3 Monte Carlo Statistics

The finite sample of Monte Carlo available for this analysis incurs an error on the measurement. While it is statistical in nature, this error is best classified as a systematic error because it enters through the modeling necessary to extract A_b from the data.

The Monte Carlo statistical error can best be evaluated by adding the MC statistical errors to the data statistical errors in quadrature before performing the fit of Equation 6.22. Subtracting off in quadrature the statistical error in the fit from the data errors alone yields the Monte Carlo statistical error, estimated to be a relative 1.64%.

6.4 Cross-Checks

Among the most serious errors above are the B fragmentation and decay modeling, and the light-quark subtraction. While the momentum-weighting exponent κ and the parameters of the B tag have been chosen to minimize the measurement error, it is a useful cross-check to vary these parameters of the analysis to see if any dependence of the answer appears.

6.4.1 Kappa dependence

At a fixed, very pure tag, the check of κ-dependence of the answer is a sensitive test of the validity of the fragmentation and decay model. For $\kappa \sim 0$, the technique simply counts the positively and negatively charged tracks in each hemisphere, subtracts them, and assigns the b quark direction to point along the direction with the largest

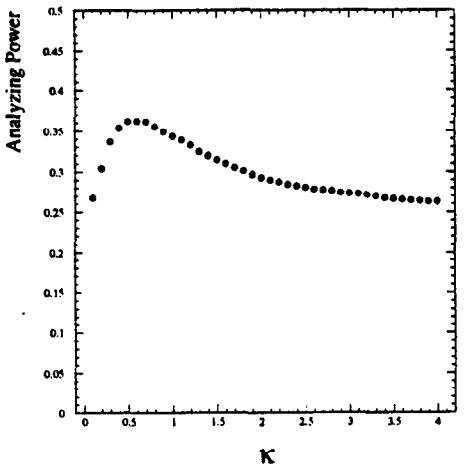

Figure 6.20: Analyzing power AP in fully simulated Monte Carlo as a function of the momentum-weighting exponent κ.

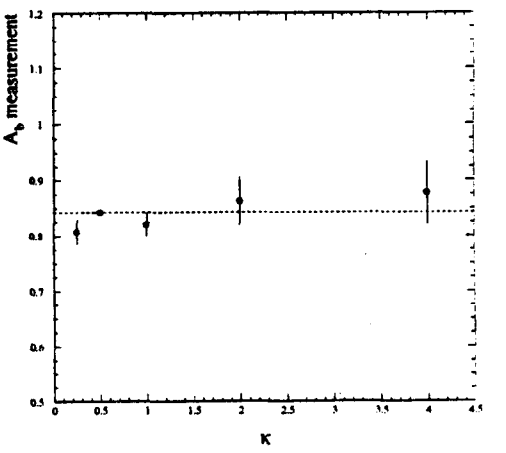

Figure 6.21: Dependence of the value of A_b measured with the binned asymmetry fit on the momentum-weighting exponent κ. Correlated statistical and systematic errors have been removed, taking $\kappa = 0.5$ as a reference point.

count of negative tracks. In the limit as $\kappa \rightarrow \infty$, the momentum-weighted charge sum in 6.2 is dominated by the single most energetic track in the event. Because of the relatively low momentum of fragmentation tracks and the stiff fragmentation function of the B mesons, the low-κ limit probes the hadronization model, while the high-κ limit probes the details of B decay.

The Monte Carlo expectation of the κ-dependence of the analyzing power, defined in Equation 6.3, is shown in Figure 6.20, demonstrating that the different processes active in B production and decay have different effects on the analyzing power.

Experiments at the Z^0 are uniquely qualified at this point in time to study the charge-momentum correlations in B-decay, owing to the clean separation of the decay products of the two B hadrons. Experiments in which a $\Upsilon(4S)$ is produced at rest for the most part confuse the decay products of the two B hadrons and therefore cannot do any charge-dependent correlations. Some progress has been made in that realm with double-tagged semileptonic decays as well as with fully reconstructed B decays.

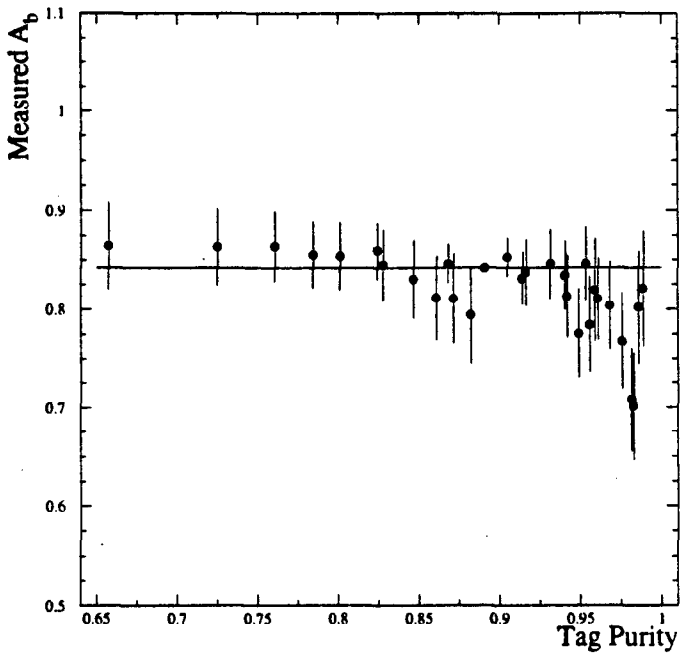

Figure 6.22: Tag dependence of the binned asymmetry A_b measurement. The weakest tag is 2 tracks at 2σ, while the strongest tag is 4 tracks at 9σ. Correlated statistical and systematic errors have been removed, taking the 3 tracks at 3σ point (with horizontal line) as a reference.

but that information cannot be used in an inclusive analysis such as this one.

The κ-dependence of the measured A_b is shown in Figure 6.21. The flatness of this graph can in fact be used to constrain some of the details of the B-decay model in the Monte Carlo.

6.4.2 Tag dependence

Another important cross-check is to repeat the analysis at a fixed κ but to vary the tag parameters. Because the asymmetry of the tag contamination is subtracted off using a Monte Carlo model, and because the background asymmetry has opposite sign from the signal asymmetry, this is a sensitive test of the ability of the Monte

Carlo to simulate the background properly.

Also tested is the tag bias on the analyzing power. The tag is more efficient for events with many high-energy charged tracks in them, as the errors in the tracks' impact parameters are smaller and the tag becomes easier to satisfy. Events with large amounts of visible energy in charged tracks are expected to have more analyzing power than those whose distributions fluctuated more towards neutral energy. The tag efficiency depends most strongly, however, on the decay times of the B hadrons, though, and the analyzing power depends only very weakly on those decay times, and that dependence comes from time-dependent mixing, and the mixing systematic error is small.

6.4.3 Hemisphere consistency

A feature of $Z^0 \to b\bar{b}$ decays is that there are two b-type quarks in the final state; each event effectively has two chances to get the proper sign. More importantly, though, a comparison of the consistency between the signing of the two quarks using momentum-weighted track charge can be used to determine how often the signing procedure yields the correct answer. The technique is to form the hemisphere momentum-weighted charges and see if they have the same sign or different sign. If both hemispheres' charges are signed correctly, then they should have oppositely signed charges. The relevant quantity to form then is

$$H = P_{agree} - P_{disagree} \tag{6.38}$$

where P_{agree} is the fraction of tagged events with hemispheres of opposite charge, and $P_{disagree}$ is the fraction of events with the same sign charge. The hemisphere analyzing power AP_{hem} is then given by

$$AP_{hem} = \sqrt{H}, \tag{6.39}$$

and can be checked for consistency between data and Monte Carlo. This variable is not quite the analyzing power for an analysis using only hemisphere charges owing to additional correlations between the two hemispheres, but it is a useful cross-check on the modeling of the Monte Carlo. It is the separate information from the hemisphere charges that allows the self-calibrated analysis of the next chapter to be performed.

Table 6.10: Asymmetries in the consistent-inconsistent hemisphere fractions, as defined in Equation 6.38 for tagged data and MC at different values of κ. Errors are statistical. At low values of κ, hemisphere correlations become more important, enlarging the fraction of events with agreeing hemispheres without increasing the analyzing power.

κ	Data H	Monte Carlo H
0.25	$(12.66 \pm 0.92)\%$	$(13.44 \pm 0.52)\%$
0.50	$(10.06 \pm 0.92)\%$	$(9.28 \pm 0.52)\%$
1.00	$(6.65 \pm 0.92)\%$	$(7.15 \pm 0.52)\%$
2.00	$(4.87 \pm 0.92)\%$	$(5.27 \pm 0.52)\%$
4.00	$(4.70 \pm 0.92)\%$	$(5.05 \pm 0.52)\%$

The results of the comparison between data and Monte Carlo are summarized below for events passing the 2-D normalized impact parameter tag, and at several different values of κ.

6.5 Summary

This chapter has presented a binned-asymmetry fit for A_b using the polarized forward-backward asymmetry of lifetime-tagged $Z^0 \rightarrow b\bar{b}$ events signed with momentum-weighted track charge. The calibration of the tag composition, correct-sign probability, and radiative effects have been estimated with the SLD Monte Carlo. The resulting A_b is found to be

$$A_b = 0.828 \pm 0.054(\text{stat.}) \pm 0.070(\text{syst.}), \tag{6.40}$$

with the systematic error dominated by uncertainties in the details of B fragmentation and decay, as well as modeling the tracking efficiency. The next chapter presents a technique designed to overcome these modeling errors by reducing the dependence on the Monte Carlo for calibration.

Chapter 7

A_b with Momentum-Weighted Charge: Maximum Likelihood

An improvement to the technique of the previous chapter is to take advantage of the value of Q, defined in Equation 6.2, on each event. If $|Q|$ is large, the probability of assigning the charge correctly is near unity, while very little information about the sign is given for $|Q|$ near zero. This leads us to incorporate this information in a maximum-likelihood analysis, which is able to make optimal use of the quantities measured in the data.

A more important feature of the analysis presented in this chapter is that the effectiveness of the momentum-weighted charge technique may be calibrated by taking advantage of the momentum-weighted charge separately in the two hemispheres of each event. This procedure is a natural extension of the hemisphere consistency cross-check of Section 6.4.3. It reduces the model dependence of the measurement of A_b, which, as indicated in Chapter 6, would ultimately limit the measurement.

This chapter describes maximum likelihood techniques in general, the specific likelihood function used in this analysis, and the calibration of its input parameters. It then describes the extraction of A_b, the remaining model dependencies, and cross-checks that have been performed.

7.1 General Formulation

The technique of maximum likelihood is described in many standard texts on statistics [165][166], so only an outline of its features necessary for this analysis will be presented. Briefly put, the technique asks the question: "What is the most probable value of the parameters of the model given the data observed, and given no other *a priori* knowledge of the measurement?" The set of parameters defining a model to describe the data will be denoted $\{\xi_i\}$*. The probability of the set of ξ_i as a function of the observed data is often not known, but one can usually construct the probability of observing a data sample given ξ_i. Bayes's theorem allows the calculation of the probability:

$$p(\{\xi_i\}|data) = \frac{p(\{\xi_i\})p(data|\{\xi_i\})}{p(data)}. \tag{7.1}$$

With no *a priori* biases, $p(\xi_i)$ is the same for all hypotheses. The denominator, $p(data)$, the likelihood of observing the data, does not depend on the ξ_i and is unimportant in what follows. One may find the optimal $\{\xi_i\}$ by maximizing the probability of the data given $\{\xi_i\}$.

This probability function can be constructed out of multiplicative components for each event in the analysis:

$$p(data|\{\xi_i\}) = \prod_{events} p(event, \{\xi_i\}) \tag{7.2}$$

The mathematical tractability of this product is improved by converting it into a sum of logarithms:

$$\ln\mathcal{L} = \sum_{events} \ln\left(p(event, \{\xi_i\})\right). \tag{7.3}$$

Often it is $-\ln\mathcal{L}$ which is used in order to allow function minimization programs to be employed. Statistical errors may be estimated from $\ln\mathcal{L}$: the region of hypothesized parameter space within 1σ of the fit value is that region for which $\ln\mathcal{L}$ is within 0.5 of its maximum value. In the case that there are several parameters to be fit, this will in general be an ellipsoid in that space, yielding both errors and statistical correlations.

*In our case, the only parameter we will fit for is A_b.

7.2 Likelihood Function

The probability of observing an event as a function of its properties is given by the differential cross-section, Equation 1.61, with the A_f as parameters to be measured or assumed. To be used as a likelihood function, though, the probability of mistagging or mis-signing an event must be incorporated. In addition, the effects of QCD radiation modify the observed distribution and must be included at this point. Overall scale factors on the differential cross-section, and even overall scale factors on individual events' probabilities do not enter, as they become constant offsets to $\ln\mathcal{L}$, and therefore affect neither the position of the maximum nor the width. The probability function used in this analysis is

$$\begin{aligned} p(event_i, A_b, A_c, A_{bckg}) = (1 - A_e P_e^i)(1 + \cos^2\theta_i) + 2(A_e - P_e)\cos\theta_i[\\ A_b f_i^b (2p_i^{correct,b} - 1)(1 - \Delta^i_{QCD,b}) + \\ A_c f_i^c (2p_i^{correct,c} - 1)(1 - \Delta^i_{QCD,c}) + \\ A_{bckg}(1 - f_i^b - f_i^c)(2p_i^{\text{"}correct\text{"},bckg} - 1)], \end{aligned} \quad (7.4)$$

where A_e is the asymmetry in electron coupling to the Z^0, P_e^i is the signed polarization of the electron beam when the event was recorded, f_i^b is the probability that that event was a $Z^0 \to b\bar{b}$ decay, and is parameterized in terms of the number of tracks missing the origin by 3σ, f_c^i is a similar quantity for the $Z^0 \to c\bar{c}$ probability, and $\Delta^i_{QCD,b,c}$ are final-state QCD corrections [58][57], to be discussed later. A_{bckg} is an estimated asymmetry from $u\bar{u}$, $d\bar{d}$, and $s\bar{s}$ decays of the Z^0. The right-sign probabilities $p_i^{correct,b}$ and $p_i^{correct,c}$ are estimated as functions of the momentum weighted charge $|Q|$ of the event, defined in Equation 6.2. The $p_i^{correct,b,c}$ parameterize how well the algorithm signs the thrust axis on an event, and may be estimated from the Monte Carlo, but as will be described in Section 7.3, they can be inferred from the data with a much reduced model dependence.

It is interesting to note that A_e appears in the probability function for the maximum likelihood technique, while it cancels from the left-right forward-backward asymmetry combination $\tilde{A}_{FB}$. In fact, it is easy to tell that its effect must vanish in the limit of a large data sample. If the experiment were run with $P_e = \pm 1$, then

$(A_e - P_e) = \mp(1 - A_e P_e)$ and the dependence on A_e vanishes entirely, because one can factor out arbitrary scale factors from the probability function for each event without affecting the answer. The experiment was run with $|P_e| < 1$, though, but the observable asymmetry should scale simply with P_e, except for the fact that a finite data sample introduces statistical fluctuations. Any dependence on A_e in the final result with this technique will scale down with increasing data sample and will also become smaller as $|P_e| \rightarrow 1$.

7.3 Calibrating the Analyzing Power

The largest systematic errors in the binned asymmetry fit arise from using the Monte Carlo to estimate the correct-sign probability. The statistical error available with the 1994–1995 data is already smaller than the systematic error in the binned fit. The goal of this section is to find some observables available in the data that provide a calibration of $p^{correct,b}(|Q|)$. The technique used takes advantage of the fact that the two hemispheres give nearly independent estimations of the correct sign of the thrust axis. Presented below is a version of the analyzing power check of Section 6.4.3 which extracts maximal information by taking advantage of the values of the hemisphere charges instead of just their relative signs.

7.3.1 Ansatz

To compute $p^{correct,b}(|Q|)$, two assumptions must be made. First, an assumption of the functional form of the momentum-weighted charge distributions in the two hemispheres of an event must be made. The form chosen here is a Gaussian. The discussion below will be cast in terms of Q_b and $Q_{\bar{b}}$, the momentum-weighted charges in the b and $\bar{b}$ hemispheres. That sometimes the b and $\bar{b}$ sometimes appear in the same hemisphere to complicate this assumption will be handled in Section 7.3.6. Relaxing the assumption that the distributions are Gaussian to determine systematic errors introduced by it will be described in Section 7.3.5. A Gaussian is likely to be a close representation of the Q_b and $Q_{\bar{b}}$ distributions because the conditions of the central

limit theorem [167] are nearly met. With a weighting exponent of $\kappa = 0.5$, no single track dominates the Q sum, and the mean B-decay multiplicity is ~5.4. For larger values of κ, single tracks become more important in the sum and the distribution becomes far less Gaussian. For $\kappa \to 0$, the distribution becomes discrete. For the case of a discrete distribution, the procedure for calibrating $p^{correct,b}$ can be performed without an assumption about the shape. The details will be given in Chapter 9.

The second assumption necessary at this point is that the momentum-weighted charges in the b and $\bar{b}$ hemispheres are statistically uncorrelated. It is important to separate the b from the $\bar{b}$ hemisphere at this point, because the momentum-weighted charges in the two hemispheres of an event are most definitely correlated: if one hemisphere has a b, the other almost certainly will have a $\bar{b}$. It is this correlation which provides the signal for the calibration; correlation in addition to this can affect the technique's accuracy. Additional correlation can arise from charge conservation in the event and the requirement that both hemispheres be color singlets. The details of how these quantities are conserved affect the interhemisphere correlation. The definition and magnitude of this extra correlation will be discussed in Section 7.3.3.

These two assumptions can be formulated with

$$p(Q_b, Q_{\bar{b}}) = p(Q_b)p(Q_{\bar{b}}), \tag{7.5}$$

with

$$p(Q_b) = \frac{1}{\sqrt{2\pi\sigma_0^2}} e^{-(Q_b+Q_0)^2/2\sigma_0^2}, \tag{7.6}$$

and

$$p(Q_{\bar{b}}) = \frac{1}{\sqrt{2\pi\sigma_0^2}} e^{-(Q_{\bar{b}}-Q_0)^2/2\sigma_0^2}, \tag{7.7}$$

where $Q_0 > 0$. is the average momentum-weighted charge in the $\bar{b}$ hemisphere, and σ_0 is the single-hemisphere charge width.

A third assumption at this point is that the momentum-weighted charge distributions do not violate CP. While not strictly true for the B hadrons [168], the decay modes with the largest CP-violating asymmetries have small branching fractions and do not affect the momentum-weighted charges because they are charge self-conjugate.

The most important CP-violating effect, though, is the presence of nuclear interactions of final-state particles with the detector material, adding extra positive charge on average to both the b and $\bar{b}$ hemispheres. This effect can be measured with the data and it is discussed in Section 7.6. The CP symmetry assumption appears in Equations 7.6 and 7.7 because

$$\langle Q_{\bar{b}} \rangle = -\langle Q_b \rangle \equiv Q_0. \tag{7.8}$$

The assumption of CP symmetry will also constrain the possible form of the hemisphere correlations.

The Monte Carlo provides a guide as to how believable these two assumptions are. Shown in Figure 7.1 are the distributions for Q_b and $Q_{\bar{b}}$, and their joint distribution. The distributions individually fit well to Gaussians. Their means are opposite at -0.57 and $+0.69$, with widths of 2.79 and 2.78, respectively. The Monte Carlo B decay model manifestly conserves CP, and so the difference in means is entirely attributable to the simulation of nuclear scattering in the detector material. The interhemisphere correlation, to be defined and discussed in Section 7.3.3, is estimated to be ~3%.

7.3.2 Correct-Sign Probability

With the assumptions that the distributions are Gaussian and uncorrelated, the function $p^{correct,b}(|Q|)$ can be determined from the data. Convenient combinations of the hemisphere momentum-weighted charges are

$$Q_{sum} = Q_b + Q_{\bar{b}}, \quad \text{and} \tag{7.9}$$

$$Q_{diff} = Q_b - Q_{\bar{b}}. \tag{7.10}$$

The unsigned event momentum-weighted charge $|Q|$ used in Chapter 6 can be identified with $|Q_{diff}|$ defined above:

$$|Q_{diff}| = |Q| = \left| \sum_{tracks} q_i |\vec{p}_i \cdot \vec{t}|^{\kappa} \mathrm{sgn}(\vec{p}_i \cdot \vec{t}) \right|, \tag{7.11}$$

and henceforth will be referred to as $|Q_{diff}|$. Only the absolute value of Q_{diff} is measurable because no knowledge of which hemisphere contains the b and which the

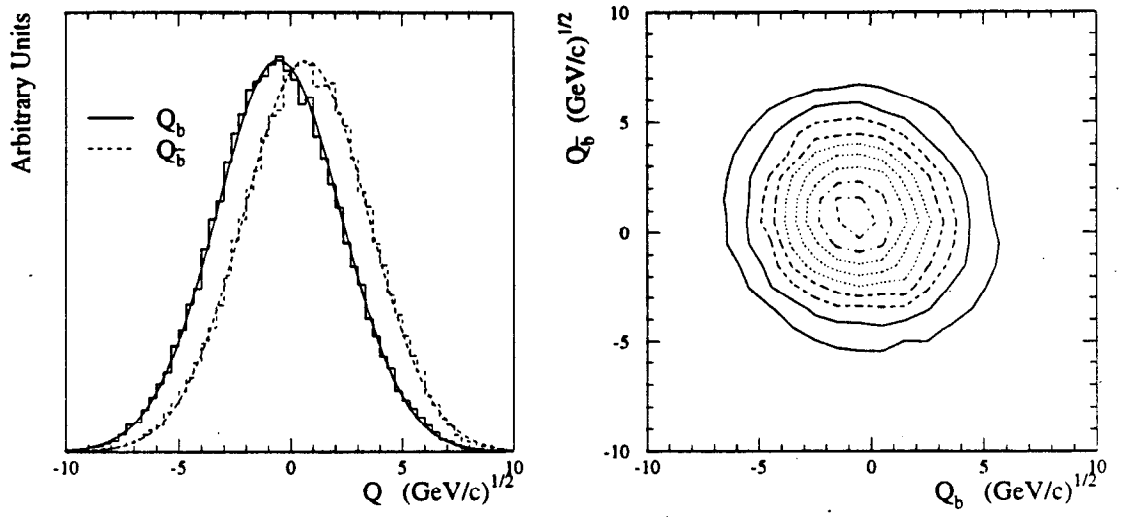

Figure 7.1: Monte Carlo distributions of Q_b and $Q_{\bar{b}}$, with fits to a Gaussian hypothesis. The joint probability distribution has a correlation of ~3%.

$\bar{b}$ is assumed. The sum of the hemisphere charges, also mentioned in Chapter 6, retains its definition:

$$Q_{sum} = \sum_{tracks} q_i |\vec{p}_i \cdot \vec{t}|^{\kappa}. \tag{7.12}$$

It can be directly measured in the data because it is invariant under an interchange of b and $\bar{b}$.

The desired correct-sign probability is the probability Q_{diff} has the sign expected from the charges of the b and $\bar{b}$:

$$p^{correct,b}(|Q_{diff}|) = p(Q_{diff} < 0). \tag{7.13}$$

In terms of the Gaussian distributions of Equations 7.6 and 7.7,

$$p(Q_{diff}) = \frac{1}{\sqrt{2\pi\sigma^2_{Q_{diff}}}} e^{-(Q_{diff}+2Q_0)^2/2\sigma^2_{Q_{diff}}} \tag{7.14}$$

where

$$\sigma_{Q_{diff}} = \sigma_0\sqrt{2} \tag{7.15}$$

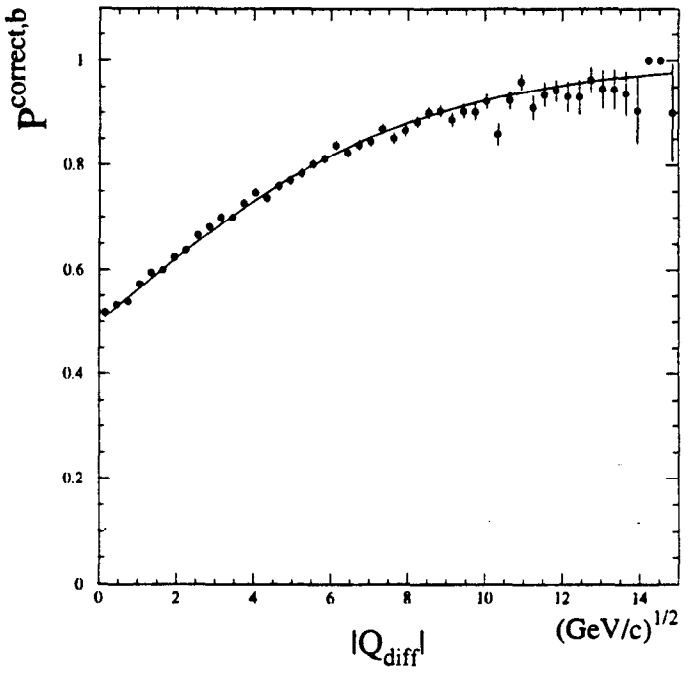

Figure 7.2: Correct-sign probability $p^{correct,b}$ as a function of $|Q_{diff}|$, as estimated from the Monte Carlo. The function appearing in Equation 7.16 with $\alpha_b = 0.2505 \pm 0.0022$ (GeV/c)$^-1/2$, where the error is statistical on the Monte Carlo.

is the width of the Q_{diff} distribution. The correct-sign probability is then given by

$$p^{correct,b}(|Q_{diff}|) = \frac{p(Q_{diff} < 0)}{p(Q_{diff} < 0) + p(Q_{diff} > 0)} = \frac{1}{1 + e^{-\alpha_b |Q_{diff}|}}, \tag{7.16}$$

with

$$\alpha_b = 4Q_0/\sigma^2_{Q_{diff}}. \tag{7.17}$$

The quantity α_b is a parameterization of how well the momentum-weighted charge technique signs the thrust axis. Larger values of α_b correspond to more reliable charge assignment, either due to a larger charge separation between b and $\bar{b}$, or smaller statistical fluctuations of the measured charge. It is also the case that

$$0.5 \leq p^{correct,b}(|Q_{diff}|) \leq 1. \tag{7.18}$$

The task then becomes how to calculate α_b from event observables. Equation 7.16 can be fit to the Monte Carlo, where the b and $\bar{b}$ axes are known and a value of α_b can be fit, but the object is to reduce the Monte Carlo dependence. Fortunately, a comparison of the widths of the $|Q_{sum}|$ and $|Q_{diff}|$ distributions provides the required information. In terms of the Gaussians of Equations 7.6 and 7.7,

$$p(Q_{sum}) = \frac{1}{\sqrt{2\pi\sigma_{sum}^2}} e^{-Q_{sum}^2/2\sigma_{sum}^2}, \tag{7.19}$$

where

$$\sigma_{sum} = \sigma_{Q_{diff}} = \sigma_0\sqrt{2} \tag{7.20}$$

is the width of the Q_{sum} distribution. The fact that Q_{sum} and Q_{diff} have the same width is a consequence of the assumption that Q_b and $Q_{\bar{b}}$ are uncorrelated. Relaxing this assumption will be discussed in Section 7.3.3. Measuring the width of the Q_{sum} distribution in the data yields σ_0 immediately.

The next step is to evaluate Q_0 from data observables. While the distribution of Q_{diff} is Gaussian, the distribution of $|Q_{diff}|$ is the sum of two Gaussians†:

$$p(|Q_{diff}|) = \frac{1}{\sqrt{2\pi\sigma_{Q_{diff}}^2}} \left(e^{-(|Q_{diff}|-2Q_0)^2/2\sigma_{Q_{diff}}^2} + e^{-(|Q_{diff}|+2Q_0)^2/2\sigma_{Q_{diff}}^2} \right). \tag{7.21}$$

This sum of two Gaussian distributions can be approximated very well by a single Gaussian distribution, as long as $Q_0 \ll \sigma_0$ ‡.

$$p(|Q_{diff}|) \simeq \frac{2}{\sqrt{2\pi\sigma_{|Q_{diff}|}^2}} e^{-|Q_{diff}|^2/2\sigma_{|Q_{diff}|}^2}. \tag{7.22}$$

The width of this single distribution may be found by setting Equations 7.21 and 7.22 equal at $|Q_{diff}|$=0 and solving for $\sigma_{|Q_{diff}|}$, yielding

$$\sigma_{|Q_{diff}|} \simeq \sigma_{Q_{diff}}(1 + 2Q_0^2/\sigma_{Q_{diff}}^2), \tag{7.23}$$

†In the high statistics limit, if Q_{sum} fits well to a Gaussian, $|Q_{diff}|$ will not. With the current data sample, however, the distributions of both Q_{sum} and $|Q_{diff}|$ are indistinguishable from Gaussian.

‡In our case, $Q_0 \simeq 0.99$ GeV$^{1/2}$, $\sigma \simeq 2.60$ GeV$^{1/2}$, and the single-Gaussian approximation to Equation 7.21 using the width of Equation 7.23 yields correct-sign probabilities which deviate by no more than 0.7% from what would be obtained without the approximation. This point will return again in Section 7.3.5. We will see that this approximation introduces a small bias to the technique which will be accounted for.

again using the approximation that $Q_0 \ll \sigma_0$. This result can also be obtained by setting the second derivative of Equations 7.21 and 7.22 equal at $|Q_{diff}|$=0.

The variable $\sigma_{|Q_{diff}|}$ is a measurable quantity; it is just the RMS deviation of $|Q_{diff}|$ from zero. The width of Q_{sum} can also be found by its RMS deviation from zero, as it is expected to have zero mean. Using Equations 7.23 and 7.20, Q_0 can be obtained in terms of observables σ_{sum} and $\sigma_{|Q_{diff}|}$:

$$Q_0 = \sqrt{(\sigma_{sum}\sigma_{|Q_{diff}|} - \sigma_{sum}^2)/2}. \tag{7.24}$$

Combining Equations 7.24 and 7.20 with 7.17, one obtains α_b in terms of data observables:

$$\alpha_b = \frac{2\sqrt{2\left(\frac{\sigma_{|Q_{diff}|}}{\sigma_{sum}} - 1\right)}}{\sigma_{sum}}. \tag{7.25}$$

The data used to calculate σ_{sum} and $\sigma_{|Q_{diff}|}$ are shown in Figure 7.3.

Because α_b can be derived from observables in the data, the technique is called *self-calibrating*. Errors introduced by modeling tracking efficiency, B decays, fragmentation, and mixing do not appear in the result because they are calibrated with this α_b. It should be noted that only data events passing the 2-D normalized impact parameter tag are used to form Q_{sum} and $|Q_{diff}|$. In this manner, a very pure sample of $Z^0 \to b\bar{b}$ events is used to calibrate its own analyzing power, and any biases introduced by the tag requirements are included in the calibration.

7.3.3 Hemisphere Correlations

The assumption that the distributions of Q_b and $Q_{\bar{b}}$ are uncorrelated has already been shown to be almost, but not quite, true. Deviations from an uncorrelated distribution will modify the expected value of α_b as obtained from σ_{sum} and $\sigma_{|Q_{diff}|}$.

The joint probability distribution of Q_b and $Q_{\bar{b}}$, in the absence of correlation, is a round, symmetric, two-dimensional Gaussian distribution (Equations 7.5-7.7). Correlations will stretch this distribution along some axis. Because the widths of the projections along the Q_b and $Q_{\bar{b}}$ axes must be equivalent by CP symmetry, the axis of deformation must be along the 45° axis shown in Figure 7.4. The correlation can

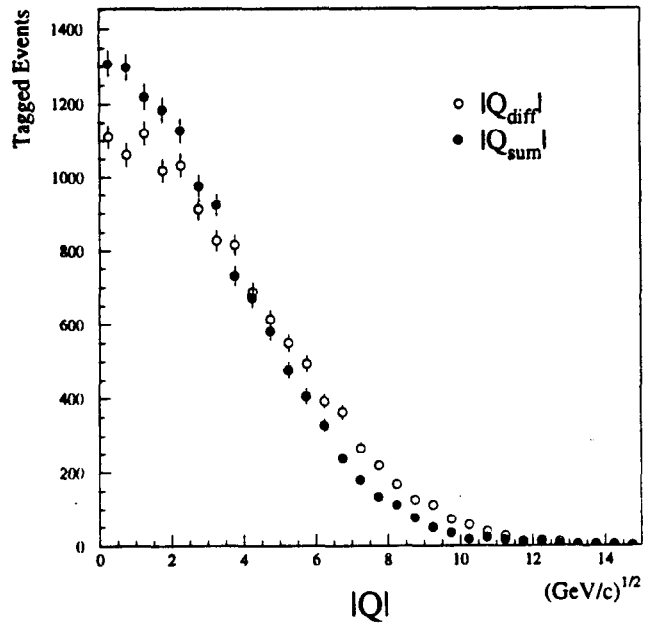

Figure 7.3: Distributions of the hemisphere charge sums and differences for 1993–1995 data with $\kappa = 0.5$.

then be defined to be

$$\lambda \equiv \frac{\sigma_{diff}}{\sigma_{sum}} - 1, \tag{7.26}$$

For the fully simulated SLD Monte Carlo $Z^0 \to b\bar{b}$ sample, $\lambda = 2.9\%$.

To incorporate λ into the calculation of the analyzing power parameter α_b, one notes that the right-sign probability $p^{correct,b}(|Q_{diff}|)$ depends only on modeling the probability distribution projected along the Q_{diff} direction, as can be seen from Equations 7.16 and 7.17. It is σ_{diff}, therefore, which is to be used in Equation 7.25. But σ_{sum} is measured, so a multiplicative correction of $(1+\lambda)$ must be applied before using it to find α_b:

$$\alpha_b = \frac{2\sqrt{2(\frac{\sigma_{|Q_{diff}|}}{(1+\lambda)\sigma_{sum}} - 1)}}{(1+\lambda)\sigma_{sum}}. \tag{7.27}$$

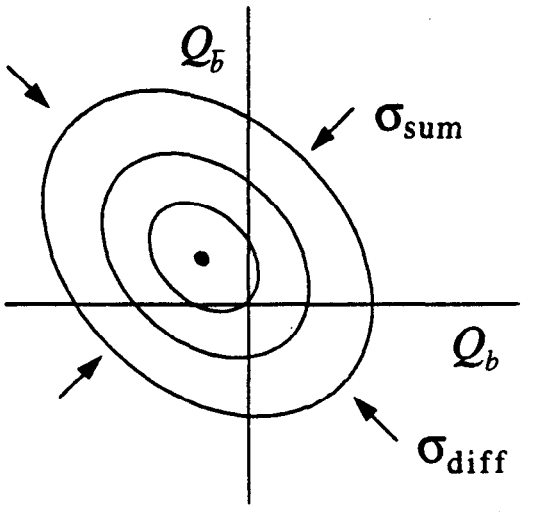

Figure 7.4: Possible effect of correlation on p(Q_b,$Q_{\bar{b}}$). CP symmetry requires that the major and minor axes of the ellipse be oriented at 45° to the Q_b and $Q_{\bar{b}}$ axes.

The magnitude of the correlation is difficult to estimate from the data itself, because a lengthening of the joint-probability distribution along the Q_{diff} axis has the same effect on Q_{diff} as an increased charge separation from a larger Q_0. There is, however, a pair of observables in each event that does in fact carry the appropriate information, $|Q_b|$ and $|Q_{\bar{b}}|$, although it cannot be determined which is which. Nonetheless, if the two unsigned hemisphere charges have some correlation, it can only arise from λ and not Q_0. This technique has not been pursued here because it is not statistically powerful enough - one would need a sample of tagged events four times as large than the one at hand in order to measure the correlation to an absolute precision of $\pm 1\%$, which would be a 30% relative error on λ, the uncertainty incurred in this analysis by using the Monte Carlo to estimate λ. This uncertainty is estimated by using different Monte Carlo models — JETSET 7.4 [30][31], HERWIG 5.7 [169], and JETSET's independent jet model — to calculate the correlation.

7.3.4 Light-Flavor Subtraction

A concern about using the widths of the momentum-weighted charge distributions to calibrate the analyzing power is that the tagged sample is not a pure sample of $Z^0 \to b\bar{b}$. The light-flavor contamination must be accounted for using a Monte Carlo model. Fortunately, though, given the nature of the widths of Q_{sum} and Q_{diff}, the light-quark fractions subtract off in quadrature and the final answer has very little dependence on the details of this subtraction.

The widths σ_{sum} and $\sigma_{|Q_{diff}|}$ are calculated by finding the RMS deviations of their respective distributions from zero:

$$\sigma_{sum} = \sqrt{\frac{1}{N} \sum_{\substack{tagged \\ events}} Q^2_{sum}}, \tag{7.28}$$

and

$$\sigma_{|Q_{diff}|} = \sqrt{\frac{1}{N} \sum_{\substack{tagged \\ events}} Q^2_{diff}}, \tag{7.29}$$

N is the number of tagged events. These expressions can be broken down into their flavor components and the light flavor parts subtracted off to give widths that correspond only to the $Z^0 \to b\bar{b}$ sample:

$$\sigma^b_{sum} = \left[\frac{\sigma^2_{sum,obs} - \Pi_c \sigma^2_{sum,c} - \Pi_{uds} \sigma^2_{sum,uds}}{\Pi_b}\right]^{\frac{1}{2}}, \tag{7.30}$$

and

$$\sigma^b_{|Q_{diff}|} = \left[\frac{\sigma^2_{|Q_{diff}|,obs} - \Pi_c \sigma^2_{|Q_{diff}|,c} - \Pi_{uds} \sigma^2_{|Q_{diff}|,uds}}{\Pi_b}\right]^{\frac{1}{2}}, \tag{7.31}$$

where $\sigma_{sum,obs}$ is the width of the sum distribution measured in the data, $\sigma_{sum,c}$ and $\sigma_{sum,uds}$ are the charm and uds widths estimated from Monte Carlo, respectively, and Π_b, Π_c, and $\Pi_{uds} = 1 - \Pi_b - \Pi_c$ are the contributions to the tag of b, c, and uds events.

The details of the light-flavor subtraction are shown in Table 7.1. It can be seen that the Monte Carlo charm widths are very similar to the data widths, and therefore do not change the average width by much in the corrections 7.30 and 7.31. The total

Table 7.1: Contributions to the light-flavor subtraction to the data σ_{sum} and $\sigma_{|Q_{diff}|}$. The "All Data" row is included for comparison. The widths have not been corrected for correlations. Errors are statistical only.

Sample	σ_{sum} (GeV/c)$^{\frac{1}{2}}$	$\sigma_{\lvert Q_{diff}\rvert}$ (GeV/c)$^{\frac{1}{2}}$	Contribution to Tag
Tagged Data	3.673 ± 0.024	4.200 ± 0.027	100%
All Data	3.684 ± 0.009	4.322 ± 0.013	—
MC $Z^0 \to b\bar{b}$	3.797 ± 0.011	4.302 ± 0.013	89%
MC $Z^0 \to c\bar{c}$	3.671 ± 0.012	4.113 ± 0.014	10%
MC $Z^0 \to uds$	3.742 ± 0.008	4.220 ± 0.010	1%

effect on α_b is a relative shift of 0.34% and is included in the systematic errors with 100% of the correction in order to be conservative.

7.3.5 Checking the Gaussian Hypothesis

The Gaussian hypothesis of Equations 7.6 and 7.7 is supported by the Monte Carlo, but the sensitivity of the analysis to the shape of Q_b and $Q_{\bar{b}}$ needs to be estimated in the case that it deviates from being Gaussian.

The technique used to determine this sensitivity is to generate a large quantity of "toy" Monte Carlo which simulates events using the differential cross-section of Equation 1.61 at a fixed value of A_b and P_e. Each event is given uncorrelated values of Q_b and $Q_{\bar{b}}$, distributed according to a probability function which is chosen arbitrarily. The constraints on this distribution are that

$$p(Q_b) = p(-Q_{\bar{b}}), \tag{7.32}$$

and the width of Q_{sum} and $|Q_{diff}|$ match those measured in the data.

Four different probability distributions were chosen, shown in Figure 7.5. The events generated with these distributions were then analyzed with the same self-calibrated maximum-likelihood technique as was used with the data, with the exception that the correlation λ was set to zero. Table 7.2 shows the estimated biases to

Table 7.2: Fit biases estimated from a Monte Carlo simulation with Q_b generated with different distributions. A positive fit bias means that the self-calibrated technique would overestimate the true asymmetry if the Q_b distribution had the hypothetical shape given.

Trial Distribution	Fit Bias ($\Delta A_b/A_b$)	χ^2 ($DOF = 12$)
Gaussian	$+(0.57 \pm 0.01)\%$	15.24
Isosceles Triangular	$-(0.4 \pm 0.1)\%$	279.6
Right Triangle (L)	$-(2.2 \pm 0.2)\%$	588.0**
Right Triangle (R)	$+(2.4 \pm 0.2)\%$	588.0**
Double Gaussian	$+(1.96 \pm 0.1)\%$	328.8

the fit when the different probability distributions of Figure 7.5 were used.

The best observable quantity which can be used to constrain the underlying momentum-weighted charge distribution is $p(|Q_{hem}|)$, where Q_{hem} is the momentum-weighted charge in a single hemisphere[§]. The absolute value for the hemisphere charge needs to be taken because it is unknown which hemisphere contains the b and which the $\bar{b}$. For each of the probability distributions in Figure 7.5, a functional form can be derived for $p(|Q_{hem}|)$, and these fit to the data distributions. The χ^2 per degree of freedom is listed for each of these, ruling out all but the Gaussian distribution at high confidence.

It was discovered with a high-statistics toy Monte Carlo run that if the momentum-weighted charge distributions are genuinely Gaussian, then there is a small bias in the fit answer, listed in Table 7.2. This correction, which is due to the approximation of Equation 7.22, will be applied to the final result, as well as on the Monte Carlo cross-check of Section 7.4 and the normalized momentum-weighted charge analysis of 7.7.

[§]The distribution of Q_{sum} is also a discriminator, but is less powerful because the distribution of the sum of two randomly distributed independent variables will in general fit better to a Gaussian than either of the components of the sum, by the Central Limit Theorem.

**The asymmetric triangle fits to $p(|Q_{hem}|)$ are optimal when the vertical side of the triangle is at $Q_{hem} = 0$, which would imply 100% analyzing power. For a more realistic analyzing power, the chisquared of these fits rises to 3,300, with 12 degrees of freedom.

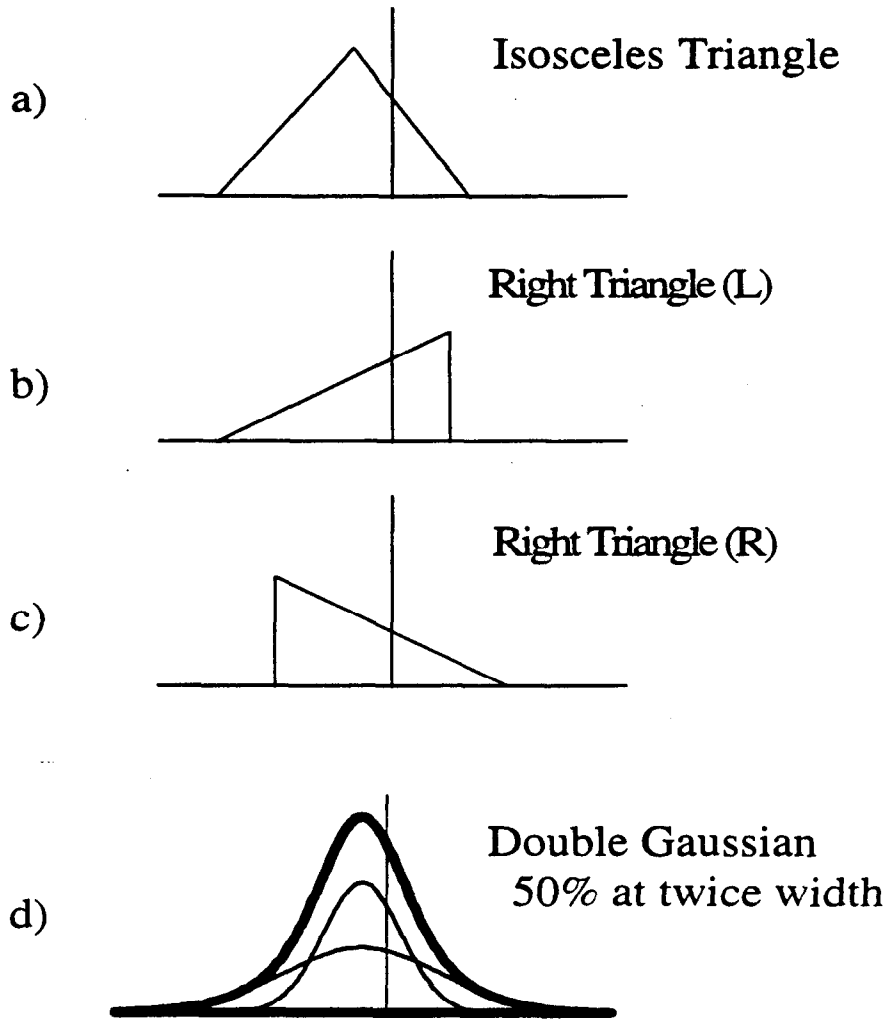

Figure 7.5: Different hypothetical Q_b distributions used to test the sensitivity of the fit to $p(Q_b)$. Each distribution is given two degrees of freedom – the mean and the width.

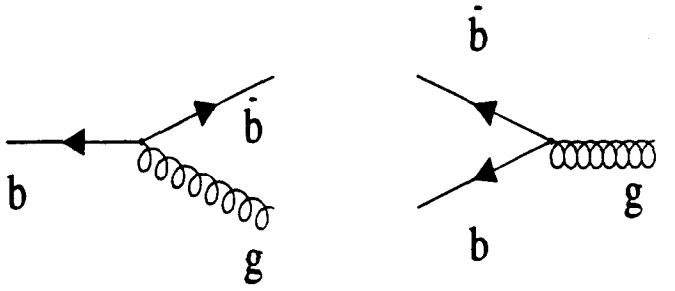

Figure 7.6: Gluon bremsstrahlung smearing the angle of the final-state quark (left), and backscattering it into the opposite hemisphere (right).

7.3.6 QCD Corrections

Corrections due to hard gluon radiation, discussed in Sections 1.5 and 6.3.1, are applied with the $\cos\theta$-dependent $1 - \Delta^i_{QCD}$ terms in the likelihood function of Equation 7.4. The self-calibrated technique introduces one complication to Δ_{QCD}, though, in that part of the correction is included in the self-calibration technique.

Most of the asymmetry dilution due to hard gluon radiation comes from smearing the quark axis before its detection. Using the thrust axis reduces the effect somewhat because the thrust axis is a more reliable indicator of the decay axis because it favors the fastest jet in the event, which has usually undergone less gluon radiation than an average jet. A second component of the QCD correction comes from events in which the gluon radiation is so hard that the two quarks end up in the same hemisphere. This affects not just the ability to find the angle, but the ability to sign the event correctly. The event-signing probability is calibrated by σ_{sum} and $\sigma_{|Q_{diff}|}$, but the angular smearing is not. The two contributions are illustrated in Figure 7.6. Figure 6.19 itemizes, using the JETSET 7.4 generator, the effects of these two contributions.

7.4 Likelihood fit to MC

A test of bias inherent in the self-calibrated maximum-likelihood fit is to generate fully simulated Monte Carlo and analyze it as if it were the data. Because the Monte Carlo is used to estimate the light flavor contamination in the tag, the errors arising from tag contamination vanish in this comparison. The Monte Carlo was generated with $A_b = 0.9357$, and the value extracted from the Monte Carlo using this technique is $A_b^{MC,meas} = 0.950 \pm 0.020(\text{stat}) \pm 0.014(\alpha \text{ stat})$.

A more serious test of the calibration and fit is to alter the analyzing power in the Monte Carlo and to re-fit for A_b. This test was performed with an additional tracking inefficiency of 20% applied randomly to the Monte Carlo. If this simulation were used to estimate A_b using the binned asymmetry fit, the value of A_b would change by a relative 40%, assuming that the corrections are still linear. The inefficient Monte Carlo is used to calibrate its own analyzing power using σ_{sum} and $\sigma_{|Q_{diff}|}$, and the fit result is $A_b^{MC,meas} = 0.991 \pm 0.032(\text{stat}) \pm 0.061(\alpha \text{ stat})$. These tests demonstrate that the technique is unbiased and that it produces a reliable result regardless of the analyzing power.

7.5 Measurement of A_b with Maximum Likelihood Track Charge

The measurement of A_b puts together the pieces described in Sections 7.1–7.3. First, events are tagged with the normalized 2-D impact parameter tag, retaining only those events with more than 3 tracks missing the origin by $+3\sigma$, the same tag used in the previous analysis. The quantities σ_{sum} and $\sigma_{|Q_{diff}|}$ are measured in the tagged data sample. The Monte Carlo is then used to estimate λ, as well as the light-flavor contributions to the the sum and difference widths. The data widths are corrected for the tag contamination using Equations 7.30 and 7.31. The value of α_b is then computed for the data with Equation 7.27, using the Monte Carlo correlation λ. The effect of hard gluon radiation is accounted for with $\Delta_{QCD}(\cos\theta)$, calculated in [58]. Systematic errors from this correction will be discussed in Section 7.6.9.

Because the tracking acceptance is not uniform in polar angle, α_b is expected to be a function of $\cos\theta$. This dependence is estimated using the Monte Carlo, while the average value of α_b is scaled to match the data. The procedure is to compute in the Monte Carlo the correct-sign probability of tagged $Z^0 \rightarrow b\bar{b}$ events as a function of $|Q_{diff}|$ and fit an α_b in each of ten bins of $\cos\theta$, as well as in the aggregate $|\cos\theta| < 0.7$. The ratio $\alpha_{b,data}/\alpha_{b,MC}^{|\cos\theta|<0.7}$ is used to scale the $\cos\theta$-dependent α values obtained from the Monte Carlo. It is these values that are used to estimate $p^{correct,b}(|Q_{diff}|)$ in the likelihood function.

The other ingredients to the likelihood function are taken from the Monte Carlo simulation. The flavor probabilities f^b and f^c are estimated as functions of the number of tracks with significant impact parameters and read from of Figure 6.11. The analyzing power function for charm is estimated from the Monte Carlo by forming $p^{correct,c}(|Q_{diff}|)$ for $Z^0 \rightarrow c\bar{c}$ events and fitting for $\alpha_c(\cos\theta)$ using Equation 7.16. The QCD correction applied to the charm portion of the likelihood function is discussed also in Reference [58] and are somewhat larger than for the b case. The value of A_c is fixed at its Standard Model value of 0.67, which is within errors of the current LEP measurement of 0.65 ± 0.05, found by combining the LEP measurement of $A_{FB}^{0,c} = 0.0729 \pm 0.0058$ [64] with the combined LEP+SLD A_e measurements, as described in Chapter 2. The reason not to fit simultaneously for A_c in this analysis is that the hard tag requirement leaves only a 10% residue of charm contamination in the sample. If the tag is weakened to include events with fewer significant tracks to allow a larger charmed sample, then A_c could indeed be measured, although its value would depend on modeling of α_c, which is estimated from Monte Carlo and therefore has large modeling uncertainties. In addition, the fraction of uds events in the weaker tags is not well understood.

The likelihood sum over all tagged events as a function of A_b is shown in Figure 7.7. Its attains its maximum value at $A_b = 0.851 \pm 0.046$, where the statistical error is estimated by finding the interval in A_b for which $\ln\mathcal{L}_{max} - \ln\mathcal{L} < 0.5$, by fitting a parabola to the likelihood function. The resulting fit value must be corrected for the estimated fractional technique bias of -0.57%, discussed in Section 7.3.5, as well as QED radiative effects, amounting to a fractional $+0.17\%$ described in Section 1.5.

Table 7.3: Details of the momentum-weighted charge maximum-likelihood fit for A_b.

	Data	Monte Carlo
σ_{sum} (GeV/c)$^{\frac{1}{2}}$	3.673 ± 0.024	3.797 ± 0.011
$\sigma_{\lvert Q_{diff}\rvert}$ (GeV/c)$^{\frac{1}{2}}$	4.200 ± 0.027	4.302 ± 0.013
α_b (GeV)$^{-\frac{1}{2}}$	0.253 ± 0.013	0.245 ± 0.005
λ	Same as MC	2.85%
Measured A_b	0.848 ± 0.046 (stat.)	0.950 ± 0.020 (stat.)
$\delta A_b/A_b$ from α_b statistics	3.4%	1.5%

A further correction arising from the b-quark's $\beta < 1$, described in Equation 1.60. lowers the measured value of A_b by a relative 0.02%. The corrected value obtained is then $A_b = 0.848 \pm 0.046$ (stat.).

7.6 Systematic Error Analysis

7.6.1 Statistical Error on α_b

The dependence of the measured A_b on α_b was determined by re-analyzing the data at several different values of α_b. The same procedure was applied to find the dependence on α_c.

$$\frac{\partial A_b}{\partial \alpha_b} = -1.944, \tag{7.33}$$

and

$$\frac{\partial A_b}{\partial \alpha_c} = -0.209. \tag{7.34}$$

The statistical error on α_b was propagated from the statistical errors on σ_{sum} and $\sigma_{|Q_{diff}|}$, and appears as an error on A_b. This error is classified as a systematic error because it is a model of the analyzing power, even if the information for it comes from the data. This error is expected to diminish in proportion to $1/\sqrt{N}$.

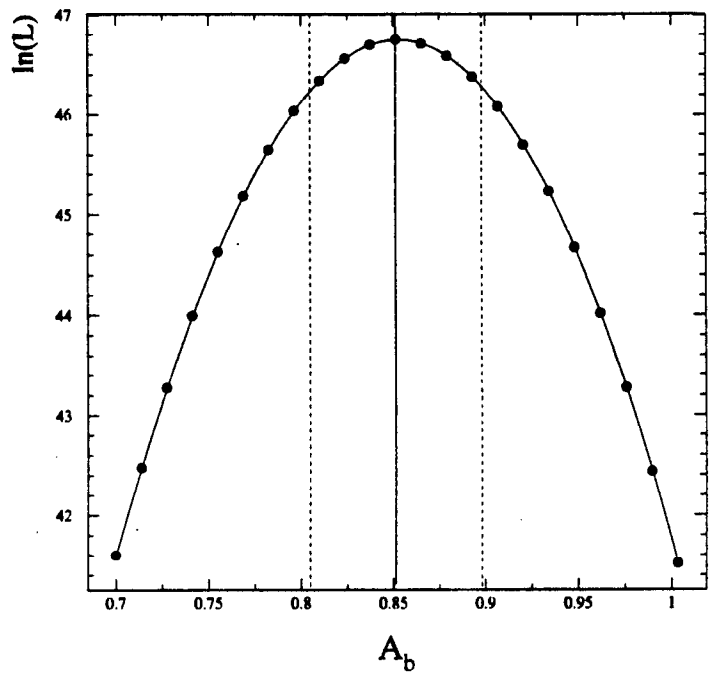

Figure 7.7: Log likelihood as a function of A_b, shown fitted to a parabola. The maximum occurs for $A_b = 0.851 \pm 0.046$.

7.6.2 Shape of the Q_b distribution

The different Q_b shapes investigated in Section 7.3.5 show a somewhat wider distribution of estimated biases than is likely to be the case for the data, indicated by the fact that none of the trial functions fits the data. A conservative estimate of the systematic error from this contribution is 1.0%.

7.6.3 Angular Dependence of α_b

Another entry for model dependence is the use of the Monte Carlo to estimate the angular dependence of α_b. Because the analyzing power of the technique is expected to fall with increasing $\cos\theta$ because of loss of tracking outside the detector acceptance, other functional forms of $\alpha_b(\cos\theta)$ can be used if they are related to tracking

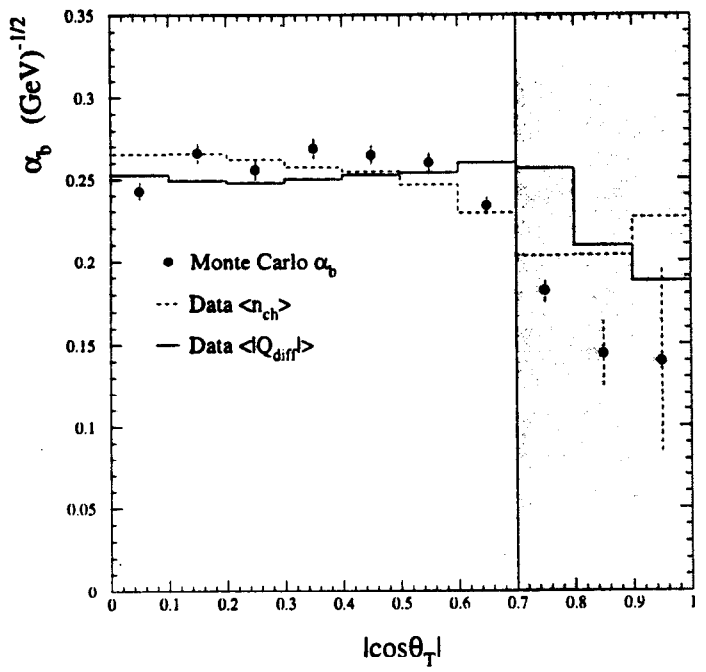

Figure 7.8: Trial shapes for the $\cos\theta$-dependence of α_b. Points are the MC estimate: the dashed line is the average multiplicity in hadronic events, and the solid line is $\langle |Q_{diff}| \rangle$ in hadronic events. Each curve has been scaled to the data α_b. The shaded region is excluded by the analysis cut.

observables in the data. The functions tried are the average multiplicity versus $\cos\theta$ for all selected hadronic events, and also the average value of $|Q_{diff}|$ for all selected hadronic events. These distributions may be scaled to the data α_b in the same way the Monte Carlo $\cos\theta$-dependent α_b was, and the variations provide a conservative estimate of the systematic error from using the Monte Carlo shape of $\alpha_b(\cos\theta)$.

7.6.4 Interhemisphere Correlation

The correlation between the momentum-weighted charges of the two hemispheres is believed to be brought about by the requirement that the total charge in the event is zero, that both hemispheres must consist only of color singlets, and also because

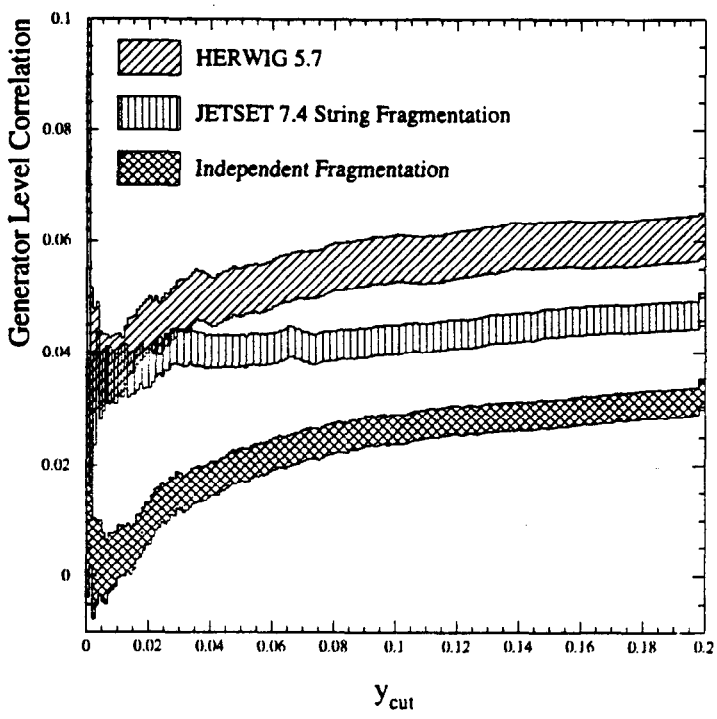

Figure 7.9: Comparison of generator-level correlations in the JETSET 7.4 string fragmentation model, JETSET's independent fragmentation option, and HERWIG 5.7. The correlations are shown for two-jet events where jets are found using the JADE algorithm [148], as a function of the jet resolution parameter y_{cut}. The widths of the shaded bands indicate the statistical error on the Monte Carlo simulation. The last bin to the right is the inclusive sample of all hadronic Monte Carlo decays.

some tracks may migrate from one hemisphere to the other, especially in events with hard gluon radiation.

The systematic error from this correlation was estimated by comparing the correlation parameter λ for three different generators: JETSET 7.4 with parton shower and string fragmentation, JETSET 7.4 with the independent fragmentation option selected, and HERWIG 5.7 with default cluster fragmentation. The generators were allowed to decay unstable products, and a simple model of detector acceptance and analysis cuts was applied.

Figure 7.9 shows the generator-level correlations for two-jet events for the two

Table 7.4: Differences between the hemisphere correlations and their effects on the measured value of A_b. The fully-simulated JETSET string model was used in the analysis and is the basis of comparison for the other models. Monte Carlo statistical errors on the estimations of λ are not propagated because the systematic variations are much larger.

Model	Generator-Level λ	Simulated λ	$\Delta A_b/A_b$
JETSET 7.4 String Frag.	$(4.82 \pm 0.25)\%$	2.85%	–
JETSET 7.4 Indep't Frag.	$(3.30 \pm 0.25)\%$	1.96%	−3.3%
HERWIG 5.7	$(6.10 \pm 0.41)\%$	3.62%	+3.2%

generators as a function of y_{cut}, using the JADE algorithm on all stable generated particles. It is expected that the more two-jet like an event is, the less correlated it will be, as the task of conserving charge at the last quark popping will have lower momentum relative to the very fast reaction products in the two jets. For a three-jet event, there is a more detailed charge conservation between the jets. Even the independent-fragmentation model shows a sizeable correlation at large values of y_{cut}.

The relative difference between the correlations of JETSET's string fragmentation model and JETSET's independent fragmentation model was then taken as an estimate of the correlation uncertainty — the discrepancy with HERWIG's correlation was found to be smaller. The sensitivity of the measured A_b to λ, holding σ_{sum} and $\sigma_{|Q_{diff}|}$ fixed, was found to be

$$\frac{\partial A_b}{\partial \lambda} = 3.34. \tag{7.35}$$

The resulting relative systematic error from hemisphere correlations is a relative 3.3%.

7.6.5 Light Flavor Subtraction

Accounting for light-flavor contamination when calculating $\sigma_{sum,b}$ and $\sigma_{|Q_{diff}|,b}$ using Equations 7.30 and 7.31 changes the resulting α_b by very little. The systematic error is conservatively taken to be the difference between using an α corrected for light-flavor contamination and using an α that omits this correction. The net effect on the measured value of A_b is a relative 0.2%.

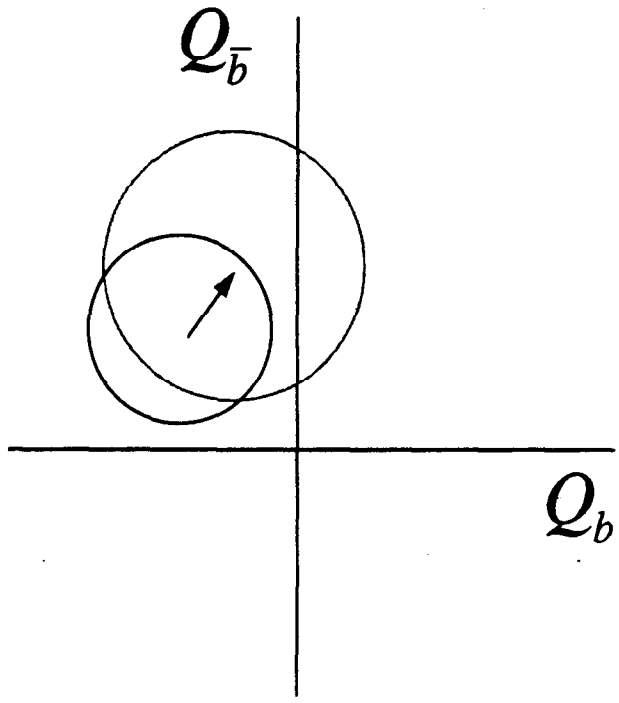

Figure 7.10: Effect of detector material on the joint probability distribution of Q_b and $Q_{\bar{b}}$. The distributions widen, and an average positive offset is given to both Q_b and $Q_{\bar{b}}$

7.6.6 Detector material

The extra positively-charged tracks introduced by nuclear scattering with the detector material have two effects on the ability of the momentum-weighted charge measurement to extract A_b. The first effect is to add some positive charge to the b and $\bar{b}$ hemispheres on average, and the second is to broaden the Q_b and $Q_{\bar{b}}$ distributions.

The second effect is calibrated by the sum and difference widths, as it makes the joint Gaussian distribution of Q_b and $Q_{\bar{b}}$ larger in both directions by the same amount. The first effect is a genuine bias to the extraction of the analyzing power. It shifts the position of the mean of the joint distribution, increasing the σ_{sum} without affecting $\sigma_{|Q_{diff}|}$. Fortunately, this bias can be measured by finding $\langle Q_{sum} \rangle$ in the

data. This has the effect of modifying the sum width:

$$\sigma_{sum} \rightarrow \sqrt{\sigma_{sum}^2 + \langle Q_{sum} \rangle^2}. \tag{7.36}$$

The measured value of $\langle Q_{sum} \rangle$ is 0.088 ± 0.034. The systematic error is taken to be the difference in the measured A_b with σ_{sum} corrected for this effect, and without, and amounts to a relative 0.1% error.

7.6.7 Light-flavor coupling asymmetries

The sensitivity of the measured A_b to the assumptions of the values of A_c, A_{uds}, and A_e was estimated by re-analyzing the data with different values to compute the derivatives:

$$\frac{\partial A_b^{meas}}{\partial A_c^{assumed}} = 0.091, \tag{7.37}$$

$$\frac{\partial A_b^{meas}}{\partial A_{bckg}^{assumed}} = 0.01, \tag{7.38}$$

and

$$\frac{\partial A_b^{meas}}{\partial A_e^{assumed}} = 0.001. \tag{7.39}$$

A feature of the likelihood function is that the assumptions for A_{bckg} and α_{bckg}, which parameterize the $p^{\text{"correct"},bckg}(|Q_{diff}|)$ of Equation 7.4, really constitute just one assumption. The strategy chosen here is to hold fixed a maximal α_{bckg}, and then to vary A_{bckg} within large limits. The α_{bckg} was chosen to be that estimated from Monte Carlo $Z^0 \rightarrow u\bar{u}$ events, the largest α of the five flavors. Then A_{bckg} was varied between $+0.5$ and -0.5; the central value chosen for the analysis was zero. The value of A_{bckg} is expected to be small because of the presence of the three light quark flavors with partially canceling charge asymmetries. The variation in the measured A_b is quoted as a 0.6% relative systematic error.

The value of A_c was fixed to the Standard Model value and its allowed range was large enough to accommodate conservatively the full range of the LEP average of 0.65 ± 0.05. The dependence of the answer on A_e has been discussed in Section 7.2, although since it appears in the likelihood function, it constitutes model dependence on the answer. Its value was chosen within the range $A_e = 0.1506 \pm 0.0028$, from

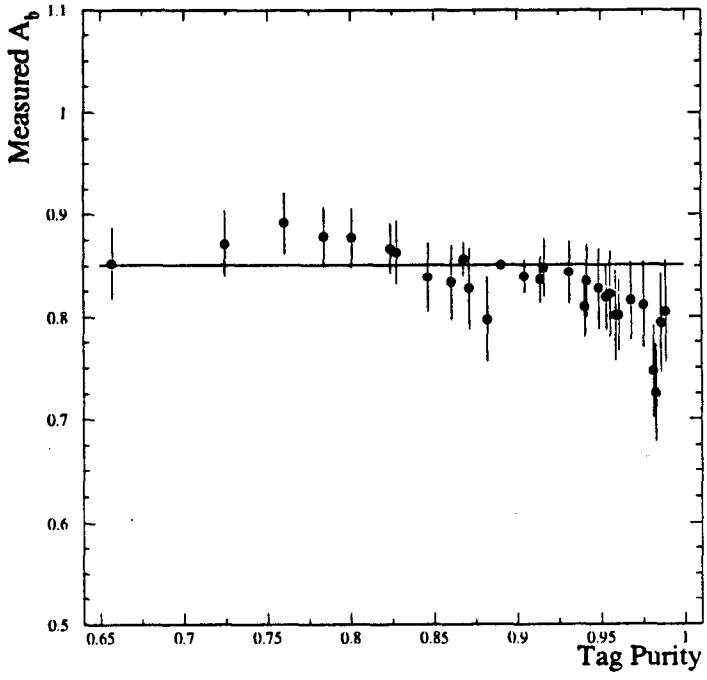

Figure 7.11: Tag dependence of the maximum-likelihood A_b measurement, for tags ranging from 2 tracks at 2σ to 4 tracks at 9σ. Correlated statistical and systematic errors have been removed, taking the 3 tracks at 3σ point (with horizontal line) as a reference.

Table 2.1, which corresponds to the combined measurement of the LEP lepton asymmetries and the SLD A_{LR} measurement.

7.6.8 Tag purity

Contributions to the systematic error arising from the modeling of the 2-D impact parameter tag are estimated with the aid of Table 6.1. Estimating the effect on the maximum-likelihood fit of A_b is done by adding extra charm contamination to the estimation of the tag composition and re-fitting for A_b. The addition of *uds* events has half of the effect on the answer, owing to its smaller asymmetry. Furthermore, it is expected that the dominant contamination to the B-tagged sample is $Z^0 \to c\bar{c}$ events, as the error from beam-position tails in Table 6.1 is not a leading contribution.

The same cross-check used for the binned asymmetry fit of checking the answer as a function of the hardness of the tag, described in Section 6.4.2, has been repeated for this analysis. The dependence, shown for tags ranging in purity from 2 tracks at 2σ to 4 tracks at 9σ, are shown in Figure 7.11.

7.6.9 QCD correction

The systematic error arising from injecting a model of hard gluon radiation has several components. There is no second-order calculation of the QCD correction using massive quarks. Instead, first-order calculations, which incorporate quark mass, are used in the analysis, and the relative size of the second-order term, compared to the massless first-order correction, are taken as a systematic error. In addition, the uncertainty in the value of α_s introduces an uncertainty in this correction. The error is taken to be the quadrature sum of the estimated mistake by omitting the second-order terms and twice the current theoretical uncertainty in the value of $\alpha_s = 0.118 \pm 0.010(theory)$.

7.7 Normalized Momentum-Weighted Charge

The approach followed by most competing analyses is to normalize the momentum-weighted charge instead of using the unnormalized sum of Equation 6.2. The normalized momentum-weighted charge is given by

$$Q_{norm} = \frac{-\sum_{tracks} q_i |\vec{p}_i \cdot \vec{t}\,|^{\kappa} \mathrm{sgn}(\vec{p}_i \cdot \vec{t}\,)}{\sum_{tracks} |\vec{p}_i \cdot \vec{t}\,|^{\kappa}} \tag{7.40}$$

This quantity can be computed in the two hemispheres of each event and the self-calibrated analysis of this chapter repeated. It is important to normalize the hemispheres separately before forming Q_{sum} and Q_{diff}, in order to minimize the hemisphere correlation. The details of this analysis are given in Table 7.6. The fit to the data has slightly larger errors from statistics and α statistics than does the unnormalized fit, although the result is in excellent agreement. The normalized fit to the Monte Carlo accurately reproduces the input value of 0.9357. The Monte Carlo distribution of Q_{norm} fits slightly less well to a Gaussian than does the unnormalized Q — the

Table 7.5: Systematic error summary for the self-calibrated maximum-likelihood measurement of A_b

Error Source	Variation	$\delta A_b/A_b$
Self-Calibration		
α_b Statistics	1σ	3.4%
$p(Q_b)$ Shape	Triangular, other shapes	1.0%
$\cos\theta$ shape of α_b	$\langle n_{ch}\rangle$ and $\langle Q_{diff}\rangle$ shapes	1.5%
Hemisphere Correlation	JETSET,HERWIG,Indep't	3.3%
Light Flavor Subtraction	100%	0.2%
Detector Material	100%	0.1%
Analysis		
A_c	0.67 ± 0.07	1.0%
A_{uds}	0.0 ± 0.50	0.6%
A_e	0.1506 ± 0.0028	$\ll 0.1\%$
α_c	Mostly $x_D \pm 5\%$	0.2%
Tag Composition	See Table 6.1	2.6%
P_e	0.8%	0.8%
QCD	$\alpha_s \pm 0.02$, 2nd order terms	0.9%
Total		5.9%

Monte Carlo $p^{correct,b}(|Q_{norm}|)$ is shown in Figure 7.12, which may be compared with Figure 7.2. The normalized momentum-weighted charge is therefore not used in this analysis.

7.8 Summary

This chapter has presented a measurement of A_b with a self-calibrated maximum-likelihood analysis. The calibration of the effectiveness of the technique was extracted from the widths of two distributions — the sum and the difference of the

Table 7.6: Details of the normalized momentum-weighted charge maximum-likelihood fit for A_b.

	Data	MC
σ_{sum}	0.3289 ± 0.0020	0.3339 ± 0.00089
$\sigma_{\lvert Q_{diff}\rvert}$	0.3745 ± 0.0024	0.37881 ± 0.00101
α_b	2.80 ± 0.14	2.70 ± 0.06
λ	Same as MC	2.51%
Measured A_b	0.8497 ± 0.048 (stat.)	0.944 ± 0.020 (stat.)
$\delta A_b/A_b$ from α statistics	3.7%	1.8%

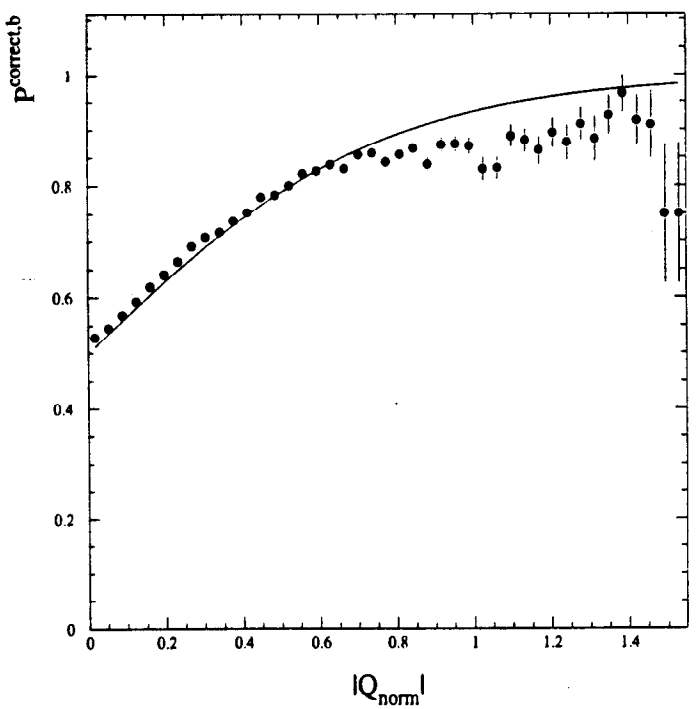

Figure 7.12: Correct-sign probability estimate for normalized momentum-weighted charge. The better fit of Figure 7.2 encourages the use of the unnormalized momentum-weighted charge.

two hemisphere's momentum-weighted charges. Residual model dependencies come from interhemisphere correlation, the composition of the b-tagged sample, and A_c. Additional systematic error comes from the statistical error on the calibration. The measured value is

$$A_b = 0.848 \pm 0.046 \text{ (stat.)} \pm 0.050 \text{ (syst.)}. \tag{7.41}$$

Chapter 8

Global Fit to Zbb Vertex Parameters

The contribution SLD makes to the knowledge of the coupling of the b quark to the Z^0 is substantial. Takeuchi, Grant, and Rosner recognized this [170] and proposed a model-independent parameterization of Zbb vertex couplings similar to the S, T, and U parameters of Peskin and Takeuchi [60][61], which describe propagator corrections. Alternative parameterizations of the vertex couplings exist [173], and the parameters are easily re-expressed in terms of those of Takeuchi, Grant, and Rosner.

8.1 Independent Parameters

There are only two independent parameters describing the coupling of any fermion to the Z^0, and different combinations have different physical interpretations *. There are the vector and axial-vector couplings v and a; there are the left-handed and right-handed couplings c_R and c_L; and there are the overall coupling strength and parity-violating asymmetry, given by the observables R_f and A_f. Because the coupling of left-handed b quarks to the Z^0 is so much stronger than the coupling of right-handed b quarks, a measurement of the overall coupling strength is most sensitive

*Some couplings are forced to zero by symmetry principles, such as the right-handed couplings to neutrinos.

to corrections to the left-handed coupling, while a measurement of the asymmetry is most sensitive to corrections to the right-handed coupling. The current experimental state places a much looser constraint on the right-handed coupling of the b quark to the Z^0 than it does the left-handed coupling. To extract the best estimate of the left and right-handed couplings, a global fit to available data sensitive to these quantities is required.

A complication arises in that the asymmetry A_b depends slightly on $\sin^2\theta_W$. Furthermore, the measurements of A^b_{FB} from LEP are indirect measurements of A_b. Those measurements are significantly dependent on $\sin^2\theta_W$ through the asymmetry in the initial state electron couplings to the Z^0.

To parameterize conveniently the dependence on the left- and right-handed b couplings and also $\sin^2\theta_W$, Takeuchi, Grant, and Rosner proposed the following scheme to perform a global fit to available observables:

$$\begin{aligned}
\sigma^0_{\rm had} &= \left[\sigma^0_{\rm had}\right]_{SM}\left(1+0.11\delta s^2+0.41\xi_b\right),\\
R_Z \equiv \Gamma_{\rm had}/\Gamma_{l^+l^-} &= [R_Z]_{SM}\left(1-0.85\delta s^2-1.02\xi_b\right),\\
R_b \equiv \Gamma_{b\bar{b}}/\Gamma_{\rm had} &= [R_b]_{SM}\left(1+0.18\delta s^2-3.63\xi_b\right),\\
R_c \equiv \Gamma_{c\bar{c}} &= [R_c]_{SM}\left(1-0.35\delta s^2+1.02\xi_b\right),\\
A_b &= [A_b]_{SM}\left(1-0.68\delta s^2-1.76\zeta_b\right),\\
A^b_{FB} = \frac{3}{4}A_eA_b &= \left[A^b_{FB}\right]_{SM}\left(1-55.7\delta s^2-1.76\zeta_b\right).
\end{aligned} \tag{8.1}$$

The variables chosen are

$$\begin{aligned}
\delta s^2 &= \sin^2\theta_W^{eff}-\left[\sin^2\theta_W^{eff}\right]_{SM},\\
\zeta_b &= (\sin\phi_b)\delta c^b_L+(\cos\phi_b)\delta c^b_R,\\
\xi_b &= (\cos\phi_b)\delta c^b_L-(\sin\phi_b)\delta c^b_R,
\end{aligned} \tag{8.2}$$

where

$$\phi_b = \tan^{-1}|c^b_R/c^b_L| \approx 0.181. \tag{8.3}$$

This linear combination of the chiral couplings $c^b_{L,R}$, defined in Chapter 1, is convenient because it forms a basis in which the measurements of production rates and ratios are orthogonal to the measurements of asymmetries.

Table 8.1: Measured observables contributing to the global fit to Zbb vertex parameters. The measurements are preliminary results reported at the 1995 Summer Europhysics Conference in Brussels [64]. The SLD measurement of A_b comes from this thesis, the semileptonic b asymmetry measurement [47], and the kaon measurement [50]. The value of $\sin^2\theta_W$ from LEP is averaged only over lepton channel measurements to avoid circularity. The SM predictions were obtained using ZFITTER [51], with m_{Higgs} = 300 GeV/c^2, m_t = 180 GeV/c^2, and $\alpha_s = 0.117$, and $\alpha_{EM} = 1/128.96$ [171].

Measurement	Value	SM Prediction
$\sin^2\theta_W$ (SLD)	0.23049 ± 0.0050	0.23163
$\sin^2\theta_W$ (LEP)	0.23160 ± 0.0049	0.23163
A_b (SLD)	0.859 ± 0.053	0.9346
A^b_{FB} (LEP)	0.0997 ± 0.0031	0.10247
$\sigma^0_{\rm had}$ (LEP)	41.488 ± 0.078 nb	41.485
R_Z (LEP)	20.788 ± 0.039	20.730
R_b (LEP, SLD)	0.2219 ± 0.0017	0.21552
R_c (LEP)	0.1540 ± 0.0074	0.1723

8.2 Fit Inputs

The best available data at the time of this writing comes from presentations at the 1995 Europhysics conference [64][65], and a summary of available observables is given in Table 8.1. In addition to the observables, Standard Model values must be calculated for these observables. The most poorly constrained parameters important to the predictions of these quantities are the values of m_t, m_{Higgs}, and $\alpha_s(m_Z)$. The values chosen for this analysis are m_t=180 GeV, m_{Higgs}=300 GeV, and $\alpha_s(m_Z) = 0.120 \pm 0.006$, as determined from event shapes, jet rates, and energy correlations. A fit value of α_s using lineshape data would introduce correlations with the $\sigma^0_{\rm had}$ and R_Z inputs to the fit. In what will be shown below, the range of predictions of the Standard Model for a range of m_t and m_{Higgs} will be shown.

8.3 Constraints on Parameters

A global fit to the available data taking into account experimental correlations has been performed by Bruce Schumm [172], and the results are summarized here. It can be seen that the rate parameter ξ_b differs from its expected value in excess of 3σ, while the asymmetry parameter ζ_b differs by 2σ. These are shown graphically in Figures 8.1 and 8.2.

$$\delta s^2 = -0.00055 \pm 0.00036 \tag{8.4}$$

$$\delta \xi_b = -0.0047 \pm 0.0015 \tag{8.5}$$

$$\delta \zeta_b = 0.032 \pm 0.018 \tag{8.6}$$

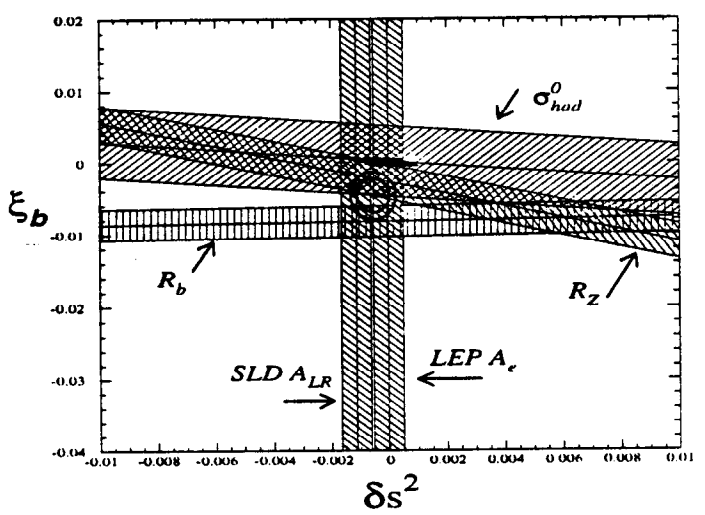

Figure 8.1: Combined constraints on the b rate-like parameter ξ_b shown with δs^2. The band for R_c falls below the figure with a large error bar. The ellipses are the 68% and 95% confidence-level fits to the bands in the figure, and the parallelogram is the range of Standard Model predictions, with $m_t = 192$ on the top side, $m_t = 168$ on the bottom, $m_H = 60$ on the left side, and $m_H = 1000$ on the right. This diagram displays graphically the discrepancy of the R_b measurements with the Standard prediction, perhaps suggesting new phenomena which modify the Zbb coupling.

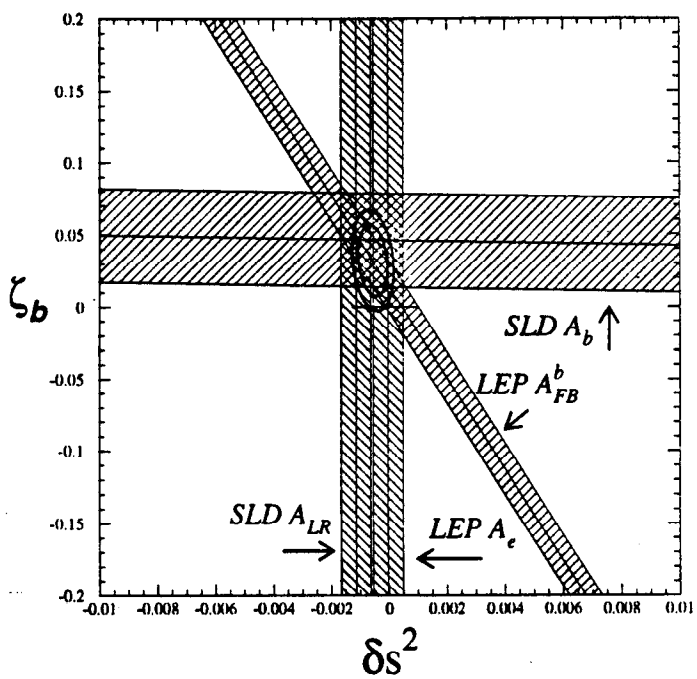

Figure 8.2: Combined constraints on the b asymmetry-like parameter ζ_b shown with δs^2. The ellipses are the 68% and 95% confidence-level fits to the bands in the figure, and the horizontal line is the Standard Model allowing m_t to vary between 168 and 192 GeV/c^2, and allowing m_H to vary between 60 and 1000 GeV/c^2. Light Higgs and heavy top correspond to the leftmost Standard Model points. The Standard Model's prediction for ζ_b, probed most directly by measurements of A_b, is rather rigid under variations of its parameters.

Chapter 9

Summary and Outlook

9.1 Results and Comparison

This thesis has presented two direct measurements of A_b, the parity-violating asymmetry of the coupling of b quarks to the Z^0 boson. The first technique lifetime-tags $Z^0 \rightarrow b\bar{b}$ events and fits the data binned to form the left-right forward-backward asymmetry where the thrust axis has been signed with the event momentum-weighted track charge. The SLD Monte Carlo, incorporating JETSET 7.4, the CLEO B meson decay model, and GEANT detector simulation, was used to estimate the effectiveness of the momentum-weighted track charge assignment and to correct for efficiency, acceptance, and resolution effects, as well as the effects of initial-state QED radiation and final-state gluon radiation. This measurement yields

$$A_b = 0.828 \pm 0.054(\text{stat.}) \pm 0.070(\text{syst.}). \tag{9.1}$$

The systematic error arises almost entirely from the use of the Monte Carlo to estimate the performance of the momentum-weighted charge-signing procedure and the composition of the tag.

The second technique, a self-calibrated maximum-likelihood method, was developed in order to reduce the total error on the measurement as an increasingly large sample of hadronic Z^0 decays becomes available. It minimizes the statistical error on the measurement by taking advantage of the magnitude of the momentum-weighted

charge of each event, as well as its sign. Each event receives its own weight in the likelihood sum depending on how reliable the estimation of the sign is.

The systematic error in the maximum-likelihood technique has been reduced by introducing a calibration procedure which uses the data almost exclusively to estimate how often the momentum-weighted track charge signs $Z^0 \to b\bar{b}$ events properly. This technique uses the momentum-weighted charge in the two hemispheres of each event to determine the correct-sign probability. Residual model dependence comes from estimating the correlation of the momentum-weighted charge in the two hemispheres of an event, estimating the light-flavor contamination to the tag and its asymmetry, and the modeling of QCD final-state radiation. The resulting measurement of this analysis is

$$A_b = 0.848 \pm 0.046(\text{stat.}) \pm 0.050(\text{syst.}). \tag{9.2}$$

While these measurements and the Standard Model prediction of $A_b = 0.936$ are consistent, higher-precision measurements in the future may begin to show a deviation.

SLD is in a unique position to measure A_b because experiments with unpolarized beams may only measure the combination $A^b_{FB} = \frac{3}{4}A_e A_b$, while SLC's polarized electron beam allows a factorization of the component asymmetries. If one takes the average A^b_{FB} from the four LEP experiments and divides it by $A_e = 0.1506 \pm 0.0028$ as determined from lepton forward-backward asymmetries, then the LEP measurement of A_b is [174]

$$A_b = 0.883 \pm 0.032, \tag{9.3}$$

where lepton and momentum-weighted track charge measurements from each of the four experiments have been combined*. It can be seen in Chapter 2 that the measurement presented in this thesis is one of the the best measurements† of A_b at present, and uses only 150,000 Z^0 decays.

*L3 did not contribute a momentum-weighted track charge measurement.

†Only the ALEPH semileptonic A^b_{FB} has a smaller total error. It is one of the outputs of a fit for A^c_{FB}, χ_B, and $\text{Br}(b \to c \to l)$, and so errors on these other outputs are not included in the error on A_{FB}.

9.2 Track Charge Prospects

Even with the calibration from the data, the systematic error on the measurement of Chapter 7 is larger than the statistical error. If the necessary precision of ~1% is to be achieved, further work must be done on the systematic error. The statistical error on α_b will scale with $1/\sqrt{N}$, where N is the total event count, and the error on the tag composition may be reduced by using tighter event tags or hemisphere double tags. The correlation error appears to be the most difficult to understand.

One approach to reduce the error from uncertainties in the hemisphere correlation is to measure it from the data. The procedure of finding the correlation of the unsigned hemisphere charges was described in Section 7.3.3, although its statistical power is limited by available data. A search for more effective measurements of the correlation should be made.

A strategy for improving the momentum-weighted track charge technique is to try different weighting functions rather than raising the momentum to a fixed power. Care must be taken, however, not to choose a function merely because it maximizes the observed asymmetry in the data, as that can introduce measurement bias.

Other information can be used to help discriminate b from $\bar{b}$. The VXD offers precise measurements of track impact parameters to the IP. Extra weight could be given to those tracks with significant impact parameters, or to identified kaons, electrons, or muons.

Progress is being made to improve the b-tag. A three-dimensional probability tag [147] can provide an event tag that has a b-purity of ~95% at the same efficiency as the tag used in this thesis. This can reduce the systematic error contributions from the tag composition by a factor of two, and reduce the statistical error at the same time. The raw statistical error is expected to scale inversely with $\sqrt{\epsilon\Pi}$, where ϵ is the tagging efficiency and Π is the purity, a result which can be obtained from Equation 6.5.

9.3 New Techniques

The main shortcoming of momentum-weighted track charge is its analyzing power of ~36%. The statistical power of the technique scales as $1/(AP \cdot P_e \cdot \sqrt{N})$, and the large gains can be made by increasing AP. "Exclusive" techniques have higher AP but also a reduced N, because they must select a specific, and often very restricted, subsample of events that have a high average analyzing power.

A measurement using charged kaons [50] has already been performed at SLD. Kaon tags can be used alone or in combination with vertexing to achieve a sample with a high-purity of correctly-signed $Z^0 \rightarrow b\bar{b}$ events.

Measurements of A_c using D^* mesons have been recently performed at SLD [175][176] and elsewhere [177][178][179]. These measurements typically use a hard momentum cut on the D^* in order to reject cascade $B \rightarrow D^*$ decays. The SLD analysis also uses displaced vertices and the precise beam spot to reject cascaded decays because the B and D flight paths are not collinear. These analyses can open their requirements to include $B \rightarrow D^*$ and fit for A_b as well as A_c. The analyzing power of the D^* is very high, although B mixing has to be accounted for.

Recently an effort has been invested in finding topological vertices using the VXD [180]. It has been used successfully to separate enriched samples of B^0 and $B^\pm$ mesons for a measurement of the lifetime ratio $\tau_{B^\pm}/\tau_{B^0}$. A pure sample of B^+ mesons could identify every event's decay axis sign correctly in an asymmetry analysis. The only tasks are to raise the efficiency sufficiently, and to measure the purity.

All of these techniques will benefit from using SLD's upgraded vertex detector, VXD3 [181]. The upgraded detector will increase the lever arm of the measurement by expanding the outer layers while the inner layer stays fixed. Each layer will have larger CCD's that are half as thick as those of the current detector. The expected measurement errors on impact parameters and vertex locations are about half those of the current vertex detector over the entire momentum range. This new detector will greatly improve the ability to assign tracks to vertices unambiguously, which will aid in determining the charge of long-lived heavy hadrons. It will also allow more efficient samples of D^* mesons to be made, because tightening the requirements on

the vertex will allow other selection cuts to be relaxed.

9.4 Calibrating New Techniques

The analyzing power of the new techniques is not expected to be exactly unity — mixing, double-charm decay, and other physics effects, as well as detector response, will reduce the analyzing power. The distributions of discriminating variables for these new techniques is often discrete, so the Gaussian approximation of Chapter 7 will not be useful.

The analyzing power for a technique with a discrete-valued discriminant can still be calibrated using the data from the two event hemispheres, though. If $P_b(n)$ is the probability of observing n in the b hemisphere, and

$$P_{\bar{b}}(n) = P_b(-n) \tag{9.4}$$

is the probability of observing n in the $\bar{b}$ hemisphere, assuming CP symmetry. If we define hemisphere sums and differences as in Chapter 7,

$$n_{sum} = n_b + n_{\bar{b}}, \quad \text{and} \tag{9.5}$$

$$n_{diff} = n_b - n_{\bar{b}}, \tag{9.6}$$

then the probabilities $P_s(n_{sum})$ and $P_d(|n_{diff}|)$ are directly measurable from the data. If CP symmetry holds, then the condition

$$P_s(n_{sum}) = P_s(-n_{sum}) \tag{9.7}$$

can be used to improve the statistical power.

This leads us to an over-constrained system of quadratic equations:

$$P_s(|n_{sum}|) = \sum_{|n_b+n_{\bar{b}}|=|n_{sum}|} P_b(n_b)P_b(-n_{\bar{b}}), \quad \text{and} \tag{9.8}$$

$$P_d(|n_{diff}|) = \sum_{|n_b-n_{\bar{b}}|=|n_{diff}|} P_b(n_b)P_b(-n_{\bar{b}}). \tag{9.9}$$

If one is interested in solving for $2N+1$ values of $P_b(n)$, where $n \in [-N, N]$, then one has $4N+2$ equations above to constrain them, as $|n_{sum,diff}| \in [0, 2N]$. In addition, there is the constraint that $P_b(n)$ be normalized.

This procedure makes no assumptions about the shape of $P_b(n)$, so virtually any combination of detector variables may be used without concern about modeling its distribution. It does assume that the hemispheres are uncorrelated, though, and it works best when the fraction of events with both hemispheres contributing information is high. Combination techniques with momentum-weighted track charge may be used to improve the efficiency to perform this calibration.

Techniques which provide continuous outputs from unknown distributions can also be calibrated with this procedure, if the measured observables are first binned. Understanding the underlying distributions, however, will always provide an advantage.

9.5 Outlook

SLC is scheduled to run until 1998, by which time 500,000 hadronic Z^0 decays are expected to have been recorded. The LEP ring at CERN stopped running at the Z^0 in October, 1995, leaving SLD in a leading position in tests of the Electroweak Standard Model. The analysis presented in this thesis is one of the important tests that can be made at SLD and may, with improvements available with more data, reach the precision necessary to discriminate between extensions to the current models.

Appendix A

SLD Collaboration

K. Abe,[29] I. Abt,[14] C.J. Ahn,[26] T. Akagi,[27] N.J. Allen,[4] W.W. Ash,[27]†
D. Aston,[27] K.G. Baird,[25] C. Baltay,[33] H.R. Band,[32] M.B. Barakat,[33]
G. Baranko,[10] O. Bardon,[16] T. Barklow,[27] A.O. Bazarko,[11] R. Ben-David,[33]
A.C. Benvenuti,[2] T. Bienz,[27] G.M. Bilei,[22] D. Bisello,[21] G. Blaylock,[7]
J.R. Bogart,[27] T. Bolton,[11] G.R. Bower,[27] J.E. Brau,[20] M. Breidenbach,[27]
W.M. Bugg,[28] D. Burke,[27] T.H. Burnett,[31] P.N. Burrows,[16] W. Busza,[16]
A. Calcaterra,[13] D.O. Caldwell,[6] D. Calloway,[27] B. Camanzi,[12]
M. Carpinelli,[23] R. Cassell,[27] R. Castaldi,[23][a] A. Castro,[21] M. Cavalli-Sforza,[7]
E. Church,[31] H.O. Cohn,[28] J.A. Coller,[3] V. Cook,[31] R. Cotton,[4]
R.F. Cowan,[16] D.G. Coyne,[7] A. D'Oliveira,[8] C.J.S. Damerell,[24] M. Daoudi,[27]
R. De Sangro,[13] P. De Simone,[13] R. Dell'Orso,[23] M. Dima,[9] P.Y.C. Du,[28]
R. Dubois,[27] B.I. Eisenstein,[14] R. Elia,[27] E. Etzion,[4] D. Falciai,[22]
M.J. Fero,[16] R. Frey,[20] K. Furuno,[20] T. Gillman,[24] G. Gladding,[14]
S. Gonzalez,[16] G.D. Hallewell,[27] E.L. Hart,[28] Y. Hasegawa,[29] S. Hedges,[4]
S.S. Hertzbach,[17] M.D. Hildreth,[27] J. Huber,[20] M.E. Huffer,[27] E.W. Hughes,[27]
H. Hwang,[20] Y. Iwasaki,[29] D.J. Jackson,[24] P. Jacques,[25] J. Jaros,[27]
A.S. Johnson,[3] J.R. Johnson,[32] R.A. Johnson,[8] T. Junk,[27] R. Kajikawa,[19]
M. Kalelkar,[25] H. J. Kang,[26] I. Karliner,[14] H. Kawahara,[27] H.W. Kendall,[16]
Y. Kim,[26] M.E. King,[27] R. King,[27] R.R. Kofler,[17] N.M. Krishna,[10]
R.S. Kroeger,[18] J.F. Labs,[27] M. Langston,[20] A. Lath,[16] J.A. Lauber,[10]

D.W.G. Leith,[27] M.X. Liu,[33] X. Liu,[7] M. Loreti,[21] A. Lu,[6] H.L. Lynch,[27]
J. Ma,[31] G. Mancinelli,[22] S. Manly,[33] G. Mantovani,[22] T.W. Markiewicz,[27]
T. Maruyama,[27] R. Massetti,[22] H. Masuda,[27] E. Mazzucato,[12]
A.K. McKemey,[4] B.T. Meadows,[8] R. Messner,[27] P.M. Mockett,[31]
K.C. Moffeit,[27] B. Mours,[27] G. Müller,[27] D. Muller,[27] T. Nagamine,[27]
U. Nauenberg,[10] H. Neal,[27] M. Nussbaum,[8] Y. Ohnishi,[19] L.S. Osborne,[16]
R.S. Panvini,[30] H. Park,[20] T.J. Pavel,[27] I. Peruzzi,[13][b] M. Piccolo,[13]
L. Piemontese,[12] E. Pieroni,[23] K.T. Pitts,[20] R.J. Plano,[25] R. Prepost,[32]
C.Y. Prescott,[27] G.D. Punkar,[27] J. Quigley,[16] B.N. Ratcliff,[27] T.W. Reeves,[30]
J. Reidy,[18] P.E. Rensing,[27] L.S. Rochester,[27] J.E. Rothberg,[31] P.C. Rowson,[11]
J.J. Russell,[27] O.H. Saxton,[27] S.F. Schaffner,[27] T. Schalk,[7] R.H. Schindler,[27]
U. Schneekloth,[16] B.A. Schumm,[15] A. Seiden,[7] S. Sen,[33] V.V. Serbo,[32]
M.H. Shaevitz,[11] J.T. Shank,[3] G. Shapiro,[15] S.L. Shapiro,[27] D.J. Sherden,[27]
K.D. Shmakov,[28] C. Simopoulos,[27] N.B. Sinev,[20] S.R. Smith,[27] J.A. Snyder,[33]
P. Stamer,[25] H. Steiner,[15] R. Steiner,[1] M.G. Strauss,[17] D. Su,[27]
F. Suekane,[29] A. Sugiyama,[19] S. Suzuki,[19] M. Swartz,[27] A. Szumilo,[31]
T. Takahashi,[27] F.E. Taylor,[16] E. Torrence,[16] J.D. Turk,[33] T. Usher,[27]
J. Va'vra,[27] C. Vannini,[23] E. Vella,[27] J.P. Venuti,[30] R. Verdier,[16]
P.G. Verdini,[23] S.R. Wagner,[27] A.P. Waite,[27] S.J. Watts,[4]
A.W. Weidemann,[28] E.R. Weiss,[31] J.S. Whitaker,[3] S.L. White,[28]
F.J. Wickens,[24] D.A. Williams,[7] D.C. Williams,[16] S.H. Williams,[27]
S. Willocq,[33] R.J. Wilson,[9] W.J. Wisniewski,[5] M. Woods,[27] G.B. Word,[25]
J. Wyss,[21] R.K. Yamamoto,[16] J.M. Yamartino,[16] X. Yang,[20] S.J. Yellin,[6]
C.C. Young,[27] H. Yuta,[29] G. Zapalac,[32] R.W. Zdarko,[27] C. Zeitlin,[20]
Z. Zhang,[16] and J. Zhou,[20]

[1]*Adelphi University, Garden City, New York 11530*
[2]*INFN Sezione di Bologna, I-40126 Bologna, Italy*
[3]*Boston University, Boston, Massachusetts 02215*
[4]*Brunel University, Uxbridge, Middlesex UB8 3PH, United Kingdom*

[5] *California Institute of Technology, Pasadena, California 91125*
[6] *University of California at Santa Barbara, Santa Barbara, California 93106*
[7] *University of California at Santa Cruz, Santa Cruz, California 95064*
[8] *University of Cincinnati, Cincinnati, Ohio 45221*
[9] *Colorado State University, Fort Collins, Colorado 80523*
[10] *University of Colorado, Boulder, Colorado 80309*
[11] *Columbia University, New York, New York 10027*
[12] *INFN Sezione di Ferrara and Università di Ferrara, I-44100 Ferrara, Italy*
[13] *INFN Lab. Nazionali di Frascati, I-00044 Frascati, Italy*
[14] *University of Illinois, Urbana, Illinois 61801*
[15] *Lawrence Berkeley Laboratory, University of California, Berkeley, California 94720*
[16] *Massachusetts Institute of Technology, Cambridge, Massachusetts 02139*
[17] *University of Massachusetts, Amherst, Massachusetts 01003*
[18] *University of Mississippi, University, Mississippi 38677*
[19] *Nagoya University, Chikusa-ku, Nagoya 464 Japan*
[20] *University of Oregon, Eugene, Oregon 97403*
[21] *INFN Sezione di Padova and Università di Padova, I-35100 Padova, Italy*
[22] *INFN Sezione di Perugia and Università di Perugia, I-06100 Perugia, Italy*
[23] *INFN Sezione di Pisa and Università di Pisa, I-56100 Pisa, Italy*
[25] *Rutgers University, Piscataway, New Jersey 08855*
[24] *Rutherford Appleton Laboratory, Chilton, Didcot, Oxon OX11 0QX United Kingdom*
[26] *Sogang University, Seoul, Korea*
[27] *Stanford Linear Accelerator Center, Stanford University, Stanford, California 94309*
[28] *University of Tennessee, Knoxville, Tennessee 37996*
[29] *Tohoku University, Sendai 980 Japan*
[30] *Vanderbilt University, Nashville, Tennessee 37235*
[31] *University of Washington, Seattle, Washington 98195*
[32] *University of Wisconsin, Madison, Wisconsin 53706*

[33] *Yale University, New Haven, Connecticut 06511*

† *Deceased*

[a] *Also at the Università di Genova*

[b] *Also at the Università di Perugia*

Appendix B

Compton Polarimeter Online Software

The SLD Compton polarimeter measures the electron beam polarization by backscattering 532 nm laser photons off of the electron beam as it passes through the South Final Focus. Its operation is described in Chapter 3. In this Appendix the details of the online acquisition system specific to the Compton Polarimeter are given.

B.1 Structure and Requirements

Figure B.1 gives an overall road map to the acquisition, and provides an outline to the tasks performed. These tasks are:

- to acquire data from the hardware;
- to check the data for integrity;
- to calculate polarization and other useful quantities, such as signal and noise averages;
- to log the data to the SLD acquisition tape;
- to display the data online for monitoring and diagnostics;

- to distribute the calculated polarization to SLC and keep a history of it;
- to display the calculated polarization on the SLD status display, as well as detailed detector and data status;
- to perform routine scans of polarimeter detector parameters to control systematic errors;
- to provide remote control of the detector for diagnostics and measurements of systematic effects;
- to limit access to the control features to ensure that no hardware option is adjusted during data taking or during a special systematic test;
- to allow full monitoring ability, even for those users not directly controlling the data flow;
- to operate automatically with a minimum of intervention from shift personnel; and
- to be easy to upgrade when the Compton hardware is modified.

These tasks are similar to those faced by most of the online acquisition systems on SLD, and therefore the acquisition has a similar structure. The model used is a distributed client-server structure, in which the main acquisition chain is performed by dedicated batch processes, and individual users may run their own client programs in order to observe or modify the acquisition process or control detector parameters.

One of the most basic elements of a real-time acquisition system is hardware that can guarantee a response when data are ready at the inputs. The SLD host computer, a VAX 8800 running VMS, a commercial time-sharing operating system, is not able to guarantee timely response to external inputs. To implement a real-time acquisition using such a host computer, additional hardware is necessary. The choice made was to use a DEC RT MicroVAX running VAXELN, an operating system built for real-time data acquisition and control tasks. The ADC's and control modules reside in three CAMAC crates, which are controlled by a Kinetic Systems 2160 Serial Highway

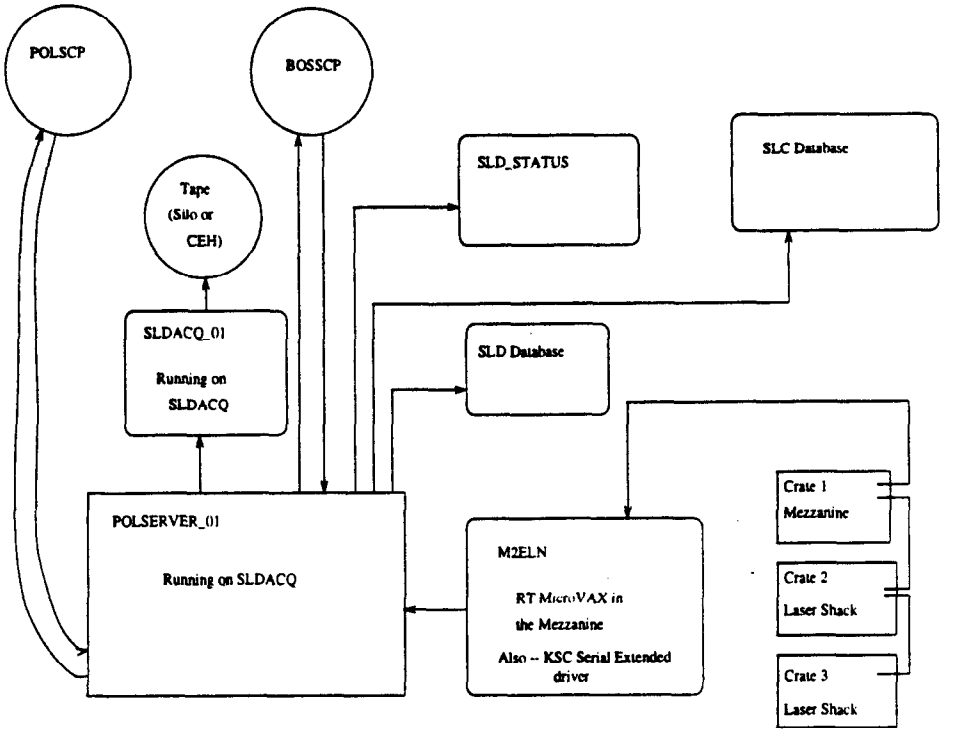

Figure B.1: Schematic diagram of the Compton polarimeter data acquisition.

Driver. One of the crates occupies a space in a rack in the mezzanine of the Collider Experimental Hall (CEH), while the other two are situated in the Compton Laser Shack and are linked by fiber optic cable to the first crate. Each crate has a Kinetic Systems enhanced serial crate controller and a CAMAC list sequencer. On each beam crossing, a pre-loaded list of CAMAC commands executes within each crate, and the resulting data are transferred to the MicroVAX via the Serial Highway Driver.

The MicroVAX accumulates the data in a buffer, and checks to see if the I/O operations completed properly and on time. After a fixed number of beam crossings (usually 400), the accumulated buffer is sent to SLDACQ, the host VAX.

A dedicated process on SLDACQ, called POLSERVER, receives the data. It forms the averages of the signals from each channel of the polarimeter, binned separately for the four $e-\gamma$ helicity combinations and also for the states in which the laser is off. Statistical errors are also formed for each of the averages. After a fixed accumulation

time, usually 20,000 beam crossings, the polarization is calculated.

B.2 Raw Data

Also calculated is the *quality factor,* defined to be the ratio of the mean square of the background-subtracted signal in a polarimeter channel, divided by the mean square deviation of the background from its average value. This was chosen because random fluctuations of the background can make the statistical errors of the measurement poor, especially when the signal strength is poor. If the background is high but very constant on a pulse-to-pulse basis, then the polarization measurement becomes statistically precise. Random fluctuations of the Compton scattering signal contribute the most to the statistical error on the polarization measurement, but these are caused by the temporal and spatial structure of the Compton laser pulse, and are therefore not under the control of shift operators and are omitted from the quality factor. Examples of a typical Cherenkov channel's response during clean running and dirty running are shown in Figures B.2 and B.3.

During the accumulation, raw data is written to tape. It consists of the raw readings for each channel in the acquisition, listed in Table B.1. These are written out only on those pulses on which the laser fires, and one pulse with the laser off for each pulse with the laser on, in order to save data tape, without significantly reducing the statistical power of the average. The averages formed online and the sums written in the summary records contain information from all collected beam crossings.

B.3 Summed Data

The averages and errors are calculated for each channel's signal binned on the different helicity states. The beam crossings are subject to data-quality vetoes, though, in order to insure a stable measurement of the polarization. These vetoes consist of:

- *Electron Toroid Veto.* The reading from the electron toroid at the exiting end of SLD must be at least 45 counts. Pedestal is usually 20 counts and full SLC beam running is 300–800 counts.

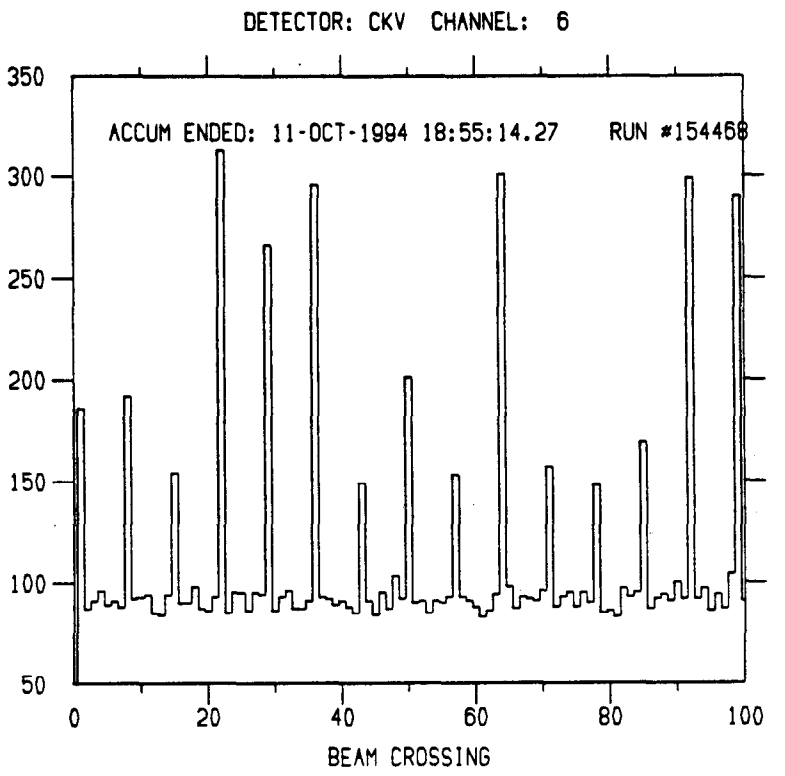

Figure B.2: Raw signal observed in Channel 6 of the Cherenkov detector during clean running.

- *Electron Dumper Veto.* One of the bits from the register in the mezzanine informs the Compton acquisition if the electron beam has been intentionally dumpered in the BSY. This veto is redundant and weaker than the electron toroid veto.

- *Positron Toroid Veto* The reading from the positron toroid after the SLD IP should be in excess of 100 counts. The nominal range of positron current readings are the same as for the electrons.

- *Excessive Noise Veto* This veto compares the signal in Cherenkov channel # 9 against 1000 counts out of a possible 2048, with a pedestal of $\sim$ 30 counts. Channel # 9 lies off the kinematic endpoint for Compton scattering, and thus measures predominantly accelerator backgrounds with almost no bias for the

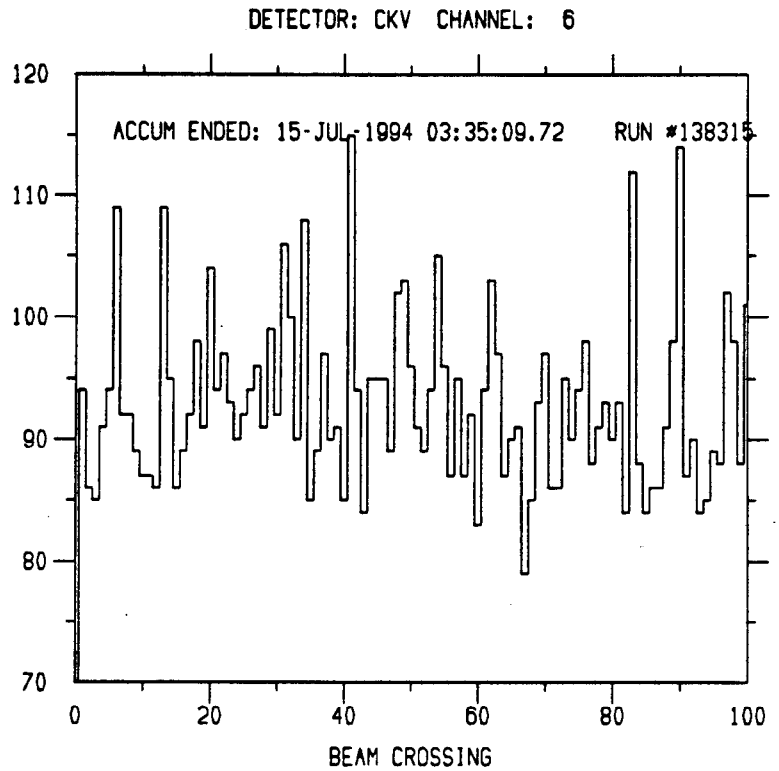

Figure B.3: Raw signal observed in Channel 6 of the Cherenkov detector during dirty running. This particular run had a smaller signal level, contributing to the lack of statistical accuracy on the measurement.

asymmetry measurement. If the other channels saturate, then linearity may be compromised, and the asymmetry affected.

After the requisite number of beam crossings' worth of data has been accumulated. the polarization is calculated and distributed, with its statistical error, to the SLD database, the SLC database, and the SLD status display. In order to be written to the SLC database, the polarization must have a statistical error of ¡5%, as well as having the detector controls set to their nominal positions.

The polarization of the laser light on the optics bench and in the analysis box in the tunnel are also calculated, as are signal ratios in the different channels of the detector. These are all written to the SLD database. The SLD time history process periodically fetches the values from the database and forms a running history. The polarization

Table B.1: Contents of the raw Compton polarimeter data structure. These can be found in QR94A.TEMPLATE.

Item	Quantity	Item Size	Size (bytes/beam crossing)
Status Word	1	4	4
Toroids	4	2	16
Polarity Registers	2	2	4
Time Digitizers	4	2	8
Spare Channels	5	2	10
PTD Detector Channels	16	2	32
XYZ Polarimeter Channels	12	2	24
Cherenkov Channels	9	2	18
PMON Information	2	2	4
Laser Photodiodes	15	2	30
Beamsstrahlung Monitor	1	2	2
Total			152

written to the SLD database has to meet the same criteria as those written to the SLC database, although time histories are kept of unfiltered polarization measurements. Often, the electron beam will be shut off in the middle of a Compton measurement. If so, the polarization may be poorly determined and cause a large scatter on a history plot.

A number of quantities are read out of the SLC database regarding the most recent beam-beam deflection scan, collimator settings, source quantum efficiency, and related quantities. These are stored in a QS94A bank, along with the Compton channel averages and RMS's (really sums and summed squares, but information enough to reconstruct the asymmetries and their errors). Time history is not performed for quantities read out of the SLC database, because the SLC time history can be used instead.

The QS94A bank also contains a small amount of raw data at its end. It carries 100 consecutive beam crossings in the same format as QR94A. The consecutive beam crossings are important for offline studies of the random number sequence. The QS94A bank is written to SLD acquisition tape after each Compton measurement, roughly every 3 minutes. The filter job which runs at the end of each SLD run strips the QS94A banks off separately and writes them to files listed in POL.DATACAT.

B.4 Scans

The first scans implemented for the polarimeter were put in place to enable the targeting of the laser beam on the SLC electron beam to be optimized. These involved scanning the position of the steering lens in the laser transport line, and scanning the timing offset of the laser Q-switch relative to the electron timing signal from SLC. Because of the finite crossing angle of the two beams, these two parameters provide enough degrees of freedom to target the beams, although the timing scan also involved moving the effective Compton IP along the beam axis.

Scans consist of repeatedly taking short runs and changing motors and power supply voltages. The datataking is the same as it is in normal acquisition, except the runs are shorter, the polarization is not calculated, the database writes are disabled, and logging is disabled. The results of the scans are stored in separate buffers for viewing by the SCPs. Targeting scans needed only to retain average signal-background information.

Other scans became necessary as the required precision from the polarimeter increased. The most important of these are the Pockels cell scans. Two varieties were implemented. The first is a quick scan, much like the targeting scans, where short runs were taken at each of many voltages on the Pockels cells. The statistics retained for these measurements were the laser polarizations on the laser bench and in the analysis box.

The second type involved scanning over the voltages slowly and recording the asymmetry of Compton scattering at each voltage point. Because the necessary time to accumulate enough data to make the measurements significant is large, this scan

had to be interleaved with nominal data-taking. A typical scan would take roughly one hour.

Other scans were implemented later. Slow scans over phototube voltage and detector table positions provide valuable information about detector linearity and position calibration.

Appendix C

CDC Vector Hit Finder

C.1 The need for Vector Hits

One of the first tasks the SLD reconstruction is faced with is to find the paths of charged tracks in the Central Drift Chamber (CDC). After being fit to helices, these are used directly in analyses, and they are extrapolated both inwards to the Vertex Detector and outward to the CRID and LAC. Ideally, a full fit over all possible combinations of hits in the CDC that maximizes the number and length of tracks found, and minimizes the chisquared of the combined fit, would produce an optimal set of found and fit charged tracks in the chamber. The SLD track fitter is elaborate, though, invoking the general swimmer to take into account multiple scattering and energy loss, and involves the inversion of large matrices at each step of a track fit.

A more efficient solution is to use simpler fitting techniques that can scan over possible combinations of hits quickly and select the best set, which can then be passed to the fitter. This is the approach taken by the SLD pattern recognition. Even this stage, though, would be too cumbersome unless some preprocessing and grouping of locally related hits were not performed.

A natural division of the problem of finding the charged tracks in an event is to divide the hits first into groups by superlayer. Most tracks pass through each superlayer only once, and tracks that bend around in the magnetic field to traverse a superlayer a second time do so at a location distant from the first traversal. Each

superlayer consists of eight layers of wires, so each track should leave eight hits in each superlayer it traverses. The wires are spaced by 0.5 cm radially, so the hits from a single track lie nearly on a straight line. The sagitta for a 1 GeV track across a superlayer is $\simeq 36\ \mu$m. By grouping hits, eight at a time (or fewer if they are not all present) into small line segments and allowing the pattern-recognition algorithm use higher-level objects in its search, a large savings in reconstruction effort is effected.

The goals of the vector hit finder, and of the pattern recognition itself, are listed below.

- Maximum efficiency for finding tracks and track segments.
- Maximum purity of the found tracks and segments. Finding background tracks is acceptable and desirable, as long as real tracks are not composed partially of background hits.
- Minimum bias for physics analyses.

The vector hit finder is mainly concerned with the first and second items, as they affect the track-finding efficiency. A perfectly efficient and pure track-finding algorithm will also introduce no more bias for physics than is already present in the chamber.

C.2 Algorithm

The vector hit (VH) finder breaks the pattern recognition problem down one step further by searching for track segments one cell at a time. A very small fraction of tracks cross cell boundaries, and many of those that do contribute at least one VH in their layer anyway. The VH finder first finds the drift distance and charge-division z position of each hit in the cell, and arranges them by wire number. Ambiguity partners are listed separately with opposite drift distances*.

*Two common strategies for drift chamber design would help break the drift distance sign ambiguity — staggering the wires and orienting the cells so that the sense wire plane does not contain the electron beam. Neither option was chosen for SLD, although the high spatial resolution partially compensates at the pattern recognition stage.

Because the VH finder is looking for line segments, it seeks first the endpoints, because they provide the most reliable information about the position and direction of the line segment. The search for endpoints starts with the first and last wires in the cell. If a VH cannot be found with endpoints in the first and last layers, combinations of the first and next-to-last layers are tried. Then second and last. Then second and next-to-last, and so forth until the allowed possibilities are exhausted.

A line is drawn between candidate endpoints, and hits on the intervening wires are assigned to the line segment if they are close enough. The criterion is that

$$|d_{hit} - d_{line}|/\sigma_{hit} < \sigma_0, \tag{C.1}$$

where d_{hit} is the signed drift distance from the hit to the wire, d_{line} is the expected drift distance if the hit were to lie on a line segment containing the two endpoints. σ_{hit} is the drift distance error, and σ_0 is and adjustable parameter of the algorithm, set loosely at 6.0 for the time being. If two hits on a single intervening wire are close enough to the line segment to be added, the closer is chosen.

A list of added hits and their

$$\chi^2 = \sum_{addedhits} (d_{hit} - d_{line})^2/\sigma_{hit}^2 \tag{C.2}$$

is kept for comparison with other combinations. In addition to trying a straight line segment as a road, a parabolic approximation to a circular segment is also tried to find a set of hits which minimizes the total χ^2. The circle used is the one that goes through the two candidate endpoints and the SLD IP. Given the small sagitta for real physics tracks, this additional search provides little discrimination. Very low momentum loopers in the first few layers, mostly the result of synchrotron-induced Compton scatters and beam-wall interactions, however, have noticeable curvature.

The algorithm searches over all combinations of pairs of candidate endpoints and selects the one with the most added intervening hits as a VH. In the case of a tie, the VH candidate with the smallest χ^2 is chosen. If no combination has

$$n_{hits} \geq n_{hits,min}, \tag{C.3}$$

where $n_{hits,min}$ is another adjustable parameter, set at 4 hits, then a different pair of wires is chosen to search for candidate endpoints.

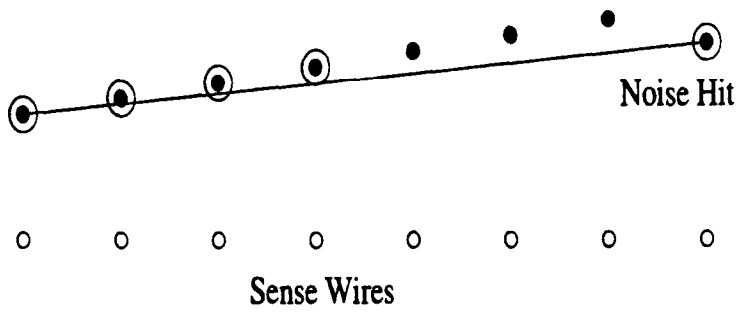

Figure C.1: A vector hit with a noise hit replacing one of the true endpoints.

Because the algorithm uses the endpoints as the seed for VH combinations, it must return and check to see if its seeds are appropriate for the found VH. Once the best combination of hits is found for a given pair of candidate endpoint wires, its hits are fit to a straight line and its χ^2 is found. At this point, one of the endpoints is dropped, the remaining hits are fit to a straight line, and the remaining wires that did not contribute hits are scanned for hits that now may lie on the new line segment. If the VH can benefit from dropping one of its endpoints by adding at least one extra hit with a lower chisquared, or by adding more than one extra hit, then the new combination is accepted. The other endpoint is also removed and tested.

The reason for doing this is that if the real endpoint hit were missing from the chamber, and a noise hit were to take its place, then the line segment between a real endpoint hit and the noise one will come in the vicinity of only a fraction of the intervening hits, as diagrammed in Figure C.1. By omitting the endpoint and refitting, more hits may be added and a more accurate vector hit found. If two hits on the end of a VH are noise hits, then the situation is not resolved. In fact, it quickly becomes impossible to distinguish from a real track a string of noise hits that lie on a straight line.

Once a VH is found, its hits are marked as used, and the VH is fit to a line segment and given an absolute position in space given the CDC wire map. The ambiguity partners of each hit are also marked as used and fit separately for a line segment themselves. Because the drift model incorporates a Lorentz angle correction, the ambiguity partners must be fit separately.

The z coordinate of a VH is an interesting problem, because the charge division resolution is ~6 cm per hit with a long, non-Gaussian tail. The goal is to arrive at a robust averaging procedure for the charge-division z measurements for each hit on the VH. The previous VH finder's algorithm was to omit the largest z and the smallest z and to average the rest. It was found that often the VH finder would group hits with two on one end of the wire, and six on the other end. It is therefore more reliable to find clusters of z measurements and to average those.

The algorithm used is simple. For each hit in the VH, a count of how many hits have z measurements within z_{cut} of the hit is made. The parameter z_{cut} is adjustable and is currently set to 6 cm. The hit with the maximum number of nearby hits is then used to construct a list of close measurements. The hits on that list contribute their z measurements to the average. If no hit has another hit with a z measurement within z_{cut} of its z measurement, then the VH is claimed to have no z information. Further, if no hits within the VH have reliable charge-division z measurements, usually due to failed electronics on one end of the chamber, then that VH is also labeled as having no z information. If a VH lacks z information, it is reported as located in the middle of the detector and flagged appropriately.

In addition to finding the average z position of the VH, a dip angle is fit using the charge division information. This dip angle suffers from a large error owing to the measurement error on the z of each hit.

C.3 Performance

The efficiency of the VH finder, defined in the Monte Carlo to be the probability a VH with a plurality of hits from the Monte Carlo track being investigated is found. The probability is averaged over all Monte Carlo tracks and all layers which the Monte Carlo tracks traverse. This efficiency is found to be ~91% in hadronic Z^0 events, largely independent of layer and track momentum, but with worse efficiency as the track $|\cos\theta|$ increases. When it is required that the Monte Carlo track deposit at least 4 hits in the layer in question, the efficiency rises to ~98%, with a smaller drop to ~95% with increasing $|\cos\theta|$.

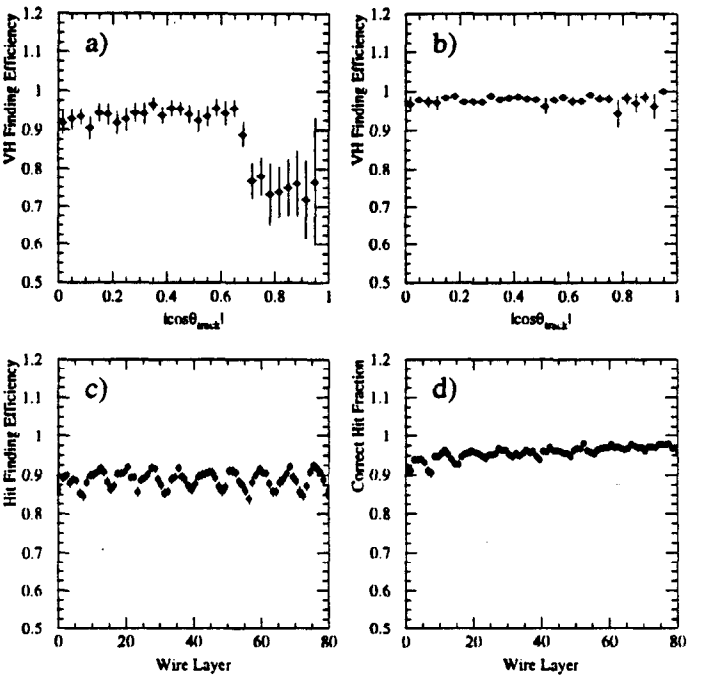

Figure C.2: Performance of the CDC Vector Hit (VH) finder. The probability of finding a VH in a cell where a Monte Carlo track passes is given in Figure a. Figure b shows the same probability if the track is required to have four or more hits in the layer where the VH is sought. Figure c shows the hit finding efficiency as a function of wire layer number for found VH's. Structure is seen due to tracks which cross cells and hit loss on the ends of cells. Figure d shows the correct-hit fraction as a function of wire layer.

It is estimated that the losses in efficiency of the VH finder are largely due to correlated hit loss in the CDC. For a track that passes too close to the plane of field wires between cells, each hit can be lost in the dead region. The same is true for a second track which passes through a cell close to another track and also parallel to it. The two-hit resolution as shown in Figure 4.9 indicates that two tracks which pass within 1 mm of each other will reduce the efficiency of finding the second track's hits. The effect is doubled by the ambiguity of the two halves of a cell. A track will induce two dead regions in a cell — one on its side, and one for its reflection across the sense wire plane. The impact of both of these efficiency losses would be reduced by

Table C.1: Percentages of found Vector Hits, listed by the number of total hits and the number of correct hits, indicating the purities of Vector Hits with different lengths.

	Correct Hits							
Total Hits	1	2	3	4	5	6	7	8
8	0.0	0.0	0.2	0.6	0.9	1.7	4.7	47.2
7	0.0	0.0	0.2	0.7	0.7	2.1	17.6	
6	0.0	0.0	0.4	0.6	1.0	7.3		
5	0.0	0.3	0.8	1.1	5.0			
4	0.2	1.0	1.2	4.5				

"tilting" the cells — arranging the sense and field wire planes so they do not contain the electron beam line. Tilted cells have inefficiencies in the corners, though, but it is less likely to lose all hits in a layer when the geometry is non-projective. Tilted cells would also reduce the impact ambiguity partners have on the pattern recognition stage in dense jets.

One shortcoming of the VH finder as it stands is that it makes no special attempt to find VH's which cross the field wire plane into another cell. Were this feature to be added, a small fraction (<5%, and then largely for low-momentum tracks which curve enough to point non-projectively) of the VH's would have their ambiguity removed. The hit-finding efficiency at the ends of the cells is reduced because a fraction of tracks leave the cell near the ends.

The composition of the vector hits is summarized in Table C.1. These are given for a sample of hadronic Monte Carlo events with full simulation and background addition. A hit on a VH which does not come from the track contributing the plurality of hits is counted as a contamination hit. Hits from background, other tracks, and ambiguity partners of correct hits are examples of contamination. The contamination fraction increases as the number of hits present in the VH falls. Missing hits reduce the purity because long VH's are preferred over short ones and the VH finder will look farther to find a hit to add.

Appendix D

Trigger and Filter

D.1 Trigger

The SLD trigger has several independent components: an energy trigger using the LAC, a tracking trigger which forms candidate track hypotheses in the CDC, a Bhabha trigger using information from the luminosity monitor, and several combinations using information from multiple sources. In addition, there is a "random" trigger, which periodically reads out the entire detector regardless of its contents, and is used for the background overlay events mentioned in Chapter 5. The trigger types are described in detail in Table D.1.

In addition to the requirements a beam crossing must pass in order for a trigger to fire, there are additional requirements it must pass in order for the readout not to be vetoed. Due to the variable noise environment of SLC, it is important not to read out the detector on a beam crossing in which either beam's bunch has a problem serious enough to cause beam loss close to the detector and fill all of the channels with muons and/or synchrotron radiation. Such an event can be called a "beam splash" event, or a "flyer." Flyers can be a significant source of deadtime when they are frequent, as it takes longer to read out SLD when its occupancy is high. Table D.1 describes these veto conditions.

In 1993, the CDC Cell overflow veto, $N_{CDCcell} \geq 275$ was applied to the Hadron as well as the track trigger, and the Energy trigger only read out the calorimetric

Table D.1: Description of the SLD triggers.

Name	Condition	Prescale	Veto	Readout
Random	any crossing	1 in 2400±50	none	SLD
Energy	KAL_{hi} ≥12 GeV	none	$N_{KAL,lo} \geq 1000$	SLD
Bhabha	Back-to-Back Octants in LUM≥12 GeV	none	none	KAL
Track	≥2 Tracks, Back-to-Back	none	$N_{CDC\ cell}$ ≥275	SLD
Hadron	≥1 Track & KAL_{hi} ≥4 GeV	none	none	SLD
WAB	KAL_{hi}(EM only)≥30 GeV	none	$N_{KAL,lo} \geq 1000$	SLD
Muon	≥1 Track & WIC CLU	≤5 in 12000	$N_{KAL,lo} \geq 1000$	SLD
ELUMMON	LUM_N & $LUM_S \geq 10$ GeV	1/100	none	KAL
Cyclic	any crossing	2/120	none	SLD

Table D.2: LAC layer thresholds and online energy conversions.

Layer	High Threshold	Low Threshold	MeV/Count
EM1 and EM2	60	8	4.09
HAD1 and HAD2	120	12	10.81

subsystems of SLD (LAC, WIC Pads, and the LUM). During the "veto period," described in Section 6.2.2, the threshold on the cell count was inappropriately set for the then current definition of how many cells had been hit*.

The terms used in Table D.1 are defined as follows:

KAL_{hi} is the sum of energy in towers in the LAC above the high threshold. The thresholds and energy scales are described below in Section D.2.1.

KAL_{lo} is the sum of energy in towers in the LAC above the low threshold The thresholds and energy scales are described below in Section D.2.1.

$N_{KAL,hi}$ is the number of towers contributing to the KAL_{hi} energy sum.

$N_{KAL,lo}$ is the number of towers contributing to the KAL_{lo} energy sum.

*The cell count was derived from the tracking trigger, which counts nonexistent hardware cells which correspond to the ends of short CDC motherboards as always being hit. A mistally of these put the wrong offset into the CDC hit cell count and the veto threshold was not changed

LUM_N and LUM_S are the energies deposited in the North and South LUM detectors, respectively.

WIC CLU is the WIC coincidence module, which seeks sets of layers of hits in the WIC. Can be configured to require coincidence of two octants to form a cosmic ray trigger.

The Prescale counts beam crossings after a particular trigger has caused the detector to read out. While the counter is counting its fixed number of beam crossings, that trigger cannot cause another readout. It is built-in deadtime. The Random trigger has a special prescale which randomly jitters the beam crossing to be read out by ±50 beam crossings. This is done so as not to lock the random trigger readout to a particular phase of any periodic behavior of SLC.

D.2 Z Filters

The second stage of event selection is common to all analyses at SLD – the first pass through the raw data with a loose set of event selection criteria. These are designed to select Z^0 decay events with maximum efficiency, while reducing the number of background triggers passed to the reconstruction and analysis stages. Analyses later apply more restrictive requirements to obtain samples more pure in the decays of interest. There are several filters applied, and if an event passes any one of them, it is included in the filtered data sample available for all SLD experimenters. These consist of: 1) two calorimetric filters, (EIT and KZ0F); 2) a first-pass tau filter; and 3) a mu-pair filter. In addition, extra sets are filtered off into non-Z^0 samples: luminosity monitor data, 120 Hz data, random triggers, and Compton polarimeter data.

D.2.1 The EIT Calorimetric Filter

The EIT filter [144] starts with the subsample of events that pass the energy trigger and imposes stricter requirements:

$$NEMHI \geq 10 \tag{D.1}$$

$$EHI > 15 \text{ GeV} \tag{D.2}$$

$$ELO < 140 \text{ GeV} \tag{D.3}$$

$$EHI > 1.5 * (ELO - 70), \tag{D.4}$$

where NEMHI is the number of EM towers passing the high threshold, EHI is the total summed energy in the EM and HAD sections for towers passing the high threshold, and ELO is the same sum, but for towers passing the low thresholds. The thresholds and energy scales are defined in Table D.2. The efficiency of this selection has been checked in the sample passed by the KZ0F filter and found to be 97.2% efficient for events also passing KZ0F. Its efficiency is estimated at 96% using the SLD Monte Carlo simulation. The combined trigger and EIT filter efficiency is estimated to be ~93% [143].

Because the EIT filter is a strict subset of the trigger and a strict subset of the filtered events, and because it is simulated in the Monte Carlo, this analysis requires that events pass the EIT selection in both data and Monte Carlo. If any trigger/filter bias is present, this technique ensures that it is modeled. The inefficiency of the EIT filter for hadronic Z^0 decay is only 1.8% within the analysis acceptance, as defined by selection cuts described below, and for tagged events it is also 1.8%. The filter is unlikely to introduce biases to the asymmetry analysis because efficiency effects cancel in the asymmetry ratio.

D.2.2 Additional Filters: Tau, Mu Pair, and KZ0F

Additional filters are applied during PASS1 reconstruction of events in order to provide data samples for analyses needing two-prong dilepton events and tau events. These filters by construction pass only events that fail the event selection cuts described in the next section, so they will not be discussed in detail. The KZ0F calorimetric sample is also highly correlated with the EIT sample, and allowing events which pass it and not EIT into the analysis increases the size of the event sample by 2%. Its use is not included in this analysis.

Appendix E

Monte Carlo Charm Decays

Listed in this Appendix are the decay tables for the D^0, $D^{\pm}$, D_s, and D^* mesons and the Λ_c^+ baryon, as adjusted by Su Dong [129], in order to match better with available data from CLEO, ARGUS, and MARK III. Branching fractions are reported here normalized to unity, to match the implementation in JETSET 7.4.

Table E.1: SLD decay table for the D^{*+} meson.

Mode	Branching Fraction
$D^{*+} \to D^0\pi^+$	0.68100
$D^{*+} \to D^+\pi^0$	0.30800
$D^{*+} \to D^+\gamma$	0.01100

Table E.2: SLD decay table for the D^{*0} meson.

Mode	Branching Fraction
$D^{*0} \to D^0\pi^0$	0.63600
$D^{*0} \to D^0\gamma$	0.36400

Table E.3: SLD decay table for the D^0 meson.

Mode	Branching Fraction	Mode	Branching Fraction
$D^0 \to K^-\pi^+$	0.04000	$D^0 \to \pi^0\pi^0\pi^0\overline{K}^0$	0.01500
$D^0 \to \pi^0\overline{K}^0$	0.02100	$D^0 \to \overline{K}^0\pi^-\pi^+\pi^-\pi^+$	0.00850
$D^0 \to K^-K^+$	0.00410	$D^0 \to \pi^0\pi^0\overline{K}^0\pi^-\pi^+$	0.04000
$D^0 \to \overline{K}^0K^0$	0.00110	$D^0 \to K^-\pi^-\pi^-\pi^+\pi^+\pi^+$	0.00500
$D^0 \to \pi^-\pi^+$	0.00163	$D^0 \to \overline{K}^0K^+K^-$	0.00520
$D^0 \to \pi^0\pi^0$	0.00013	$D^0 \to \pi^0\overline{K}^0K^+K^-$	0.00900
$D^0 \to \eta\overline{K}^0$	0.01520	$D^0 \to \phi\pi^-\pi^+$	0.00240
$D^0 \to \eta\pi^0$	0.00008	$D^0 \to K^+K^-\pi^+\pi^-$	0.00007
$D^0 \to \eta\eta$	0.00016	$D^0 \to K^0K^-\pi^+$	0.00220
$D^0 \to \eta'\overline{K}^0$	0.01700	$D^0 \to \pi^0\pi^+\pi^-$	0.01500
$D^0 \to \eta'\pi^0$	0.00004	$D^0 \to \pi^0\pi^-\pi^-\pi^+\pi^+$	0.01700
$D^0 \to \rho^+K^-$	0.09000	$D^0 \to \pi^0\pi^0K^-\pi^-\pi^+\pi^+$	0.01200
$D^0 \to \rho^0\overline{K}^0$	0.00610	$D^0 \to \pi^0K^-\pi^-\pi^+\pi^+$	0.03500
$D^0 \to \phi\overline{K}^0$	0.00880	$D^0 \to \pi^0\pi^0\pi^0K^-\pi^+$	0.01000
$D^0 \to K^{*-}\pi^+$	0.04500	$D^0 \to \rho^0K^-\pi^+$	0.00630
$D^0 \to K^{*0}\pi^0$	0.02100	$D^0 \to \overline{K}^{*0}\pi^+\pi^-$	0.01600
$D^0 \to \phi\pi^0$	0.00026	$D^0 \to \overline{K}^{*0}\pi^0\pi^+\pi^-$	0.01600
$D^0 \to \omega\overline{K}^0$	0.02500	$D^0 \to \pi^0K^-K^+\pi^+\pi^-$	0.00280
$D^0 \to K^{*-}K^+$	0.00200	$D^0 \to e^+\nu_eK^-$	0.03500
$D^0 \to K^{*+}K^-$	0.00350	$D^0 \to e^+\nu_eK^{*-}$	0.02500
$D^0 \to K^{*-}\rho^+$	0.06200	$D^0 \to e^+\nu_e\overline{K}^0\pi^-$	0.00200
$D^0 \to K^-a_1^+$	0.07400	$D^0 \to e^+\nu_eK^-\pi^0$	0.00200
$D^0 \to K_1^-\pi^+$	0.01090	$D^0 \to e^+\nu_e\overline{K}^{*0}\pi^-$	0.00400
$D^0 \to \overline{K}^0a_1^0$	0.00420	$D^0 \to e^+\nu_eK^{*-}\pi^0$	0.00400
$D^0 \to \overline{K}_1^{*0}\pi^0$	0.00820	$D^0 \to e^+\nu_e\pi^-$	0.00300
$D^0 \to \rho^0\overline{K}^{*0}$	0.01500	$D^0 \to e^+\nu_e\rho^-$	0.00200
$D^0 \to \overline{K}^{*0}\eta$	0.02100	$D^0 \to \mu^+\nu_\mu K^-$	0.03500
$D^0 \to \overline{K}^{*0}K^{*0}$	0.00270	$D^0 \to \mu^+\nu_\mu K^{*-}$	0.02500
$D^0 \to \pi^0K^-\pi^+$	0.01100	$D^0 \to \mu^+\nu_\mu\overline{K}^0\pi^-$	0.00200
$D^0 \to \overline{K}^0\pi^-\pi^+$	0.01800	$D^0 \to \mu^+\nu_\mu K^-\pi^0$	0.00200
$D^0 \to \pi^0\pi^0\overline{K}^0$	0.01200	$D^0 \to \mu^+\nu_\mu\overline{K}^{*0}\pi^-$	0.00400
$D^0 \to K^-\pi^-\pi^+\pi^+$	0.01800	$D^0 \to \mu^+\nu_\mu K^{*-}\pi^0$	0.00400
$D^0 \to \pi^0\pi^0K^-\pi^+$	0.04000	$D^0 \to \mu^+\nu_\mu\pi^-$	0.00300
$D^0 \to \pi^+\pi^-\pi^-\pi^+$	0.00750	$D^0 \to \mu^+\nu_\mu\rho^-$	0.00200
$D^0 \to \pi^0\overline{K}^0\pi^-\pi^+$	0.02200		

Table E.4: SLD decay table for the D^+ meson.

Mode	Branching Fraction	Mode	Branching Fraction
$D^+ \to \overline{K}^0\pi^+$	0.02455	$D^+ \to \rho^+K^-\pi^+$	0.00755
$D^+ \to \overline{K}^0K^+$	0.00689	$D^+ \to \rho^+\pi^0K^0$	0.00755
$D^+ \to \pi^0\pi^+$	0.00283	$D^+ \to \overline{K}^{*0}\pi^-\pi^+\pi^+$	0.00718
$D^+ \to \eta\pi^+$	0.00623	$D^+ \to \pi^0K^-K^+\pi^+$	0.01416
$D^+ \to \eta'\pi^+$	0.00378	$D^+ \to \rho^0\overline{K}^{*0}\pi^+$	0.00538
$D^+ \to \overline{K}^{*0}\pi^+$	0.01794	$D^+ \to \pi^0\pi^+\pi^-\pi^+$	0.01605
$D^+ \to \rho^+\overline{K}^0$	0.06231	$D^+ \to \pi^+\pi^-\pi^+\pi^-\pi^+$	0.00142
$D^+ \to \phi\pi^+$	0.00566	$D^+ \to \pi^0\pi^-\pi^-\pi^+\pi^+\pi^+$	0.00264
$D^+ \to \overline{K}^{*0}K^+$	0.00444	$D^+ \to e^+\nu_e\overline{K}^0$	0.07553
$D^+ \to \overline{K}^{*0}K^{*+}$	0.02455	$D^+ \to e^+\nu_e\overline{K}^{*0}$	0.05287
$D^+ \to \rho^+\pi^0$	0.00566	$D^+ \to e^+\nu_e\overline{K}^0\pi^0$	0.00566
$D^+ \to \rho^+\eta$	0.00566	$D^+ \to e^+\nu_eK^-\pi^+$	0.00566
$D^+ \to \rho^+\eta'$	0.00378	$D^+ \to e^+\nu_e\overline{K}^{*0}\pi^0$	0.01039
$D^+ \to \overline{K}^{*0}\rho^+$	0.01983	$D^+ \to e^+\nu_eK^{*-}\pi^+$	0.01039
$D^+ \to \overline{K}^0a_1^+$	0.07081	$D^+ \to e^+\nu_e\pi^0$	0.00566
$D^+ \to \overline{K}_1^{*0}\pi^+$	0.04154	$D^+ \to e^+\nu_e\eta$	0.00094
$D^+ \to K^-\pi^+\pi^+$	0.07175	$D^+ \to e^+\nu_e\eta'$	0.00094
$D^+ \to \pi^0\overline{K}^{*0}\pi^+$	0.01133	$D^+ \to e^+\nu_e\rho^0$	0.00189
$D^+ \to K^+K^-\pi^+$	0.00378	$D^+ \to e^+\nu_e\omega$	0.00094
$D^+ \to \overline{K}^0\overline{K}^0K^+$	0.02549	$D^+ \to \mu^+\nu_\mu\overline{K}^0$	0.07553
$D^+ \to \phi\pi^0\pi^+$	0.02266	$D^+ \to \mu^+\nu_\mu\overline{K}^{*0}$	0.05287
$D^+ \to \pi^+\pi^-\pi^+$	0.00264	$D^+ \to \mu^+\nu_\mu\overline{K}^0\pi^0$	0.00566
$D^+ \to \pi^0\pi^0\pi^+$	0.01048	$D^+ \to \mu^+\nu_\mu K^-\pi^+$	0.00566
$D^+ \to \overline{K}^0\pi^-\pi^+\pi^+$	0.00755	$D^+ \to \mu^+\nu_\mu\overline{K}^{*0}\pi^0$	0.01039
$D^+ \to \pi^0K^-\pi^+\pi^+$	0.00850	$D^+ \to \mu^+\nu_\mu K^{*-}\pi^+$	0.01039
$D^+ \to \pi^0\pi^0\overline{K}^0\pi^+$	0.01888	$D^+ \to \mu^+\nu_\mu\pi^0$	0.00566
$D^+ \to K^-\pi^-\pi^+\pi^+\pi^+$	0.00576	$D^+ \to \mu^+\nu_\mu\eta$	0.00094
$D^+ \to \overline{K}^0\pi^-\pi^+\pi^-\pi^+\pi^+$	0.00094	$D^+ \to \mu^+\nu_\mu\eta'$	0.00094
$D^+ \to \pi^0\pi^0K^-\pi^+\pi^+$	0.02077	$D^+ \to \mu^+\nu_\mu\rho^0$	0.00189
$D^+ \to \pi^0\overline{K}^0\pi^-\pi^+\pi^+$	0.05098	$D^+ \to \mu^+\nu_\mu\omega$	0.00094
$D^+ \to \pi^0\pi^0\pi^0\overline{K}^0\pi^+$	0.02832		

Table E.5: SLD decay table for the D_s^+ meson, Part 1.

Mode	Branching Fraction	Mode	Branching Fraction
$D_s^+ \to \eta\pi^+$	0.01349	$D_s^+ \to K^{*-}K^+\pi^+$	0.00682
$D_s^+ \to \eta'\pi^+$	0.03328	$D_s^+ \to K^{*+}K^-\pi^+$	0.00682
$D_s^+ \to K^0\pi^+$	0.00259	$D_s^+ \to \rho^+\overline{K}^0K^0$	0.00189
$D_s^+ \to \overline{K}^0K^+$	0.02519	$D_s^+ \to \rho^+K^-K^+$	0.00203
$D_s^+ \to \pi^0K^+$	0.00040	$D_s^+ \to K^{*0}\overline{K}^0\pi^+$	0.00670
$D_s^+ \to \eta K^+$	0.00020	$D_s^+ \to \overline{K}^{*0}K^0\pi^+$	0.00670
$D_s^+ \to \rho^+\eta$	0.07106	$D_s^+ \to \rho^0\overline{K}^0K^+$	0.00196
$D_s^+ \to \rho^+\eta'$	0.08545	$D_s^+ \to \omega\overline{K}^0K^+$	0.00174
$D_s^+ \to \phi\pi^+$	0.03148	$D_s^+ \to \overline{K}^{*0}\pi^0K^+$	0.00692
$D_s^+ \to \rho^+K^0$	0.00499	$D_s^+ \to K^{*+}\pi^0\overline{K}^0$	0.00679
$D_s^+ \to K^{*0}\pi^+$	0.00143	$D_s^+ \to \rho^0K^0\pi^+$	0.00058
$D_s^+ \to \overline{K}^{*0}K^+$	0.02968	$D_s^+ \to \rho^0\pi^0K^+$	0.00059
$D_s^+ \to K^{*+}\overline{K}^0$	0.02968	$D_s^+ \to \rho^+\pi^0K^0$	0.00058
$D_s^+ \to \omega K^+$	0.00068	$D_s^+ \to \rho^+K^+\pi^-$	0.00058
$D_s^+ \to K^{*+}\pi^0$	0.00023	$D_s^+ \to \rho^-K^+\pi^+$	0.00058
$D_s^+ \to K^{*+}\eta$	0.00067	$D_s^+ \to \omega\pi^0K^+$	0.00057
$D_s^+ \to K^{*+}\eta'$	0.00079	$D_s^+ \to \omega K^0\pi^+$	0.00056
$D_s^+ \to \phi K^+$	0.00001	$D_s^+ \to \phi K^0\pi^+$	0.00017
$D_s^+ \to f_0^0\pi^+$	0.00702	$D_s^+ \to \phi\pi^0K^+$	0.00018
$D_s^+ \to \eta a_1^+$	0.01284	$D_s^+ \to K^{*+}\pi^-\pi^+$	0.00098
$D_s^+ \to K^0a_1^+$	0.00183	$D_s^+ \to K^{*+}\pi^0\pi^0$	0.00099
$D_s^+ \to K^+a_1^0$	0.00026	$D_s^+ \to K^{*+}\overline{K}^0K^0$	0.00002
$D_s^+ \to \phi\rho^+$	0.04677	$D_s^+ \to K^{*+}K^-K^+$	0.00002
$D_s^+ \to K^{*0}\rho^+$	0.00194	$D_s^+ \to K^{*0}\pi^0\pi^+$	0.00099
$D_s^+ \to \overline{K}^{*0}K^{*+}$	0.04498	$D_s^+ \to K^{*0}\overline{K}^0K^+$	0.00002

Table E.6: SLD decay table for the D_s^+ meson, Part 2.

Mode	Branching Fraction	Mode	Branching Fraction
$D_s^+ \to \rho^0 K^{*+}$	0.00029	$D_s^+ \to \overline{K}^{*0} K^0 K^+$	0.00002
$D_s^+ \to \omega K^{*+}$	0.00028	$D_s^+ \to K^{*-} K^+ K^+$	0.00002
$D_s^+ \to \phi K^{*+}$	0.00022	$D_s^+ \to \rho^+ \pi^0 \pi^0$	0.01069
$D_s^+ \to e^+ \nu_e \eta$	0.02788	$D_s^+ \to \omega \pi^0 \pi^+$	0.01032
$D_s^+ \to e^+ \nu_e \eta'$	0.03328	$D_s^+ \to \rho^0 \pi^0 \pi^+$	0.01062
$D_s^+ \to e^+ \nu_e \phi$	0.01799	$D_s^+ \to \rho^+ \pi^- \pi^+$	0.01056
$D_s^+ \to e^+ \nu_e K^0$	0.00180	$D_s^+ \to \rho^- \pi^+ \pi^+$	0.01056
$D_s^+ \to e^+ \nu_e K^{*0}$	0.00180	$D_s^+ \to \phi \pi^+ \pi^- \pi^+$	0.01079
$D_s^+ \to \mu^+ \nu_\mu \eta$	0.02788	$D_s^+ \to \eta \pi^+ \pi^- \pi^+$	0.02008
$D_s^+ \to \mu^+ \nu_\mu \eta'$	0.03328	$D_s^+ \to \eta' \pi^+ \pi^- \pi^+$	0.02008
$D_s^+ \to \mu^+ \nu_\mu \phi$	0.01799	$D_s^+ \to \phi \pi^0 \pi^0 \pi^+$	0.02008
$D_s^+ \to \mu^+ \nu_\mu K^0$	0.00180	$D_s^+ \to \eta \pi^0 \pi^0 \pi^+$	0.02008
$D_s^+ \to \mu^+ \nu_\mu K^{*0}$	0.00180	$D_s^+ \to \eta' \pi^0 \pi^0 \pi^+$	0.02008
$D_s^+ \to \nu_\tau \tau^+$	0.01799	$D_s^+ \to \overline{K}^0 K^+ \pi^+ \pi^-$	0.01101
$D_s^+ \to K^+ K^- \pi^+$	0.00729	$D_s^+ \to \pi^0 \pi^0 \overline{K}^0 K^+$	0.01101
$D_s^+ \to K^0 \overline{K}^0 \pi^+$	0.00816	$D_s^+ \to \phi \pi^0 \pi^+ \pi^- \pi^+$	0.00680
$D_s^+ \to \pi^0 \overline{K}^0 K^+$	0.00828	$D_s^+ \to \eta \pi^0 \pi^+ \pi^- \pi^+$	0.01004
$D_s^+ \to \eta \overline{K}^0 K^+$	0.00268	$D_s^+ \to \eta' \pi^0 \pi^+ \pi^- \pi^+$	0.01004
$D_s^+ \to \pi^0 K^0 \pi^+$	0.00076	$D_s^+ \to \phi \pi^0 \pi^0 \pi^0 \pi^+$	0.00680
$D_s^+ \to K^+ \pi^- \pi^+$	0.00126	$D_s^+ \to \eta \pi^0 \pi^0 \pi^0 \pi^+$	0.01004
$D_s^+ \to \pi^0 \pi^0 K^+$	0.00076	$D_s^+ \to \eta' \pi^0 \pi^0 \pi^0 \pi^+$	0.01004
$D_s^+ \to K^0 \overline{K}^0 K^+$	0.00017	$D_s^+ \to \pi^0 \overline{K}^0 K^+ \pi^+ \pi^-$	0.00550
$D_s^+ \to K^+ K^+ K^-$	0.00018	$D_s^+ \to \pi^0 \pi^0 \pi^0 \overline{K}^0 K^+$	0.00550
$D_s^+ \to \pi^0 \pi^0 \pi^+$	0.00919	$D_s^+ \to K^+ K^- \pi^- \pi^+ \pi^+$	0.00171
$D_s^+ \to \pi^+ \pi^- \pi^+$	0.00720	$D_s^+ \to \pi^+ \pi^- \pi^+ \pi^- \pi^+$	0.00171
$D_s^+ \to \phi \pi^0 \pi^+$	0.01290		

Table E.7: SLD decay table for the Λ_c^+ baryon, Part 1.

Mode	Branching Fraction	Mode	Branching Fraction
$\Lambda_c^+ \to p\overline{K}^0$	0.02175	$\Lambda_c^+ \to p\overline{K}^0 K^+\pi^-$	0.00104
$\Lambda_c^+ \to \Lambda^0\pi^+$	0.00818	$\Lambda_c^+ \to pK^0K^-\pi^+$	0.00104
$\Lambda_c^+ \to \Sigma^0\pi^+$	0.00901	$\Lambda_c^+ \to p\pi^0\overline{K}^0K^0$	0.00104
$\Lambda_c^+ \to \Sigma^+\pi^0$	0.00311	$\Lambda_c^+ \to \Lambda^0K^+\pi^+\pi^-$	0.00414
$\Lambda_c^+ \to p\pi^0$	0.00155	$\Lambda_c^+ \to \Lambda^0\pi^0\pi^0K^+$	0.00207
$\Lambda_c^+ \to n\pi^+$	0.00311	$\Lambda_c^+ \to \Lambda^0\pi^0K^0\pi^+$	0.00414
$\Lambda_c^+ \to \Sigma^+\eta$	0.00311	$\Lambda_c^+ \to \Sigma^0K^+\pi^+\pi^-$	0.00104
$\Lambda_c^+ \to f_0^0 p$	0.00186	$\Lambda_c^+ \to \Sigma^0\pi^0K^0\pi^+$	0.00104
$\Lambda_c^+ \to p\phi$	0.00135	$\Lambda_c^+ \to \Sigma^+\pi^0K^+\pi^-$	0.00104
$\Lambda_c^+ \to \Delta^{++}K^-$	0.00684	$\Lambda_c^+ \to \Sigma^-\pi^0K^+\pi^+$	0.00104
$\Lambda_c^+ \to pK^-\pi^+$	0.04557	$\Lambda_c^+ \to p\pi^0\pi^0K^-\pi^+$	0.01554
$\Lambda_c^+ \to p\pi^0\overline{K}^0$	0.03314	$\Lambda_c^+ \to pK^-\pi^+\pi^+\pi^-$	0.00073
$\Lambda_c^+ \to n\overline{K}^0\pi^+$	0.04557	$\Lambda_c^+ \to p\pi^-\pi^+\pi^-\pi^+$	0.00124
$\Lambda_c^+ \to \Lambda^0\pi^0\pi^+$	0.01657	$\Lambda_c^+ \to p\pi^0\pi^0\pi^0\overline{K}^0$	0.01554
$\Lambda_c^+ \to \Sigma^0\pi^0\pi^+$	0.01554	$\Lambda_c^+ \to p\pi^0\overline{K}^0\pi^+\pi^-$	0.03107
$\Lambda_c^+ \to \Sigma^+\pi^0\pi^0$	0.01554	$\Lambda_c^+ \to n\pi^0\pi^0\overline{K}^0\pi^+$	0.01554
$\Lambda_c^+ \to \Sigma^+\pi^-\pi^+$	0.03107	$\Lambda_c^+ \to n\overline{K}^0\pi^+\pi^+\pi^-$	0.01554
$\Lambda_c^+ \to \Sigma^-\pi^+\pi^+$	0.01657	$\Lambda_c^+ \to n\pi^0K^-\pi^+\pi^+$	0.01554
$\Lambda_c^+ \to p\pi^-\pi^+$	0.00228	$\Lambda_c^+ \to \Lambda^0\pi^0\pi^0\pi^0\pi^+$	0.02382
$\Lambda_c^+ \to p\pi^0\pi^0$	0.00259	$\Lambda_c^+ \to \Lambda^0\pi^0\pi^-\pi^+\pi^+$	0.04661
$\Lambda_c^+ \to pK^-K^+$	0.00166	$\Lambda_c^+ \to \Sigma^0\pi^0\pi^0\pi^0\pi^+$	0.00621
$\Lambda_c^+ \to p\overline{K}^0K^0$	0.00311	$\Lambda_c^+ \to \Sigma^0\pi^0\pi^-\pi^+\pi^+$	0.01243
$\Lambda_c^+ \to n\pi^0\pi^+$	0.00311	$\Lambda_c^+ \to \Sigma^+\pi^0\pi^0\pi^0\pi^0$	0.00621
$\Lambda_c^+ \to n\overline{K}^0K^+$	0.00259	$\Lambda_c^+ \to \Sigma^+\pi^0\pi^0\pi^-\pi^+$	0.01243

Table E.8: SLD decay table for the Λ_c^+ baryon, Part 2.

Mode	Branching Fraction	Mode	Branching Fraction
$\Lambda_c^+ \to p\eta\overline{K}^0$	0.00725	$\Lambda_c^+ \to \Sigma^+\pi^-\pi^+\pi^-\pi^+$	0.01554
$\Lambda_c^+ \to \Lambda^0\eta\pi^+$	0.00725	$\Lambda_c^+ \to \Sigma^-\pi^0\pi^0\pi^+\pi^+$	0.00621
$\Lambda_c^+ \to \Sigma^0\eta\pi^+$	0.00311	$\Lambda_c^+ \to \Sigma^-\pi^-\pi^+\pi^+\pi^+$	0.01243
$\Lambda_c^+ \to \Sigma^+\eta\pi^0$	0.00311	$\Lambda_c^+ \to \Lambda^0\pi^-\pi^-\pi^+\pi^+\pi^+$	0.00829
$\Lambda_c^+ \to \Xi^- K^+\pi^+$	0.00497	$\Lambda_c^+ \to \Lambda^0\pi^0\pi^0\pi^-\pi^+\pi^+$	0.01657
$\Lambda_c^+ \to p\pi^0 K^-\pi^+$	0.03314	$\Lambda_c^+ \to \Lambda^0\pi^0\pi^0\pi^0\pi^0\pi^+$	0.00829
$\Lambda_c^+ \to p\pi^0\pi^0\overline{K}^0$	0.01657	$\Lambda_c^+ \to \Sigma^0\pi^-\pi^-\pi^+\pi^+\pi^+$	0.00207
$\Lambda_c^+ \to p\overline{K}^0\pi^+\pi^-$	0.01761	$\Lambda_c^+ \to \Sigma^0\pi^0\pi^0\pi^-\pi^+\pi^+$	0.00207
$\Lambda_c^+ \to n\pi^0\overline{K}^0\pi^+$	0.03314	$\Lambda_c^+ \to \Sigma^0\pi^0\pi^0\pi^0\pi^0\pi^+$	0.00207
$\Lambda_c^+ \to nK^-\pi^+\pi^+$	0.03314	$\Lambda_c^+ \to \Sigma^+\pi^0\pi^-\pi^-\pi^+\pi^+$	0.00207
$\Lambda_c^+ \to \Lambda^0\pi^0\pi^0\pi^+$	0.03314	$\Lambda_c^+ \to \Sigma^+\pi^0\pi^0\pi^0\pi^+\pi^-$	0.00207
$\Lambda_c^+ \to \Lambda^0\pi^-\pi^+\pi^+$	0.02796	$\Lambda_c^+ \to \Sigma^+\pi^0\pi^0\pi^0\pi^0\pi^0$	0.00207
$\Lambda_c^+ \to \Sigma^0\pi^0\pi^0\pi^+$	0.00829	$\Lambda_c^+ \to \Sigma^-\pi^0\pi^-\pi^+\pi^+\pi^+$	0.00207
$\Lambda_c^+ \to \Sigma^0\pi^-\pi^+\pi^+$	0.00953	$\Lambda_c^+ \to \Sigma^-\pi^0\pi^0\pi^0\pi^+\pi^+$	0.00207
$\Lambda_c^+ \to \Sigma^+\pi^0\pi^0\pi^0$	0.00829	$\Lambda_c^+ \to e^+\nu_e\Lambda^0$	0.01243
$\Lambda_c^+ \to \Sigma^+\pi^0\pi^-\pi^+$	0.01657	$\Lambda_c^+ \to \mu^+\nu_\mu\Lambda^0$	0.01243
$\Lambda_c^+ \to \Sigma^-\pi^0\pi^+\pi^+$	0.01657	$\Lambda_c^+ \to e^+\nu_e\Sigma^0$	0.00829
$\Lambda_c^+ \to p\eta K^-\pi^+$	0.00414	$\Lambda_c^+ \to \mu^+\nu_\mu\Sigma^0$	0.00829
$\Lambda_c^+ \to n\eta\overline{K}^0\pi^+$	0.00311	$\Lambda_c^+ \to e^+\nu_e\Sigma^0\pi^0$	0.00621
$\Lambda_c^+ \to p\pi^0\pi^-\pi^+$	0.00207	$\Lambda_c^+ \to \mu^+\nu_\mu\Sigma^0\pi^0$	0.00621
$\Lambda_c^+ \to n\pi^0\pi^0\pi^+$	0.00104	$\Lambda_c^+ \to e^+\nu_e pK^-$	0.00932
$\Lambda_c^+ \to n\pi^-\pi^+\pi^+$	0.00207	$\Lambda_c^+ \to \mu^+\nu_\mu pK^-$	0.00932
$\Lambda_c^+ \to n\pi^0\pi^0\pi^+$	0.00104	$\Lambda_c^+ \to e^+\nu_e n\overline{K}^0$	0.00932
$\Lambda_c^+ \to p\pi^0 K^-K^+$	0.00104	$\Lambda_c^+ \to \mu^+\nu_\mu n\overline{K}^0$	0.00932

Bibliography

[1] D. Charlton, *Measurements of R_b with Lifetime Tags*, presented at the Int'l Europhysics Conference on High Energy Physics, Brussels, Jul. 27-Aug. 2, 1995.

[2] W. Pauli, Phys. Rev. **38**, 579 (1931).

[3] T. D. Lee and C. N. Yang, Phys. Rev. **104**, 254 (1956).

[4] C. S. Wu, E. Ambler, R. W. Hayward, D. D. Hoppes, and R. P. Hudson, Phys. Rev. **105**, 1413 (1957).

[5] R. L. Garwin, L. M. Lederman, and M. Weinrich, Phys. Rev. **105**, 1415 (1957).

[6] V. L. Telegdi and J. I. Friedman, Phys. Rev. **105**, 1681 (1957).

[7] C. N. Yang and R. Mills, Phys. Rev. **96**, 191 (1956).

[8] S. Glashow, Nucl. Phys. **22**, 579 (1961).

[9] S. Weinberg, Phys. Rev. Lett. **19**, 1264 (1967).

[10] A. Salam, in *Elementary Particle Theory*, p. 367. ed. N. Svartholm, Almqvist and Wiksell, Stockholm (1968).

[11] P. W. Higgs, Phys. Lett. **12**, 132 (1964); P. W. Higgs, Phys. Rev. Lett. **13**, 508 (1964); Phys. Rev. **145**, 1156 (1966); F. Englert and R. Brout, Phys. Rev. Lett. **13**, 321 (1964); G. S. Guralnik, C. R. Hagen, and T. W. B. Kibble, Phys. Rev. Lett. **13**, 585 (1964).

[12] G. t'Hooft, Nucl. Phys. **B33**, 173 (1971); G. t'Hooft, Nucl. Phys. **B35**, 167 (1971).

[13] F. J. Hasert *et. al.* (GARGAMELLE Collaboration), Phys. Lett. **B46**, 121 (1973); J. Blietschan *et. al.* (GARGAMELLE Collaboration), Nucl. Phys. **B114**, 189 (1976); J. Blietschan *et. al.* (GARGAMELLE Collaboration), Phys. Lett. **B73**, 232 (1978).

[14] For a review of accelerator-based neutrino scattering experiments, see D. H. Perkins, Proceedings of the SLAC Summer Institute, SLAC-REPORT 215, p. 1 (1978)

[15] S. L. Glashow, J. Iliopoulos, and L. Maiani, Phys. Rev. **D2**, 1285 (1970).

[16] M. Perl *et. al.*, Phys. Rev. Lett **35**, 1489 (1975).

[17] W. R. Innes *et. al.*, Phys. Rev. Lett **39** 1240 (1977). Erratum: Phys. Rev. Lett **39**, 1640 (1977).

[18] F. Abe *et. al.* (CDF Collaboration), FERMILAB-PUB-95-022-E (1995). Submitted to Phys. Rev. Lett.

[19] S. Abachi *et. al.* (D0 Collaboration), FERMILAB-PUB-95-028-E (1995). Submitted to Phys. Rev. Lett.

[20] G. Arnison *et. al.* (UA1 Collaboration), Phys. Lett. **B134**, 469 (1984).

[21] G. Arnison *et. al.* (UA1 Collaboration), Phys. Lett. **B126**, 398 (1983).

[22] F. Halzen and A. Martin, *Quarks and Leptons: an Introductory Course in Modern Particle Physics*, John Wiley and Sons, New York (1984).

[23] D. H. Perkins, *Introduction to High Energy Physics*, Third Edition, Addison-Wesley, Menlo Park, California (1987).

[24] M. E. Peskin and D. V. Schroeder, *An Introduction to Quantum Field Theory*, Addison-Wesley, Menlo Park, California, (1995).

[25] This limit is the one cited in the *Review of Particle Properties, Full Listings*. Phys. Rev. **D50**, p. 1351 (1994). This limit was obtained using the galactic magnetic field. The original reference is Chibisov *et. al.*, Soviet Physics — Uspekhi **19** 624 (1976).

E. Fischbach, H. Kloor, R. A. Langel, A. T. Y. Liu, and M. Peredo, Phys. Rev. Lett. **73**, 514 (1994).

[26] Y. Nambu, Phys. Rev. Lett **4**, 380 (1960); J. Goldstone, A. Salam, and S. Weinberg, Phys. Rev **127**, 965 (1962).

[27] T.-P. Cheng and L.-F. Li, *Guage Theory of Elementary Particle Physics*, Clarendon Press, Oxford (1984).

[28] D. J. Gross and F. Wilczek, Phys. Rev. Lett. **30**, 1343 (1973); D. J. Gross and F. Wilczek, Phys. Rev. **D8**, 3633 (1973).

[29] R. D. Field and R. P. Feynman, Nucl. Phys. **B136**, 1 (1978).

[30] T. Sjöstrand, Computer Phys. Commun. **39** 347 (1986); T. Sjöstrand and M. Bengtsson, Comput. Phys. Commun. **43** 367 (1987).

[31] T. Sjöstrand, CERN-TH.6488 (1992) (Version 7.3); T. Sjöstrand, CERN-TH-7112-93, Feb, 1994 (Version 7.4).

[32] A. Kronfeld, FERMILAB-CONF-95/067-T (1995).

[33] J. Ellis, M. K. Gaillard, and G. G. Ross, Nucl. Phys. **B111**, 253 (1976).

[34] K. Abe *et. al.* (SLD Collaboration), Phys. Rev. Lett **71**, 2528 (1993); K. Abe *et. al.* (SLD Collaboration), Phys. Rev. **D50**, 5580 (1994);

[35] S. J. Brodsky and G. P. Lepage, Phys. Rev. **D28**, 228 (1983) is a reference which proposes a procedure to elmiminate scale ambiguities in QCD. Also see H. J. Lu, Stanford Ph. D. Thesis, SLAC-REPORT-406 (1992).

[36] P. N. Burrows and H. Masuda, SLD Physics Note # 36 (1995).

[37] J. D. Bjorken, Phys. Rev. **D17**, 171, (1978).

[38] P. Clarke, RAL-90-055 (1990).

[39] A. Blondel, B. W. Lynn, F. M. Renard, and C. Verzegnassi, Nucl. Phys. **B304**, 438 (1988).

[40] F. M. Renard, A. Blondel, and C. Verzegnassi, CERN-88-06, Vol. 1, *Polarization at LEP*, 197 (1988).

[41] K. Abe *et. al.*, Phys. Rev. Lett. **73**, 25 (1994)

[42] E. Torrence, SLAC Experimental Seminar, June 8, 1995.

[43] P. Gambino and A. Sirlin, NYU-TH-93/09/07, (1993).

[44] D. Buskulic *et. al.* (ALEPH Collaboration), CERN-PPE-95-023 (1995), submitted to Z. Phys; M. Acciarrie *et. al.* (L3 Collaboration), Phys. Lett. **B341**, 245 (1994); R. Akers *et. al.* (OPAL Collaboration), Z. Phys. **C65**, 1 (1995).

[45] D. Williams, Ph. D. Thesis, MIT (1994). Published as SLAC-REPORT-445.

[46] K. Abe *et. al.* (SLD Collaboration) Phys. Rev. Lett. **74**, 2895 (1995).

[47] J. Huber, talk given at the Int'l Europhysics Conference on High Energy Physics, Brussels, Jul. 27-Aug. 2, 1995. The SLD proceedings contribution is in preparation.

[48] K. Abe *et. al.* (SLD Collaboration) Phys. Rev. Lett. **74**, 2890 (1995).

[49] K. Abe *et. al.* (SLD Collaboration) SLAC-PUB-6979, submitted to the Int'l Europhysics Conference on High Energy Physics, Brussels, Jul. 27-Aug. 2, 1995.

[50] D. Su, *Production of Charm and Beauty in e^+e^- with Polarized Electron Beam*, Invited talk at the 6th Int'l Symposium on Heavy Flavor Physics, Pisa, June 6, 1995.

[51] D. Bardin *et. al.*, CERN-TH-6443 (1992).

[52] M. Peskin, Proceedings of the 17th SLAC Summer Institute on Particle Physics, SLAC-REPORT-361, p. 71 (1989).

[53] D. C. Kennedy, J. M. Im, B. W. Lynn, and R. G. Stuart, SLAC-PUB-4128 (1988).

[54] G. Altarelli and B. Lampe, Nucl. Phys. **B391**, 3 (1993).

[55] A. Djouadi, J. H. Kühn, and P. M. Zerwas, Z. Phys. **C46**, 411 (1990)

[56] B. A. Schumm, SLD Physics Note # 23 (1993).

[57] A. Djouadi, B. Lampe, and P. M. Zerwas, MPI-PH-94-81 (1994).

[58] J. B. Stav and H. A. Olsen, Trondheim U. Preprint 1994-17, (1994). This work has been summarized by P. N. Burrows in SLD Physics Note # 29 (1994).

[59] M. L. Swartz, SLAC-PUB-6710 (1994). Submitted to Phys. Rev. D.

[60] M. Peskin and T. Takeuchi, Phys. Rev. Lett **65**, 964 (1990).

[61] M. Peskin and T. Takeuchi, Phys. Rev. **D46**, 381 (1992).

[62] M. Boulware and D. Finnell, Phys. Rev. **D44**, 2054 (1991).

[63] T. G. Rizzo, SLAC-PUB-6672 (1994). Submitted to Phys. Rev. D.

[64] A. Olchevski, *Precision Tests of the Standard Model* , presented at the Int'l Europhysics Conference on High Energy Physics, Brussels, Jul. 27-Aug. 2. 1995.

[65] A. Passeri, *Forward-Backward Asymmetris for Heavy Flavours using Lifetime Tags*, presented at the Int'l Europhysics Conference on High Energy Physics, Brussels, Jul. 27-Aug. 2, 1995.

[66] R. Akers *et. al.* (OPAL Collaboration), CERN-PPE/95/50 (1995).

[67] D. Buskulic *et. al.* (ALEPH Collaboration), Phys. Lett. **B335** 99 (1994).

[68] P. Abreu *et. al.* (DELPHI Collaboration), Z. Phys. **C65**, 569 (1995).

[69] F. Liu *et. al.* (AMY Collaboration), Phys. Rev. **D49**, 4339-4347 (1994).

[70] M. Shirakata *et. al.* (VENUS Collaboration), Phys. Lett. **B278**, 499-505 (1992).

[71] K. Nagai *et. al.* (TOPAZ Collaboration), Phys. Lett. **B278**, 506-510 (1992).

[72] SLAC Linear Collider Conceptual Design Report, SLAC-REPORT-229 (1980). This report contains much that is out-dated, but provides an overview of the design considerations of the major SLC components.

[73] R. Prepost, Proceedings of the 21st SLAC Summer Institute on Particle Physics, SLAC-REPORT-444, p. 57 (1994).

[74] Neal, Richard B., *The Stanford Two Mile Accelerator*, Benjamin, N.Y. (1968).

[75] Z. D. Farkas, SLAC SLED Program, SLAC-TN-77-001, April, 1977; Z. D. Farkas, H. A. Hogg, G. A. Loew and A. R. Wilmunder, IEEE Trans. Nucl. Sci. NS-24, No. 3, 1827; G. A. Loew, Proc X^th Int. conf. on High Energy Accel., Serpukhov, USSR (1977), Vol 1, p. 58. See also Reference [72], p. 13-16.

[76] H. Wiedemann, SLAC-CN-58 (1981).

[77] C. Simopoulos and R. L. Holtzapple, SLAC-PUB-6813 (1995).

[78] C. Adolphsen /eal/ Proceedings of the IEEE Particle Accelerator Conference. p. 2019 (1993).

[79] K. Bane *et. al.*, SLAC-PUB-6894 (1995). Presented at the IEEE Particle Accelerator Conference (PAC 95).

[80] F. J. Decker, R. Holtzapple, T. Raubenheimer, SLAC-PUB-6604 (1994). Presented at the 17th International Linear Accelerator Conference (LINAC 94). Tsukuba, Japan, 1994.

[81] L. Hendrickson *et. al.*, SLAC-PUB-6621 (1994). Presented at the 17th International Linear Accelerator Conference (LINAC 94), Tsukuba, Japan, 1994.

[82] R. Erickson, T. H. Feiguth, J. J. Murray, SLAC-PUB-4199 (1987). Published in Washington PAC, p. 142 (1987).

[83] F. Zimmermann *et. al.*, SLAC-PUB-6790 (1995). Presented at the IEEE Particle Accelerator Conference (PAC 95).

[84] G. Bonvicini, R. Frey, E. Gero, W. A. Koska, R. C. Field, and A. Minten, Nucl. Instr. Meth. **A277**, 297 (1989).

[85] Y.-C. Chao *et. al.*, SLAC-PUB-5868 (1992). Presented at the 15th Int'l conf. on High-Energy Accelerators, Hamburg, Germany, Jul 20-24, 1992.

[86] S. Wagner, Proceedings of the May 12-14, 1993 SLD Collaboration Meeting. Volume 2, Chateau La Cresta, Saratoga, CA (1993); S. Wagner, Proceedings of the February 7-9, 1994 SLD Collaboration Meeting, Volume 2, Chateau La Cresta, Saratoga, CA (1994); and S. Wagner, Proceedings of the February 15-17, 1995 SLD Collaboration Meeting, Volume 2, p. 705, Chateau La Cresta, Saratoga, CA (1993).

[87] A. A. Sokolov and I. M. Ternov, Sov. Phys. Doklady **8**, 1203 (1964).

[88] W. Heitler, *The Quantum Theory of Radiation, 3^d ed.*, p. 264–267. Clarendon Press, Oxford. Reprinted by Dover, New York.

[89] P. Horowitz and W. Hill, *The Art of Electronics*, p. 437-442, Cambridge University Press, Cambridge (1980).

[90] T. Junk, SLD Note # 227 (1992).

[91] T. Lindberg, P. Emma, and R. Rossmanith, Proceedings of the IEEE Particle Accelerator Conference, p. 429 (1993).

[92] J. Irwin, Proceedings of the 21st SLAC Summer Institute on Particle Physics. SLAC-REPORT-444, p. 209 (1994).

[93] D. Calloway *et. al.*, SLAC-PUB-6423 (1994).

[94] T. Junk, SLD Note # 245 (1995).

[95] A. Lath and M. Woods, SLD Note # 236 (1994).

[96] O. Klein and Y. Nishima, Z. Phys. **52**, 823 (1929); Y. Nishina, Z. Phys. **52**, 869 (1929).

[97] H. Veltman, Phys. Rev. **D40**, 2810 (1989).

[98] W. Nelson, H. Hirayama, D. W. O. Rogers, SLAC-REPORT-265 (1985).

[99] B. A. Schumm (private communication).

[100] A. Lath, D. Freytag, *Compton Analysis: LeCroy Model 2249W ADC Linearity Study*, SLD Note 237, April, 1994.

[101] M. Swartz *et. al.*, SLAC-PUB-6467 (1994), submitted to Nucl. Instrum. Meth.

[102] L. G. Levchuk, Kharkov Preprint KFTI 92-32 (1992); L. G. Levchuk, Nucl. Instr. Meth. **A345**, 496 (1994).

[103] M. S. Lubell, Proceedings of the High Energy Physics with Polarized Beams and Targets, Argonne, IL, 1976 p. 418-423.

[104] G. Blaylock, SLD Physics Note # 22 (1993). Also, G. Blaylock, D. Briggs, B. Collins, and M. Petree, SLAC-PUB-5649 (1992). Presented at the Technical Conf. and Expo, San Francisco, CA, Jan 15-17, 1992.

[105] SLD Design Report, SLAC-REPORT-273 (1984).

[106] S. C. Berridge *et. al.*, IEEE Trans. Nucl. Sci. **37**, p. 1191 (1990).

[107] K. T. Pitts, SLAC-REPORT-446, *Electroweak Coupling Measurements from Polarized Bhabha Scattering at the Z^0 Resonance*, Ph. D. Thesis, University of Oregon (1994).

[108] M. Hildreth *et. al.*, SLAC-PUB–6656, Sept, 1994 (submitted to IEEE Trans. Nucl. Sci.).

[109] T. Usher, Proceedings of the SLD Collaboration Meeting, April 9-11, 1992, Vol. 2 (1992).

[110] D. Williams, Ph. D. Thesis, MIT (1994), Appendix B. Published as SLAC-REPORT-445.

[111] G. Agnew *et. al.*, SLAC-PUB-5906 (1992).

[112] M. Strauss *et. al.*, Proceedings of the 7th Meeting of the APS Division of Particles and Fields, World Scientific, Singapore, p. 1758 (1992). Also printed as SLAC-PUB-5970.

[113] P. Billoir, Nucl. Instr. Meth. **225** 352 (1984).

[114] M. Cavalli-Sforza *et. al.*, IEEE Trans. Nucl. Sci. **37**, 1132 (1990).

[115] D. Axen *et. al.*, Nucl. Inst. and Meth. *A238*, 472 (1993).

[116] A. C. Benvenuti *et. al.*, Nucl. Instrum. Meth. **A290**, 353 (1990).

[117] E. Iarocci, Nucl. Instrum. Meth. **217**, 30 (1983). G. Battistoni *et. al.*, Nucl. Instrum. Meth. **217**, 429 (1983).

[118] C. Peterson, D. Schlatter, I. Schmitt, and P. M. Zerwas, Phys. Rev. **D27**, 105 (1983).

[119] B. A. Schumm, Proceedings of the May 12-14, 1993 SLD Collaboration Meeting. Chateau La Cresta (1993).

[120] R. Wang, Ph. D. Thesis, University of Minnesota (1994).

[121] N. Isgur, D. Scora, B. Grinstein, and M. B. Wise, Phys. Rev. **D39**, 799 (1989).

[122] H. Albrecht *et. al.* (ARGUS Collaboration), Phys. Lett. **B221**, 422 (1989); H. Albrecht *et. al.* (ARGUS Collaboration), Phys. Lett. **B232**, 398 (1989).

[123] P. Kim (private communication, 1994).

[124] H. Albrecht *et. al.* (ARGUS Collaboration), Z. Phys. **C58**, 191 (1993).

[125] H. Albrecht *et. al.* (ARGUS Collaboration), Z. Phys. **C54**, 13 (1992).

[126] D. Coffman *et. al.* (MARK III Collaboration), Phys. Lett. **B263**, 135.

[127] F. Muheim, Presented at the 1994 APS DPF Meeting, Santa Fe, NM (1994).

[128] M. Thulasidas, Ph. D. Thesis, Syracuse University (1993).

[129] D. Su (private communication).

[130] GEANT program, version 3.21, CERN Application Software Group, CERN Program Library (1993). See R. Brun *et. al.*, GEANT3 User's Guide, CERN-DD//EE/84-1, CERN (1989).

[131] H. Fesefeldt, *GHEISHA*, PITHA 85/02 (1985).

[132] G. Grindhammer *et. al.*, Nucl. Instr. Meth. **A290**, 469 (1990).

[133] See, for example, the PDG's mini-review of electromagnetic shower parameterization in Physical Review **D50**, 1255-1256, and references therein.

[134] K. Abe *et. al.*, SLAC-PUB-6569, July, 1994 (submitted to Phys. Rev. D).

[135] R. G. Jacobsen, Ph.D. Thesis, Stanford University, 1991. Published as SLAC-REPORT-381.

[136] E. Farhi, Phys. Rev. Lett **39**, 1587 (1977).

[137] R. Brandelik *et. al.* (TASSO Collaboration), Phys. Lett. **B100** 357 (1981); C. Berger *et. al.* (PLUTO Collaboration), Nucl. Phys. **B214** 189 (1983); W. W. Ash *et. al.* (MAC Collaboration), Phys. Rev. Lett. **58** 1080 (1987); T. Greenshaw *et. al.* (JADE Collaboration), Z. Phys. **C42** 1 (1989).

[138] D. Stuart *et. al.* (AMY Collaboration), Phys. Rev. Lett. **64** 983 (1990); D. Stuart *et. al.* (AMY Collaboration); M. Shirakata *et. al.* (VENUS Collaboration). Phys. Lett. **B278**, 499, (1992).

[139] D. Buskulic *et. al.* (ALEPH Collaboration), Phys. Lett. **B284**, 177 (1992); P. D. Acton *et. al.* (OPAL Collaboration) Phys. Lett. **B294**, 436 (1992).

[140] M. Fendt *et. al.* (DELPHI Collaboration), CERN-PPE-95-076 (1995). Contributed to the 1995 Rencontres de Moriond Electroweak Session.

[141] P. D. Acton *et. al.* (OPAL Collaboration) Phys. Lett. **B302**, 523 (1993)

[142] M. V. Purohit *et. al.* (E791 Collaboration), FERMILAB-CONF-94-186-E (1994). Contributed to 27th International Conference on High Energy Physics (ICHEP), Glasgow, Scotland, 20-27 Jul 1994.

[143] P. N. Burrows, H. Park, K. t. Pitts, and J. M. Yamartino, SLD Note 229 (1993).

[144] J. M. Yamartino, SLD Physics Note 14 (1992).

[145] A review of SLC backgrounds may be found in M. D. Hildreth, Ph. D. Thesis, SLAC-REPORT-95-458, Appendix D, p. 300-324 (1995).

[146] M. Aguilar-Benitez *et. al.*, Physical Review **D50**, 1173 (1994).

[147] H. Neal, Stanford University Ph. D. Thesis (1995). Published as SLAC-REPORT-473.

[148] Jets are defined with the JADE algorithm, W. Bartel *et. al.*, Z. Phys. **C33**, 23 (1986), using a value of $y_{min} = 0.02$.

[149] D. Su, Proceedings of the February 7-9, 1994 SLD Collaboration Meeting, Volume 2, Chateau La Cresta, Saratoga, CA (1994).

[150] D. Decamp *et. al.* (ALEPH Collaboration), Phys. Lett. **B273**, 181 (1991).

[151] M. Hildreth, Stanford Ph.D. Thesis, p. 123 (1995). Published as SLAC-REPORT-458.

[152] B. Lampe, MPI-PH-93-74 (1993).

[153] M. Fero, SLAC-PUB-6678 (1994), presented at the XIV International Conference on Physics in Collision, Tallahassee, Florida, June 15-17, 1994.

[154] M. G. Bowler, Z. Phys. **C11** 161 (1981).

[155] D. Abbaneo, presented at the 1994 Rencontres de Moriond, Electroweak Session, March 12-19, 1994.

[156] D. Decamp, *et. al.* (ALEPH Collaboration), Phys. Lett. **B278**, 209 (1992).

[157] P. D. Acton, *et. al.* (OPAL Collaboration), Phys. Lett. **B281** 394 (1992).

[158] K. Abe *et. al.* (SLD Collaboration), Phys. Rev. Lett. **72**, 3145 (1994).

[159] S. Komahiya, *b and c Physics*, presented at the Int'l Europhysics Conference on High Energy Physics, Brussels, Jul. 27-Aug. 2, 1995.

[160] A. F. Falk and M. E. Peskin, Phys. Rev. **D49** 3320 (1994).

[161] T. Mannel and G. A. Schuler, Phys. Lett. **B279**, 194 (1992).

[162] F. E. Close, J. Körner, R. J. N. Phillips, and D. J. Summers, J. Phys. **G18**, 1716 (1992).

[163] J. G. Körner and M. Krämer, Phys. Lett. **B275**, 495 (1992).

[164] ALEPH Collaboration, EPS-0400, internal note contributed to the Int'l Europhysics Conference on High Energy Physics, Brussels, Jul. 27-Aug. 2, 1995.

[165] W. T. Eadie, D. Drijard, F. E. James, M. Roos, and B. Sadoulet, *Statistical Methods in Experimental Physics*, American Elsevier, 1971.

[166] See, for example, the PDG's mini-review of maximum-likelihood techniques in Physical Review **D50**, 1275-1282, and references therein.

[167] P. Billingsley, *Probability and Measure,* 2nd *ed.*, John Wiley & Sons, New York (1986), or any advanced text on statistics.

[168] H. Quinn, SLAC-PUB-6438 (1994); Decays into non-CP eigenmodes may have some asymmetry by projection onto CP eigenmodes with a helicity analysis — see I. Dunietz, H. Quinn, A. Snyder, and W. Toki

[169] G. Marchenisi, B. R. Webber, G. Abbiendi, I. G. Knowles, M. H. Seymour, and L. Stanco, Comput. Phys. Commun. **67**, 465-508 (1992).

[170] T. Takeuchi, A. K. Grant, J. L. Rosner, FERMILAB-CONF-94/279-T, presented at the DPF'94 Meeting, Albuquerque, NM. Aug 2-6, 1994.

[171] M. Swartz, SLAC-PUB-7001, Sep, 1995 (Submitted to Phys. Rev. D).

[172] B. Schumm, talk presented at the SLD Collaboration Meeting, August, 1995, Kirkwood, CA.

[173] D. Comelli, C. Verzegnassi, and F. M. Renard, UTS-DFT-94-02 (1994).

[174] D. Strom, *Precision Electroweak Experiments at LEP*, Invited talk at the SLAC Summer Institute, July 10-21, 1995. (get a better ref from EPS).

[175] M. Hildreth, Stanford Ph.D. Thesis (1995). Published as SLAC-REPORT-458.

[176] K. Abe *et. al.* (SLD Collaboration), SLAC-PUB-6681 (1995).

[177] D. Buskulic *et. al.* (ALEPH Collaboration), CERN-PPE-95-44 (1995); P. Abreu *et. al.* (DELPHI Collaboration), Z. Phys. **C66**, 341 (1994); R. Akers *et. al.* (OPAL Collaboration), CERN-PPE-94-217 (1994).

[178] P. Baringer *et. al.* (HRS Collaboration), Phys. Lett. **B206**, 551 (1988).

[179] A. Okamoto *et. al.* (VENUS Collaboration), Phys. Lett. **B278** 393 (1992).

[180] D. Jackson, SLD Physics Note # 27 (1995).

[181] SLD Collaboration, VXD3 Note # 1 (1994).